



Universitat Autònoma de Barcelona

**ADVERTIMENT.** L'accés als continguts d'aquesta tesi queda condicionat a l'acceptació de les condicions d'ús establertes per la següent llicència Creative Commons:  [http://cat.creativecommons.org/?page\\_id=184](http://cat.creativecommons.org/?page_id=184)

**ADVERTENCIA.** El acceso a los contenidos de esta tesis queda condicionado a la aceptación de las condiciones de uso establecidas por la siguiente licencia Creative Commons:  <http://es.creativecommons.org/blog/licencias/>

**WARNING.** The access to the contents of this doctoral thesis it is limited to the acceptance of the use conditions set by the following Creative Commons license:  <https://creativecommons.org/licenses/?lang=en>



# FUNCTIONAL SURFACES BY MEANS OF NANOIMPRINT LITHOGRAPHY TECHNIQUES

*Ariadna Fernández Estévez*

M. Sc. Physics

Tesi Doctoral

Programa de Doctorat en Física

Thesis Director: *Prof. Dr. Clivia M. Sotomayor Torres*

Tutor: *Prof. Dr. Jordi Mompert*

Supervisor: *Dr. Nikolaos Kehagias*

Departament de Física

Facultat de Ciències

2016



*A mamá, a papá*

# Abstract

Different surface functionalities can be achieved by means of topography instead of chemistry, based on inspirations from nature. The main objective of this thesis is the investigation of Nanoimprint Lithography (NIL) as a feasible fabrication technique to modify both organic and inorganic surfaces to alter their physical properties and utilize them for superhydrophobic and oleophobic applications.

During this thesis a modified nanoimprint technique, capable of imprinting with zero residual layer was developed. This novel imprint based technique is adaptable to pattern over free form surfaces, allowing us to realize tailored three dimensional (3D) hierarchical micro and nanostructured surfaces.

We demonstrate that the fabrication techniques developed in this thesis, are adaptable to industrial manufacturing process, allowing their application on the development of functional surfaces. The produced 3D hierarchical surfaces were realized using fully industrial replication methods such as electroplating and injection molding techniques. Moreover, various materials have been tested into which the 3D hierarchical structured were replicated. Our manufacturing approach allowed us to reproduce our superhydrophobic surfaces in a controlled manner opening the path to high volume manufacturing of functional plastic components and surfaces.

Within our experimental findings we achieved a static contact angle value of  $170^{\circ}$  with a hysteresis of  $4^{\circ}$  without the need of any additional chemical treatment. Dynamic effects were measured on the produced surfaces, obtaining remarkable self-cleaning properties, as well as excellent robustness over impacting droplets.

The precise control of the developed fabrication technique allowed us to realize hybrid hierarchical patterned surfaces with tunable wetting properties. Hierarchical surfaces were realized resulting in a dual state functionality. In particular, our

structured surfaces exhibit both ‘lotus’ and ‘petal’ effect when varying the deposition conditions of the water droplets, without the need of any modification of the surface. The great difference between the capillary pressures exerted by the micro and nanostructures resulted in a tailored adhesion of the water droplets. The low capillary pressure induced by the microstructures and the high capillary pressure observed by the nanostructures, allowed to achieve a controlled dynamic effect, enabling different wetting states on the same hybrid surface.

Despite the perception that NIL is not suitable for direct imprinting surfaces which contain overhanging structures, within this thesis we prove that ultraviolet light assisted nanoimprint lithography (UV-NIL) is a suitable technique to realize mushroom-like structures. These 3D structures, which contained overhanging features, were fabricated by a novel one-step up-plating process. The structures were successfully replicated in a commercial UV curable resist material, that, in combination with a chemical post treatment, exhibited amphiphobic (both hydrophobicity and oleophobicity) properties. Wetting analysis of the produced 3D surface was performed using a variety of liquids possessing different surface tensions. The critical surface tension for achieving oleophobicity was established experimentally.

# Acknowledgements

First of all I would like to thank Prof. Clivia M. Sotomayor Torres, my supervisor, for giving me the opportunity to carry out my research in her group.

I would also like to sincerely thank my daily supervisors Dr. Nikolaos Kehagias and Dr. Achille Francone for all their help and fruitful conversations.

I would like to thank also to all the people from the P2N group, the people who still there and the people who have left.

I am grateful to all our collaborators, specially to Markus Guttman from KIT, and all the NILT people.

My sincere thanks to my family and friends who helped me in all the difficult moments.

To finish, I am absolutely grateful to my mom, without you, I would not be here.





# Nomenclature

## Abbreviations

**AAO** Anodic aluminum oxide

**CA** Contact angle

**CAH** Contact Angle Hysteresis

**CVD** Chemical vapor deposition

**DRIE** Deep-reactive ion etching

**EBL** Electron beam lithography

**F-ASLs** Fluorinated antiadhesive layers

**NIL** Nanoimprint Lithography

**PDMS** Polydimethylsiloxane

**PEG** Polyethylene glycol

**PMMA** Poly(methyl methacrylate)

**PP** Polypropylene

**PS** Polystyrene

**PTFE** Polytetrafluoroethylene

**PVA** Poly(vinyl alcohol)

**PVDF** Poly(vinylidene fluoride)

**RF** Radio frequency

**RIE** Reactive ion etching

**RNIL** Reverse nanoimprint lithography

**SAM** Self-assembled monolayer

**SEM** Scanning Electron Microscope

**UV-NIL** Ultraviolet-assisted nanoimprint lithography

**WCA** Water contact angle

**WSA** Water sliding angle

## **Symbols**

$A_C$  Capillary area

$A_{LA}$  Liquid-air interface area

$A_{SL}$  Solid-liquid interface area

$\alpha$  Sliding angle

$Bo$  Bond number

$C$  Speed of the sound in water (1495 m/s)

$\Delta\theta$  Contact angle hysteresis

$F$  Faraday number (96485C/mol)

$f_{SL}$  Solid-liquid contact fraction

$g$  Acceleration of the gravity

$\gamma_{LA}$  Interfacial energy liquid-air

$\gamma_{SA}$  Interfacial energy solid-air

$\gamma_{SL}$  Interfacial energy solid-liquid

$I$  Current

$I/A$  Current density

$\kappa_C$  Capillary length

$L_C$  Capillary length

$m$  Mass

$P_{antiwetting}$  Antiwetting pressure

$P_C$  Capillary pressure

$P_D$  Dynamic pressure

$P_{wetting}$  Wetting pressure

$P_{WH}$  Water hammer pressure

$\psi$  Texture angle

$r$  Surface roughness

$Re$  Reynolds number

$\rho$  Density

$t$  Time

$T_g$  Glass transition temperature

$\theta_C$  Critical intrinsic contact angle

$\theta_A$  Advancing contact angle

$\theta_{CB}$  Cassie-Baxter contact angle

$\theta_R$  Receding contact angle

$\theta_W$  Wenzel contact angle

$\theta_Y$  Young contact angle

$V$  Impact velocity

$We$  Weber number

$W_{SL}$  Work of adhesion

$z$  Valency number



# Contents

<b>Abstract</b>	<b>iii</b>
<b>Acknowledgements</b>	<b>v</b>
<b>Nomenclature</b>	<b>vii</b>
<b>Contents</b>	<b>xii</b>
<b>List of Figures</b>	<b>xvi</b>
<b>List of Tables</b>	<b>xxvii</b>
<b>1 Introduction and Objectives</b>	<b>1</b>
<b>2 Fundamental Wetting Concepts</b>	<b>8</b>
2.1 Surface Tension and Contact Angle . . . . .	9
2.2 Contact Angle Hysteresis . . . . .	11
2.3 Classic Models of Wetting . . . . .	13
2.3.1 The Wenzel model . . . . .	13
2.3.2 The Cassie-Baxter model . . . . .	16
2.4 Stability of the Superhydrophobicity . . . . .	18
2.4.1 Thermodynamic Analysis . . . . .	20
2.4.2 Dynamic Analysis . . . . .	22
2.5 Superhydrophobic States . . . . .	24
2.6 Effect of Hierarchical Roughness . . . . .	27
2.7 Special wetting: Oleophobicity . . . . .	29
<b>3 Realization of Surfaces with Special Wetting</b>	<b>32</b>

3.1	Superhydrophobic Surfaces . . . . .	32
3.1.1	Top-down Techniques . . . . .	33
3.1.2	Bottom-up Techniques . . . . .	37
3.1.3	Nanoimprint-based methods . . . . .	39
3.1.4	Summary . . . . .	41
3.2	Oleophobic Surfaces . . . . .	43
3.2.1	Origin of Oleophobicity . . . . .	43
3.2.2	Top-down Techniques . . . . .	44
3.2.3	Bottom-up Techniques . . . . .	45
<b>4</b>	<b>Nanopatterning Techniques</b>	<b>47</b>
4.1	Nanoimprint Lithography . . . . .	48
4.1.1	Thermal and UV-assisted NIL . . . . .	48
4.1.2	Reverse NIL . . . . .	49
4.1.3	3D NIL . . . . .	51
4.2	Electroplating . . . . .	56
4.2.1	Template-assisted electroplating . . . . .	59
4.3	Injection Molding . . . . .	61
4.3.1	Injection molding for functional plastic surfaces . . . . .	64
4.4	Process flow . . . . .	65
<b>5</b>	<b>Materials and Processes</b>	<b>67</b>
5.1	Materials . . . . .	68
5.1.1	Stamps & Molding materials . . . . .	68
5.1.2	Patterning materials . . . . .	70
5.2	Processes . . . . .	72
5.2.1	Pattern definition by conventional lithographic techniques	72
5.2.2	Nanoimprint Tools . . . . .	77
5.2.3	Electroplating . . . . .	78
5.2.4	Injection Molding . . . . .	81
5.3	Characterization techniques . . . . .	82
5.3.1	Scanning Electron Microscope . . . . .	82

5.3.2	Surface wetting . . . . .	84
<b>6</b>	<b>Development of Nanopatterning Techniques</b>	<b>87</b>
6.1	UV-NIL . . . . .	87
6.2	Reverse NIL . . . . .	89
6.2.1	Free-Residual layer NIL . . . . .	90
6.2.2	RNIL for 3D hierarchical structures . . . . .	100
6.3	Electroplating and Up plating . . . . .	105
6.3.1	Electroplating . . . . .	106
6.3.2	Up-plating . . . . .	107
6.4	Injection Molding . . . . .	108
<b>7</b>	<b>Results and Discussion</b>	<b>111</b>
7.1	Design of Structures for Superhydrophobicity . . . . .	111
7.1.1	Microstructures . . . . .	111
7.1.2	Nanostructures . . . . .	114
7.1.3	Structures Fabrication . . . . .	117
7.2	Self-cleaning Surfaces . . . . .	118
7.2.1	Wetting of 2D Surfaces . . . . .	119
7.2.2	Wetting of 3D Hierarchical Surfaces . . . . .	123
7.2.3	Dynamic effects . . . . .	126
7.2.4	Summary . . . . .	130
7.3	Design of hierarchical surfaces for tuning wetting characteristics .	131
7.3.1	Morphology control and Wettability . . . . .	133
7.3.2	Dynamic behavior . . . . .	135
7.3.3	Effect of the inclination . . . . .	144
7.3.4	Summary . . . . .	148
7.4	Oleophobic surfaces . . . . .	150
7.4.1	Morphology control . . . . .	153
7.4.2	Wetting analysis . . . . .	155
7.4.3	Robustness of the oleophobicity . . . . .	160
7.4.4	Summary . . . . .	162



<b>8 Conclusions and Prospects</b>	<b>163</b>
<b>Bibliography</b>	<b>166</b>

# List of Figures

Figure 1.1	a) Water resting on the lotus leaf and b) typical SEM image of the surface structures on the lotus leaf [7]. . . . .	2
Figure 1.2	(Left) Water droplet sliding along a dirty hydrophilic surface. (Right) Water droplet sliding along a dirty superhydrophobic surface. . . . .	3
Figure 1.3	Examples of hierarchical structures present in the nature. The images correspond to SEM photographs of a) rose petal [8], b) gecko foot [9], c) shark skin [10] and d) butterfly wing [11]. . . . .	3
Figure 1.4	Schematics of wetting of the three different surfaces. The largest contact area between the droplet and the surface is given in microstructured surfaces, but is reduced in nanostructured surfaces and is minimized in hierarchical structured surfaces. . . . .	4
Figure 2.1	The contact angle $\theta_0$ and all the surface tensions in a system consisting of a water droplet resting on a flat surface. . . . .	8
Figure 2.2	Advancing ( $\theta_A$ ) and receding ( $\theta_R$ ) contact angles obtained by a) tilting the surface at the critical angle ( $\alpha$ ), b) increasing the size of the droplet and c) decreasing the size of the drop. . . . .	12
Figure 2.3	a) Schematic illustration of a droplet in the Wenzel state. b) Illustration of the Wenzel roughness ratio $r$ related to the Wenzel state. . . . .	14
Figure 2.4	Contact angle ( $\theta_W$ ) as a function of the roughness factor ( $r$ ) for various CAs for a smooth surface ( $\theta_0$ ). . . . .	15

Figure 2.5	a) Measured contact angles on hydrophilic and hydrophobic surfaces. b) SEM micrographs of the patterned polymer surface. Both low aspect ratio (LAR) and high aspect ratio (HAR) are shown, as well as the micropatterned lotus replica [30]. . . . .	16
Figure 2.6	a) Schematic illustration of a droplet in the Cassie-Baxter state. b) Illustration of the solid-liquid contact fraction $f_{SL}$ defined in the Cassie-Baxter equation. . . . .	18
Figure 2.7	Mechanisms showing transition from Cassie to Wenzel states: a) sag mechanism and b) depinning mechanism [34]. . . . .	19
Figure 2.8	Multiple minima of the Gibbs energy of a droplet deposited on a rough surface. . . . .	20
Figure 2.9	Apparent contact angle $\theta^*$ plotted in function of the Young CA, denoted by $\theta$ . Theoretically, the Wenzel state exists when $90^\circ < \theta < \theta_C$ , and the Cassie-Baxter state exists when $\theta_C < \theta < 180^\circ$ . However, the Cassie-Baxter state can also be observed for $\theta < \theta_C$ , shown by the dotted line after the critical point. . . . .	22
Figure 2.10	Cross-section of the meniscus on a pillar structure; $R$ is the radius of curvature of the meniscus, $h$ the penetration of the meniscus and $\theta$ is the contact angle. . . . .	24
Figure 2.11	Schematic illustration of a droplet in the mixed state. The droplet partially penetrates into the cavities. . . . .	25
Figure 2.12	Different states of superhydrophobic surfaces proposed by Wang and Jiang [57]: a) Wenzel state, b) Cassie superhydrophobic state, c) the ‘Lotus’ state (a special case of Cassie superhydrophobic state), d) the transitional superhydrophobic state between Wenzel and Cassie states, and e) the ‘Gecko’ state, characterized by a large adhesive force. . . . .	25

Figure 2.13 Schematics of nine wetting regimes for a rough surface characterized proposed by Bhushan and Nosonovsky [20], characterized by no penetration, partial penetration, and complete penetration of water into microroughness, nanoroughness and both micro and nanoroughness. . . . .	26
Figure 2.14 The solid-liquid fraction of a microstructure, a nanostructure, and a hierarchical micro nanostructure in contact with a drop. . . . .	29
Figure 2.15 a) A schematic of a concave texture ( $\psi > 90^0$ ) showing a liquid droplet with $\theta > 90^0$ in the Cassie–Baxter state. b) A schematic of a convex texture (re-entrant texture, $\psi < 90^0$ ) showing a lower surface tension liquid with $\theta < 90^0$ in the Cassie–Baxter state. . . . .	30
Figure 3.1 SEM image and WCA images of a) silica micropillars [77], b) silica micro nano rod hierarchical structure and [78] and c) vertically aligned hair arrays of PMMA [79]. . . . .	35
Figure 3.2 SEM image and WCA images of a) nanocone structure of fused silica surface [80] and b) nanocone array made by means of block-copolymer lithography [81]. . . . .	35
Figure 3.3 SEM image and WCA images of a) line-patterned PDMS surfaces [86] and b) laser textured brass surface [87]. . . . .	37
Figure 3.4 SEM images of a) hierarchical structure surfaces with ZnO seed layer on silicon pyramid surfaces [92] and b) nanoflake film grown on a glass substrate [93]. . . . .	38
Figure 3.5 SEM images of a) hierarchical micro structures on a PP surface [67], b) nanopattern over the overhanging structures [100] and c) UV imprinted PFPE surface [101]. . . . .	40
Figure 3.6 SEM images of a) hierarchical $TiO_2$ structures [102], b) nanopatterned and shrunken thermal shrinkage film (TSF) [103] and c) nanopillars treated with $C_4F_8$ plasma [104]. . . . .	41
Figure 3.7 SEM images of a) re-entrant structures fabricated by Tuteja et al. [71] and c) re-entrant structures fabricated by Zhao et al. [108]. . . . .	43

Figure 3.8	SEM images of a) nanoin-micro hierarchical structure, b) nanoscale re-entrant curvature and c) simple overhanging structure.	45
Figure 4.1	a) Schematic of thermal nanoimprint lithography. b) Schematic of UV nanoimprint lithography. . . . .	48
Figure 4.2	Schematic of the reverse nanoimprint lithography process at a temperature a) higher than $T_g$ and b) lower than $T_g$ . . . . .	51
Figure 4.3	SEM images of a 3D nickel mold fabricated by NIL and electroplating techniques. . . . .	52
Figure 4.4	Schematics of building 3D micro and nanostructures by transfer bonding and sequential layer stacking. . . . .	53
Figure 4.5	Schematics of nanoimprint over topography with two different results: a) whole layer transfer (700 nm period PMMA grating transferred onto substrate line patterns with spacing of less than 2 $\mu m$ ) and b) layer transfer only on protruded surfaces (700 nm period PMMA grating transferred onto substrate line patterns with spacing of 5 $\mu m$ ) [124]. . . . .	53
Figure 4.6	Schematic diagram for hierarchical surface by two consecutive nanoimprints. . . . .	54
Figure 4.7	Schematics of the electroplating process. . . . .	57
Figure 4.8	Schematics of the cathode arrangement for the production of micro and nanostructures by means of electroplating. . . . .	60
Figure 4.9	SEM images of different electroplated structures: a) zinc macroporous film, b) indium-antimony nanowire and c) gold nanopillars. . . . .	61
Figure 4.10	Schematic of the injection molding process [139]. . . . .	62
Figure 4.11	Schematic of the process chain followed in this thesis to produce functional plastic products. . . . .	65
Figure 5.1	Schematic of the followed method for the deposition of a fluorinated antiadhesive layer on the mold surface. . . . .	70

Figure 5.2	Schematic diagram showing the photolithography process using a negative and a positive resist. . . . .	73
Figure 5.3	Schematic diagram showing the electron beam process using a negative and a positive resist. . . . .	74
Figure 5.4	Different possible plasma etch processes as a function of the chamber pressure scale. . . . .	76
Figure 5.5	Schematic process of the plasma etching. . . . .	76
Figure 5.6	CNI Tool from NIL Technology <i>ApS</i> . . . . .	77
Figure 5.7	Schematics of thermal NIL process performed by the CNI Tool. . . . .	78
Figure 5.8	Photograph of the UV-assisted NIL setup . . . . .	78
Figure 5.9	Schematics of the a) up-plating and b) electroplating processes with two representative SEM images. . . . .	79
Figure 5.10	Photographs of the electroplating equipment used throughout this thesis. . . . .	80
Figure 5.11	Photographs of the injection molding equipment used throughout this thesis. . . . .	81
Figure 5.12	The schematic diagram of the scanning electron microscopy (SEM) system. . . . .	83
Figure 5.13	Photograph of the FEI Quanta 650 FEG SEM equipment used in this work. . . . .	84
Figure 5.14	Contact angle measurement performed by the software from the contact angle goniometer. . . . .	85
Figure 5.15	Photograph from EasyDroplet Standard droplet shape analysis system from Krüss. . . . .	86
Figure 6.1	SEM images of a) 2D micropillars pattern imprinted in Ormocomp by UV-NIL and b) 3D hierarchical pattern imprinted in mr-XNIL26 SF by UV-NIL. . . . .	88
Figure 6.2	Diagram showing the targeted applications obtained with the RNIL method developed in this thesis. . . . .	89

Figure 6.3	Schematic illustration of the residual-layer-free reversal NIL process. . . . .	91
Figure 6.4	Schematic of the honeycomb-like structure used in this work.	91
Figure 6.5	a) SEM image of the positive honeycomb pattern. b) SEM image of the negative honeycomb pattern. . . . .	92
Figure 6.6	SEM image PDMS stamps coater with mr-NIL 6000E at a) 1500 rpm, b) 3000 rpm and c) 4000 rpm for 1 minute. . . . .	93
Figure 6.7	SEM image of mr-NIL 6000E coated PDMS stamps after PEG functionalization. . . . .	94
Figure 6.8	SEM image of PMMA 75K coated PDMS stamp at 4000 rpm during 1 min. . . . .	94
Figure 6.9	SEM images of diluted PMMA spin coated on PDMS stamp, speed 4000 rpm for 1 minute (a) PMMA with a viscosity of $3.2\text{ mPa}\cdot\text{s}$ and (b) PMMA with a viscosity of $5.2\text{ mPa}\cdot\text{s}$ . . . . .	95
Figure 6.10	SEM images of RNIL with mr-NIL 6000E resist on silicon. The imprint parameters were $40^{\circ}\text{C}$ , 2 bar during 3 min. . . . .	95
Figure 6.11	SEM images of RNIL with PMMA 75K resist on silicon. The imprint parameters were $110^{\circ}\text{C}$ , 2 bar during 3 min. . . . .	96
Figure 6.12	SEM images of RNIL with diluted PMMA 75K resist on silicon with viscosities of a) $5.2\text{ MPa}\cdot\text{s}$ and b) $3.2\text{ MPa}\cdot\text{s}$ . . . . .	97
Figure 6.13	a) Photograph of a large area imprint on a nickel-coated steel wafer and b) SEM image of the honeycomb structure with no residual layer on a nickel-coated substrate. . . . .	97
Figure 6.14	Tilted SEM image of a honeycomb polymer structure, which is reverse imprinted on a nickel-coated silicon substrate with high roughness of the nickel surface. . . . .	98
Figure 6.15	Tilted SEM image of honeycomb polymer structures reverse imprinted on pre-patterned silicon surfaces on a) holes, b) lines with a size bigger than the honeycomb pattern and c) lines with a size smaller than the honeycomb pattern. . . . .	98

Figure 6.16 Schematic of the fabrication of the 3D hierarchical surfaces. The microstructures were fabricated by UV-NIL followed by a RNIL process to transfer the nanostructures from the mold to d.1) the top of the microstructures or d.2) the whole microstructure. . . . .	102
Figure 6.17 Tilted view SEM images of squared micropillars with several nanostructures on the top surface, a) the honeycomb pillar structure, b) honeycomb line structure, c) nanopillars and d) nanospikes on top. . . . .	104
Figure 6.18 Tilted view SEM images of cylindrical micropillars decorated with nanostructures with the intact mode. a) Nanospikes on micropillars and b) Nano pillars on micropillars. . . . .	105
Figure 6.19 Schematic diagram of the different electroplating-based approaches followed in this thesis and their corresponding purposes.	106
Figure 6.20 Tilted view SEM images of nickel shims fabricated by electroplating. a) Negative pattern of the honeycomb pillars on micro pillars, b) Negative pattern of nano pillars on micro pillars.	107
Figure 6.21 SEM images of nickel shims fabricated by up-plating. The honeycomb pattern was created with PMMA by means of the free-residual layer RNIL developed in Section 6.2.1. . . . .	108
Figure 6.22 SEM images of fully metallic nickel surfaces fabricated by the up-plating process. The original mask consisted in an array of cylindrical holes made by photolithography. . . . .	108
Figure 6.23 SEM images of the injection molded surface made of a) PP and b) TOPAS and their corresponding contact angle images. . .	109
Figure 7.1 Schematics of a) square array of cylindrical pillars and b) square array of square pillars. . . . .	112
Figure 7.2 Plot showing the possible combinations of diameter/width and period to get a solid-liquid contact fraction of 0.09 for cylindrical and squared pillars. . . . .	113
Figure 7.3 Tilted view SEM images of the microstructures selected in this work. a) Squared pillars, b) Cylindrical pillars. . . . .	114



Figure 7.4	Tilted view SEM images of squared micropillars with several nanostructures on the top surface, a) the honeycomb pillar structures, b) honeycomb line structures, c) nanopillars and d) nanospikes. . . . .	115
Figure 7.5	Schematic description of the fabrication of 3D hierarchical surfaces. a) The starting point are the inking mode fabricated samples, as described in Section 6.2.2, b) a PDMS stamp was fabricated to have a final mold with the 3D structures, c,d,e,) the PDMS was used to make the final imprints over different substrates. . . . .	119
Figure 7.6	Top view SEM images of the micropattern used to design the hierarchical structures and its corresponding water contact angle value. . . . .	120
Figure 7.7	Tilted view SEM images of the nanostructures selected for the fabrication of the hierarchical structures and their static water contact angles. a) Honeycomb pillars, b) honeycomb lines, c) nano pillars, d) nano spikes. . . . .	121
Figure 7.8	Tilted view SEM images of squared micropillars with several nanostructures on the top surface, a) the honeycomb pillar structure, b) honeycomb line structure, c) nanopillars and d) nanospikes. . . . .	123
Figure 7.9	Photograph of the micro/nano hierarchical structure fabricated on a PET substrate over an area of $5 \times 5 \text{ cm}^2$ with several water droplets resting on the patterned area. . . . .	124
Figure 7.10	Measured contact angles of the hierarchical surfaces compared to the theoretical Cassie-Baxter state curve. Snapshots of water droplets contacting the samples are shown as insets. . . . .	126
Figure 7.11	Self-cleaning of the superhydrophobic surface with hierarchical nanospikes-on-micropillars on PET: a) image of the superhydrophobic surface covered with pepper powder as contaminant, b-f) series of images showing a droplet rolling along the surface taking all the contaminants with it. (The scale bars correspond to 1 cm). . . . .	127

Figure 7.12 Sequence showing the low adhesion between a water droplet and the superhydrophobic surface, indicating a small contact angle hysteresis: a) The water droplet is suspended from a needle. b) Approaching of the substrate towards the droplet. c) The droplet undergoes a sliding movement due to the low adhesion between them. d, e) Retracting the substrate from the droplet. f) The droplet remains attached to the needle without wetting the surface. . . . .	128
Figure 7.13 Sequence of a 10 $\mu$ l droplet impacting on the squared micropillars array. The snapshots are obtained using a high-speed camera. The sequence shows a) approach of the droplet, b) hitting the surface, c,d) recoil and e,f)penetration into the cavities of the microstructures, ending in a Wenzel state. . . . .	129
Figure 7.14 Sequence of a 10 $\mu$ l droplet impacting on the nanospikes-on-micropillars array. The snapshots are obtained using a high-speed camera. The sequence shows a) approach of the droplet, b) hitting the surface, c,d) recoil of the droplet and e,f) roll-off of the droplet along the surface. . . . .	129
Figure 7.15 Tilted view SEM images of cylindrical micropillars decorated with nanostructures in two different modes: a) intact mode of the nanospikes on micropillars, b) intact mode of the nanopillars on micropillars, c) inking mode of the nanospikes on micropillars and d) inking mode of the nanopillars on micropillars. The insets correspond to their WCA images. . . . .	133
Figure 7.16 Graphs showing the dynamic behavior of droplet on the a) nanopillars-micropillars surface and b) nanospikes-micropillars surface. . . . .	137
Figure 7.17 Schematic of the different wetting states observed on the hierarchical surfaces made with the intact mode. a) Transitions for the nanospikes - micropillars configuration and b) transitions for the nanopillars - micropillars configuration. . . . .	137

Figure 7.18 Snapshots of a 10 $\mu\text{l}$ droplet hitting the surface at 0.6 m/s for the Case I, at 0.8 m/s for the Case II and at 1.8 m/s for the Case III. . . . .	139
Figure 7.19 Schematics of three different wetting states in function of the wetting and antiwetting pressures. . . . .	141
Figure 7.20 Snapshots showing a) droplet in contact with a hydrophobic surface and b) droplet in contact with a hydrophilic surface. . . . .	144
Figure 7.21 Snapshots of a 10 $\mu\text{l}$ droplet hitting the surface ( $20^\circ$ tilt) at normal velocities of 0.94 m/s, 1.65 m/s and at 2.01 m/s. Pinning of the droplet occurs at velocities higher than 2 m/s. . . . .	146
Figure 7.22 Snapshots of a 10 $\mu\text{l}$ droplet hitting the surface ( $30^\circ$ tilt) at normal velocities of 0.94 m/s, 1.65 m/s and at 2.01 m/s. Pinning of the droplet occurs at velocities higher than 2 m/s. . . . .	146
Figure 7.23 Snapshots of a 10 $\mu\text{l}$ droplet hitting the surface ( $45^\circ$ tilt) at normal velocities of 0.94 m/s, 1.65 m/s and at 2.01 m/s. Pinning of the droplet occurs at velocities higher than 2 m/s. . . . .	147
Figure 7.24 Schematic of the fabrication process followed to develop the polymeric mushroom-like structures. The template was fabricated in nickel by electroplating. A soft stamp was produced with the negative pattern. This soft stamp was used to produce mushroom-like structures by direct UV-NIL in Ormocomp. . . . .	152
Figure 7.25 SEM images showing Ormocomp mushroom-like structures with different overhanging degrees. Distance between caps of a) 3-3.5 $\mu\text{m}$ , b) 2-2.5 $\mu\text{m}$ and c) 0.8-1 $\mu\text{m}$ . . . . .	154
Figure 7.26 Photographs of 5 $\mu\text{l}$ droplets of different liquids obtained on the surface with medium overhanging degree. . . . .	158
Figure 7.27 Graph showing the obtained contact angle values for liquids with different surface tensions. . . . .	158

Figure 7.28 Profiles of liquid droplets of volume $v = 5 \mu\text{l}$ and capillary length $a = 1.25 \text{ mm}$ ( $Bo = 0.075$ , solid line). In comparison with a spherical profile ( $Bo$ , dashed line), it can be observed the effect of the gravity on the sagging effect [184]. . . . .	159
Figure 7.29 Surface tension obtained for different ethanol concentrations in water. . . . .	161
Figure 7.30 Measured contact angle of different water/ethanol solutions possessing different surface tensions. . . . .	161

# List of Tables

Table 2.1	Surface tension of common liquids used to assess repellency of a surface [68]. . . . .	29
Table 3.1	Typical techniques and corresponding materials to produce micro nanoroughness for superhydrophobic purposes. . . . .	42
Table 4.1	Nanoimprint-based techniques to produce 3D structures with their corresponding advantages and drawbacks. . . . .	56
Table 5.1	Advantages and problems of the followed electroplating-based approaches. . . . .	80
Table 6.1	Imprinting conditions used in soft UV-NIL for imprints with the two photocurable resists used in this thesis. . . . .	89
Table 6.2	Dimensions and SEM images of the different structures studied in this thesis. . . . .	101
Table 6.3	Imprint parameters to fabricate 3D structures with the inking mode. . . . .	103
Table 6.4	Imprint parameters to fabricate 3D structures with the intact mode. . . . .	103
Table 6.5	Static and dynamic measurements obtained from the wetting analysis of the injection molded polymers. . . . .	110
Table 7.1	Geometrical parameters for all the microstructures analyzed in this thesis . . . . .	113
Table 7.2	Dimensions, surface roughness ( $r$ ) and solid-liquid contact fraction ( $f$ ) of the different structures used in this work. . . . .	116

Table 7.3	Calculated and experimental contact angles measurements of the micropattern on XNIL26 surface. . . . .	120
Table 7.4	Calculated and experimental contact angles measurements of the nanostructures on XNIL26 printed surfaces. . . . .	122
Table 7.5	Calculated and experimental measured contact angles of the hierarchical structures fabricated on XNIL 26 printed surfaces. . . . .	124
Table 7.6	Experimental contact angles measurements for the hierarchical structures fabricated with PMMA/Ormocomp. . . . .	134
Table 7.7	Summary of results for each of the tilt angles tested in this study. The droplet diameters are 4 mm. . . . .	148
Table 7.8	Experimental water contact angles measurements for the Ormocomp mushroom-like structures with different overhanging degrees. . . . .	156
Table 7.9	Experimental contact angles measurements for the Ormocomp mushroom-like structures with different overhanging degrees measured with liquids with different surface tension. . . . .	157
Table 7.10	: Surface tension and density values for the liquids used in this study. . . . .	160

# Chapter 1

## Introduction and Objectives

The idea of observing, understanding and learning new concepts from the properties formed in nature is called ‘biomimetics’ and has recently gained a great deal of interest. These properties are created through designed surfaces or interfaces containing structural features on the micro and nanoscale. Taking a look at nature, different structures in the nano and micrometer range can be observed offering a wide range of functionalities, such as anti-reflective, self-cleaning, hydrophobic/hydrophilic or colour appearance. Biomimetics is a highly interdisciplinary field and crosses the boundaries between academic disciplines such as physics, chemistry, biology and material science. With advancements in characterization techniques, observation of these features is now possible allowing a better understanding of their mechanisms. The understanding of the functions provided by objects and processes found in nature can guide us to imitate and produce nanomaterials, nanodevices, and processes [1].

There are a large number of objects, including bacteria, animals and plants with properties of commercial interest. Many people have presented a number of results in the field of biomimetic surfaces including the lotus-leaf surface, which has self-cleaning property; the gecko foot, which has very high adhesion with the surface; the moth eye, which does not reflect light; the water strider leg, which stays dry on the top the water or the darkling beetle, which collects water using hydrophilic microposts [1–3]. Most of these objects have a feature in common, which is a hierarchical roughness ranging from nanometers to millimeters [4].

When a small liquid droplet is placed onto a solid surface, the drop can attain

various wetting states depending on the characteristic properties of the underlying solid substrate. For example, if the water droplet could retain a nearly spherical shape on the solid surface and roll off rapidly when the surface is tilted slightly, such surface is superhydrophobic and self-cleaning. A solid surface is considered superhydrophobic if the water contact angle is higher than  $150^\circ$ .

Nature provides several examples of superhydrophobic surfaces. The most famous example of natural superhydrophobic surface is the *Nelumbo nucifera* (Lotus) (Figure 1.1a). These plants, apart from repelling water, exhibit a self-cleaning behavior. Water droplets roll off on these surfaces with a tilt of about  $15^\circ$  taking contaminants with them. This behavior is commonly referred as the ‘lotus effect’.

Bartholtt and Neinhuis pioneered the understanding of the scientific basics behind the self-cleaning effect [5,6], based on the examination of a lotus leaf with a scanning electron microscope (SEM) and concluded that the extreme non-wetting property of these leaves arises from a hierarchical dual-scale surface structure consisting of micro bumps covered with nanoscale protuberances (Figure 1.1b).

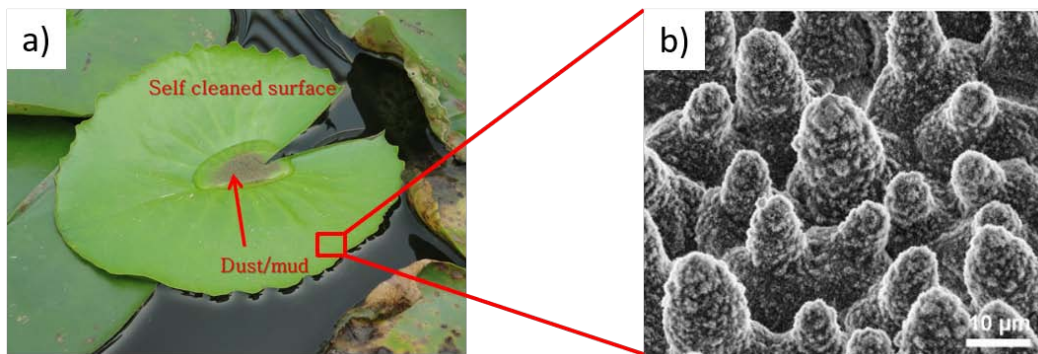


**Figure 1.1:** a) Water resting on the lotus leaf and b) typical SEM image of the surface structures on the lotus leaf [7].

The microscale bumps greatly reduce the contact area of water droplets, while the nanoscale protuberances prevent the water from penetrating into the valleys. As a result, water droplets cannot wet the lotus leaf, and roll easily off the surface (Figure 1.2).



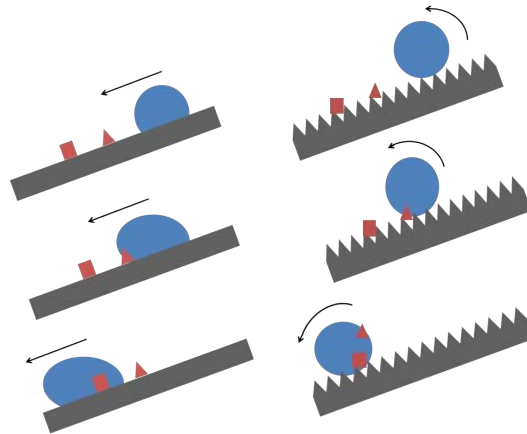


**Figure 1.2:** (Left) Water droplet sliding along a dirty hydrophilic surface. (Right) Water droplet sliding along a dirty superhydrophobic surface.

Natural superhydrophobic surfaces are not limited to the aforementioned example, in fact there are several other examples such as rose petals (Figure 1.3a) [8], gecko feet (Figure 1.3b) [9], shark skin (Figure 1.3c) [10] and butterfly wings (Figure 1.3d) [11]. The understanding of the mechanisms behind all these natural examples can provide an insight on how to address the encountered challenges for real life applications.

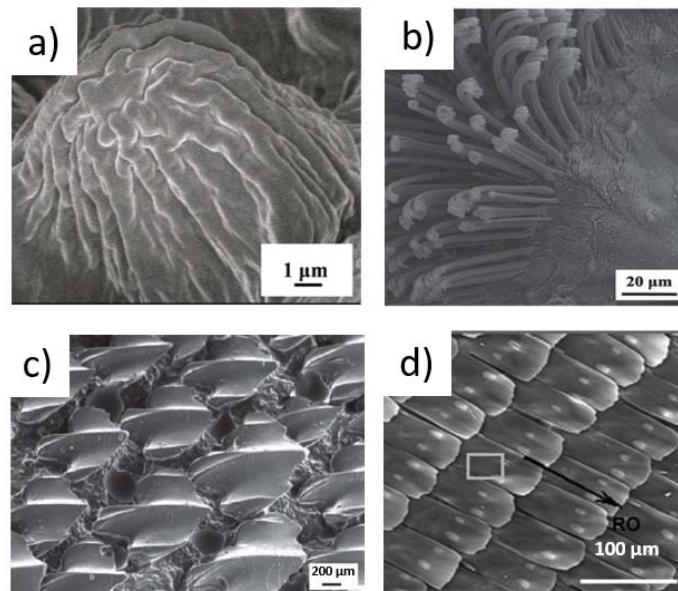


**Figure 1.3:** Examples of hierarchical structures present in the nature. The images correspond to SEM photographs of a) rose petal [8], b) gecko foot [9], c) shark skin [10] and d) butterfly wing [11].

With the rapid development of nanotechnology, these natural structures can be mimicked to create artificial superhydrophobic products for a wide range of applications, such as self-cleaning window glasses, self-cleaning textiles, anti-bacterial surfaces or localized chemical reactions [12–15].

Nevertheless, a number of issues still needs to be understood before superhydrophobic surfaces find widespread use, since artificial superhydrophobic or self-cleaning surfaces are far from being as stable as the natural surfaces. Fabricating a durable and stable superhydrophobic surface is not an easy task, two main factors have to be addresses and properly combined: one is the surface energy of the material and the other is the type of roughness imposed to the surface.

From the aforementioned observations, we noticed that the superhydrophobic properties of natural organisms are intimately linked to the micro and nanostructures on the surfaces. These kinds of hierarchical surfaces allow air to be trapped between the water droplets and the solid surfaces, significantly reducing the water contact area and the adhesion to the surfaces (Figure 1.4).

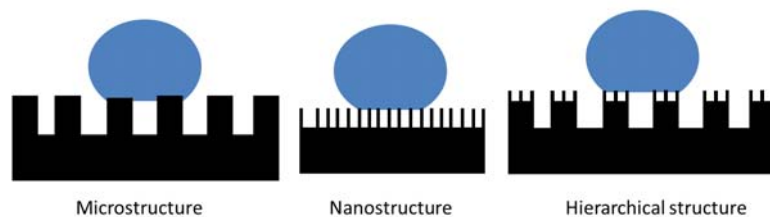


**Figure 1.4:** Schematics of wetting of the three different surfaces. The largest contact area between the droplet and the surface is given in microstructured surfaces, but is reduced in nanostructured surfaces and is minimized in hierarchical structured surfaces.

There are two methods to produce a superhydrophobic surface. The first one consists of making a rough surface from a material which is intrinsically hydrophobic. The second one relies on modifying or coating an already rough surface with a hydrophobic material. However, the second approach fails in its durability and non-toxic characteristics, hindering the possibility of using them for real life applications.

For this reason, inherently hydrophobic materials are preferred to fabricate superhydrophobic surfaces. However, this limits the spectra of the materials that

can be roughened as well as the fabrication approaches available to modify these kinds of materials. In this regard, nanoimprint lithography (NIL) is a good technique to create complex hierarchical structures, due to its high resolution, low cost, high throughput and the possibility to use different substrates materials, allowing surface structuring over transparent and flexible materials [16].

NIL has proven to be as one of the key contributors to the nanotechnology industry, which is gradually progressing from research laboratories to manufacturing process. NIL industrial processes are estimated at US\$ 1.6 billion in 2015 and is projected to reach US\$ 13.9 billion by 2020, registering a compounded growth rate of 55.4% [17].

Following the idea to deliver research findings from the laboratory to the industry, the European project PLAST4FUTURE (2012-2015) was born. The key aim of this project was to upgrade current plastic injection molding production technology for products with nanoscale texture for multifunctional surfaces. The PLAST4FUTURE manufacturing chain comprised four main components:

1. A library of multifunctional micro and nanometer topography modelled to produce functional plastic surface.
2. Process flow for cost-efficient production of nanostructured injection molding tool inserts.
3. New steel tool materials and tool fabrication processes enabling tool surfaces suitable for nanostructuring.
4. Life cycle assessment for cradle-to-cradle production philosophy.

The PLAST4FUTURE concept was based on conventional silicon wafers for the production of nanostructures, which are subsequently transferred to injection molding tools. The silicon wafer is used as a mold for a flexible stamp. The flexible stamp transfers the structures to a resist coated tool with nanoimprint lithography. Finally, the structures are defined in the tool steel by etching or electroplating. Injection molding is then performed for the mass production of polymer based products.

The research reported here was part of the PLAST4FUTURE project with the specific goal to develop self-cleaning surfaces that can be produced by injection molding. This thesis contributes on the design of hierarchical structures, as well as the implementation of the fabrication process towards producing final plastic products. The research objectives of this work were:

1. To develop a new fabrication approach to produce different hierarchical structures through rational control of the physical and chemical properties of the surface.
2. To develop a robust superhydrophobic surface using surface roughness to prevent the wetting transition without the need of chemical treatments.
3. The hierarchical surfaces will be realized inline with high volume manufacturing techniques, demonstrating the possibility of commercial applications.
4. To achieve a precise control over different wetting states by a careful control of the micro and nanostructures fabricated on the surface.
5. To develop a new fabrication technique to extend the wetting behavior to low surface tension liquids.

The thesis is divided in eight chapters. Chapter 2 introduces the fundamental concepts of wetting, from the basic Young equation to the superhydrophobicity and oleophobicity. The chapter ends with an analysis of the de-stabilization factors of a superhydrophobic surface, both from a thermodynamical and dynamical point of view.

Chapter 3 provides an analysis of the current production of superhydrophobic and oleophobic surfaces, analyzing the state of the art arising from the different fabrication methods, paying special attention to the NIL-based methods.

Chapter 4 describes the background of the manufacturing methods used during this research, divided in three main blocks: nanoimprint lithography, electroplating and injection molding.

In Chapter 5 the materials and processes needed to develop this thesis are reported. The processes presented here include those needed to fabricate the original

masters, the fabrication approaches used in this thesis, and the image and surface characterization equipments.

In Chapter 6, the newly developed fabrication methods are presented. This chapter is divided in the three main techniques followed throughout this thesis: nanoimprint-based methods, electroplating and injection molding.

In Chapter 7 the results from the wetting characterization are presented, covering stable self-cleaning surfaces, superhydrophobic surfaces with tunable wetting characteristics and the fabrication of mushroom-like structures by direct UV-NIL with superhydrophobic and oleophobic properties.

Finally, in Chapter 8 we conclude and discuss future perspectives of work.

## Chapter 2

# Fundamental Wetting Concepts

The main parameter that characterizes the wetting is the static contact angle (CA), which is defined as the angle that a liquid makes with a solid (Figure 2.1). The contact angle depends on several factors, such as surface energy, surface roughness, and its cleanliness. If the liquid wets the surface (hydrophilic surface), the value of the static contact angle is between  $0^\circ$  and  $90^\circ$ , whereas if the liquid does not wet the surface (hydrophobic surface), the value of the contact angle is between  $90^\circ$  and  $180^\circ$ .

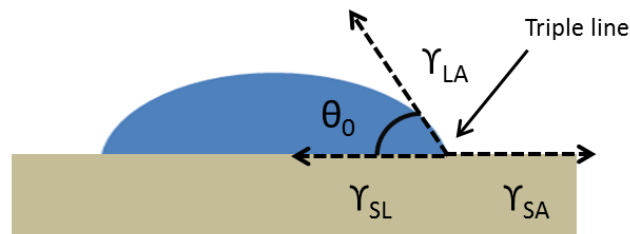


**Figure 2.1:** The contact angle  $\theta_0$  and all the surface tensions in a system consisting of a water droplet resting on a flat surface.

There are different ways to improve the inherent wetting properties of a surface. One of the ways to increase the hydrophobic or hydrophilic properties of a surface is to increase surface roughness. Wenzel (1936) [18] suggested a simple way to predict that the contact angle of a liquid with a rough surface is different from that with a smooth surface.

Later, Cassie and Baxter (1944) [19] showed that a gaseous phase, commonly referred to as ‘air’ in the literature, may be trapped in the cavities of a rough surface, resulting in a composite solid-liquid-air interface, as opposed to the homogeneous solid-liquid interface. These two models describe two major possible wetting regimes or states: the homogeneous (Wenzel) and the composite (Cassie-Baxter) regimes.

However, within the last years, new superhydrophobic states have been reported [8, 20–22], depending on contact angle and dynamic effects. Developments on the fabrication of several hierarchical structures with different combinations of micro and nanostructures helped to know that the wetting cannot be characterized by a single parameter such as the contact angle. For this reason, in this chapter we will differentiate between the classic models of wetting and the recently discovered wetting states.

## 2.1 Surface Tension and Contact Angle

The contact angle (CA) is one of the most important parameters to measure the surface wettability, and its value can be used to determine its hydrophobicity. A surface with a water contact angle below  $90^\circ$  is considered hydrophilic and a surface with a water contact angle above than  $90^\circ$  is considered hydrophobic. Furthermore, a surface is denoted superhydrophobic if its contact angle is larger than  $150^\circ$ .

In 1805, Thomas Young proposed for the first time [23] that an interface between two materials has a specific energy, the interfacial energy. This concept opened the opportunity to establish the field of wettability, which has become a hot topic in the last decades.

The molecules sitting at a surface of any material have less binding with adjacent molecules than molecules in the bulk, and therefore they have the potential to form new bonds. Materials with higher binding potential have higher wetting ability. In other words, the atoms or molecules at the surface of the liquids or solids can be treated as a relatively thin layer, in contrast to those of the bulk, because the surface atoms or molecules have fewer bonds with neighbouring atoms, and therefore, they have higher energy than similar atoms in the interior. This energy difference is attributed to the surface tension or free surface energy. This surface energy,  $\gamma$ , is

equal to the required work to create a unit area of the surface at a constant pressure and temperature. In SI units, the surface tension is measured either in energy per unit area or force per unit length, i.e.,  $J/m^2$  or  $N/m$ .

When a solid is in contact with a liquid, the molecular attraction will reduce the energy of the system so as to reach an equilibrium value which is smaller than the sum of two separated surfaces. The elimination of two surfaces to produce an interface reduces the total energy of the system. The energy of the liquid-solid-air system is reduced by an energy given by the Dupré equation [24]:

$$W_{SL} = \gamma_{SA} + \gamma_{LA} - \gamma_{SL} \quad (2.1)$$

where  $W_{SL}$  is the work of adhesion per unit area between the two surfaces,  $\gamma_{SA}$ ,  $\gamma_{SL}$  are the surface energies of the solid in contact with air and liquid, and  $\gamma_{LA}$  is the surface energy of liquid in contact with air. The place where the surface, the air and the liquid meet is called the triple line.

In the case where the solid-liquid interface energy is lower than the solid-air interface energy, the droplet will tend to spread on the surface (hydrophilic behavior). If the solid-liquid interface energy is higher than the solid-air interface energy, spreading will not occur (hydrophobic behavior).

When a liquid droplet is placed on a solid surface, the liquid and solid surfaces come together under equilibrium at a characteristic angle called the static contact angle or Young contact angle, usually denoted as  $\theta_Y$  or  $\theta_0$ . The CA can be determined by minimizing the total energy of the system of the three interfaces [24]:

$$E_{tot} = \gamma_{LA} (A_{LA} + A_{SL}) - W_{SL} A_{SL} \quad (2.2)$$

where  $A_{LA}$  and  $A_{SL}$  are the liquid-air and solid-liquid interfaces areas, respectively.

A droplet suspended in a gas phase (e.g. air) is subjected to two forces which determine its shape: the surface tension, which acts to minimize the surface area, (i.e. making the droplet spherical); and the gravitational force, which acts to flatten it. The effect of gravity can be neglected if the size of the droplet is smaller than the capillary length ( $\kappa_C$ ) [25]:



$$\kappa_C = \sqrt{\frac{\gamma_{LA}}{\rho g}} \quad (2.3)$$

here,  $\gamma_{LA}$  is the surface tension of the liquid-air interface,  $\rho$  is the density of the liquid, and  $g$  is the acceleration of the gravity. At ambient conditions, the capillary length of clean water is around 2.7 mm [25].

It is also assumed that the volume and pressure of the droplet are constant, so that the volumetric energy does not change and at equilibrium is equal to zero ( $dE_{tot} = 0$ ). With these considerations, equation 2.2 will be:

$$\gamma_{LA} (dA_{LA} + dA_{SL}) - W_{SL}dA_{SL} = 0 \quad (2.4)$$

For a droplet of constant volume, the geometrical relationship  $\frac{dA_{LA}}{dA_{SL}} = \cos\theta_0$  [24] can be used, which gives us the Young equation for the contact angle of a flat and chemically homogeneous surface:

$$\cos\theta_0 = \frac{\gamma_{SA} - \gamma_{SL}}{\gamma_{LA}} \Rightarrow \gamma_{SL} = \gamma_{SA} - \gamma_{LA}\cos\theta_0 \quad (2.5)$$

A CA of  $0^\circ$  means that the surface is totally wetted, while a CA of  $180^\circ$  corresponds to complete non-wetting. Generally, the lower the surface tension of the solid  $\gamma_{SA}$ , the higher the contact angle  $\theta_0$  of a surface.

## 2.2 Contact Angle Hysteresis

Young equation describes the behavior on a perfectly flat surface, but in reality, flat surfaces rarely exist. Surfaces have some roughness, either inherent or created. The roughness can influence the triple line and pin it, resulting in adhesion of the droplet to the surface, either slightly or completely. The concept of Contact Angle Hysteresis (CAH or  $\Delta\theta$ ) has been developed to characterize the adhesion of a water droplet to a surface.

When a droplet moves on a surface, the pinning of the triple line influences the contact angle. At the advancing part of the drop, the contact angle increases (advancing CA,  $\theta_A$ ) and for the receding part of the drop, the contact angle decreases

(receding CA,  $\theta_R$ ). Normally droplet movement can take place in two ways. One way is to tilt the surface, making the droplet move by the effect of the gravity (Figure 2.2a). When the tilt angle reaches the critical angle ( $\alpha$ ), the droplet will start moving down the plane, which is known as the roll-off or sliding angle. An alternative option to measure the contact angle hysteresis is when the droplet volume is altered by ejecting or taking out a small amount of liquid (Figure 2.2b,c).

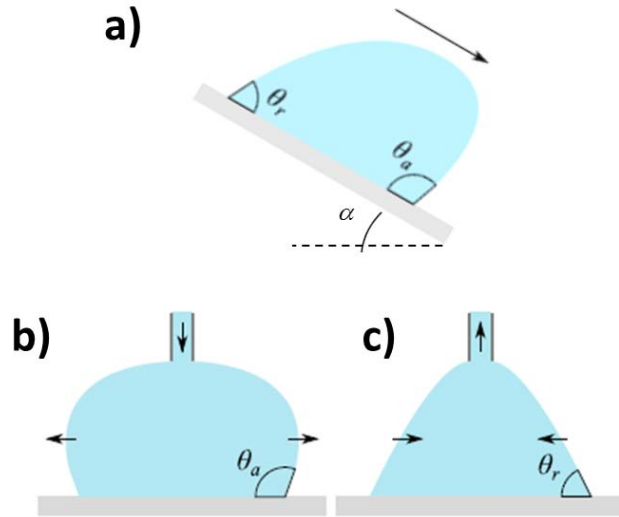


**Figure 2.2:** Advancing ( $\theta_A$ ) and receding ( $\theta_R$ ) contact angles obtained by a) tilting the surface at the critical angle ( $\alpha$ ), b) increasing the size of the droplet and c) decreasing the size of the drop.

The difference between the advancing and receding contact angles is known as the contact angle hysteresis [26, 27]:

$$\Delta\theta = \theta_A - \theta_R \quad (2.6)$$

This value gives a measure of how ‘sticky’ the surface is. The higher the CAH, the easier the water will stick to the surface. To study the fabrication of superhydrophobic surfaces and the practical application of the self-cleaning surfaces, the dynamic behavior of the liquid droplet must be considered. An ideal self-cleaning surface needs an extremely small contact angles hysteresis, that is, liquid droplets

can easily roll off on the surface [12]. Although for surfaces with roughness carefully controlled on the molecular scale it is possible to achieve contact angle hysteresis as low as  $< 1^\circ$  [28], hysteresis cannot be eliminated completely, since even atomically smooth surfaces have a certain roughness and heterogeneity. Several factors affect the hysteresis, such as liquid purity, droplet mass, surface impurities, surface roughness and surface chemical heterogeneity [29].

## 2.3 Classic Models of Wetting

By increasing the surface roughness the water droplets can be subjected to different wetting states. The inherent behavior of the material can be enhanced, increasing its hydrophobic/hydrophilic behavior. Furthermore, structuring of the material can lead to air pockets trapped between the droplet and the surface. In particular, with hierarchical structures the situation can be more complex since the droplet can wet either the microstructures, the nanostructures, none of them or both of them. In this section, we will address the classic models of wetting on a rough surface.

### 2.3.1 The Wenzel model

The correlation between surface roughness and contact angle was first examined by Wenzel in 1936 [18]. According to Wenzel, the CA of a surface is heavily influenced by its physical characteristics, namely roughness. The model is schematically depicted in Figure 2.3a, where the roughness is represented as an array of square pillars.

Wenzel proposed that a rough surface provides an additional interfacial area for the liquid, thus the CA would be different to the Young CA. The additional surface area provided by roughening the surface resulted in an increase of surface energy. Wenzel studied the effect of surface roughness on the equilibrium and suggested an equation for a water droplet in a rough surface, given by [18]:

$$\cos\theta_W = r\cos\theta_0 \tag{2.7}$$

where  $\theta_W$  is the apparent contact angle in the Wenzel state,  $\theta_0$  is the Young contact angle for a flat surface of the same material, and  $r$  is the roughness factor defined as the ratio of the actual solid-liquid area  $S_{actual}$  to its projection on a flat plane  $S_{projected}$ , as depicted in the Figure 2.3b. The value of  $r$  of a rough surface must be larger than one.

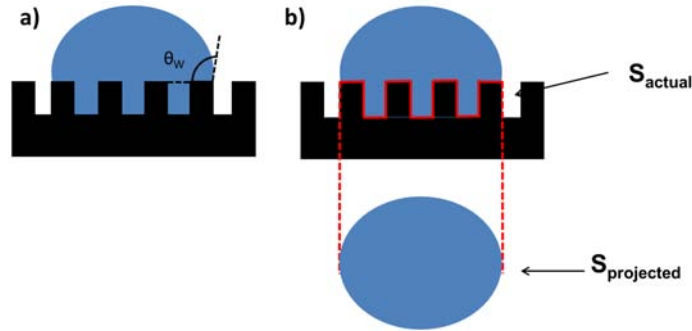


**Figure 2.3:** a) Schematic illustration of a droplet in the Wenzel state. b) Illustration of the Wenzel roughness ratio  $r$  related to the Wenzel state.

Wenzel equation indicates that the rough surface makes the actual solid/liquid contact area larger. Droplets in the Wenzel state will tend to amplify the ‘intrinsic’ behavior of the surface. In other words, when  $\theta < 90^\circ$ ,  $\theta_W$  decreases with increasing roughness and the surface becomes more hydrophilic; whereas when  $\theta > 90^\circ$ ,  $\theta_W$  increases with the increase of the roughness and the surface becomes more hydrophobic.

The dependence of the CA on the roughness factor  $r$  is schematically illustrated in Figure 2.4. The plot shows that large contact angles can be achieved for droplets in the Wenzel state. However, the droplets will be pinned to the surface by the roughness and the surface will not exhibit a self-cleaning behavior.

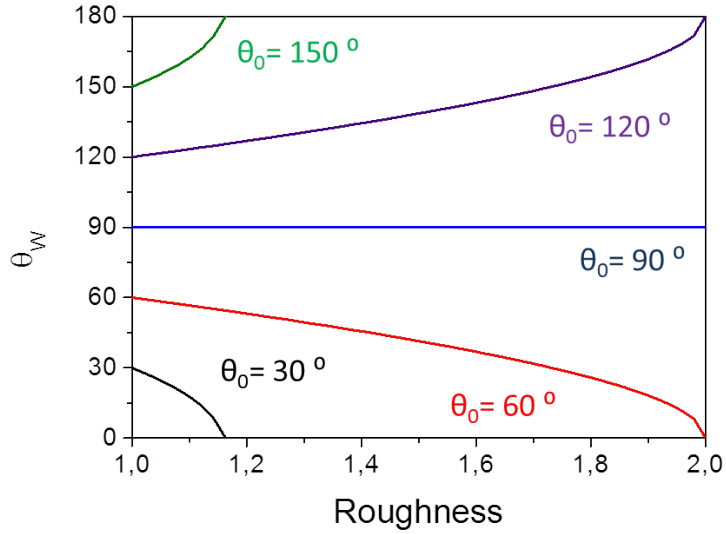


**Figure 2.4:** Contact angle ( $\theta_w$ ) as a function of the roughness factor ( $r$ ) for various CAs for a smooth surface ( $\theta_0$ ).

The trend observed in the Figure 2.4 was experimentally demonstrated by Jun and Bhushan in 2006 [30]. The bar chart in Figure 2.5a shows measured contact angles of  $5 \mu\text{l}$  water droplets deposited on both hydrophilic and hydrophobic surfaces made of poly(methyl methacrylate) PMMA. PMMA is a polymer that has polar (hydrophilic) groups with high surface energy, but they treated some PMMA films with a hydrophobic self-assembled monolayer SAM of perfluorodecyltriethoxysilane (PFDTES).

Furthermore, in addition to the PMMA films, ordered nanostructures with low and high aspect ratio (LAR and HAR) were prepared using soft lithography, as well as a replica of a lotus leaf (Figure 2.5b). These surfaces yielded a roughness factor of 2.1, 5.6 and 3.2, respectively. It can be observed that with increasing the roughness factor ( $r$ ) the water CA decreases on the hydrophilic PMMA, and increases on the hydrophobic PMMA, which is exactly what the Wenzel model predicts.

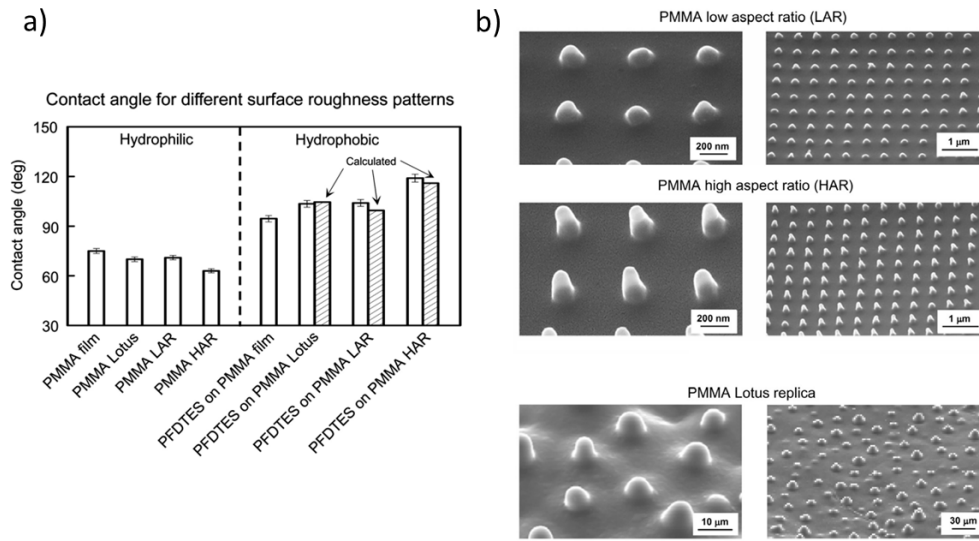


**Figure 2.5:** a) Measured contact angles on hydrophilic and hydrophobic surfaces. b) SEM micrographs of the patterned polymer surface. Both low aspect ratio (LAR) and high aspect ratio (HAR) are shown, as well as the micropatterned lotus replica [30].

### 2.3.2 The Cassie-Baxter model

The Wenzel equation relates the apparent contact angle and the intrinsic contact angle of a homogeneous rough surface. However, the equation is not valid when the surface is composed of different types of chemical substances. Cassie and Baxter [19] extended the theory presented by Wenzel and proposed that a heterogeneous rough surface could be considered as a composite surface.

Cassie and Baxter proposed that if the substrate is rough and it consists of randomly distributed ‘n’ different types of materials on the surface, it will produce a composite model where the surface properties of each part of these materials is characterized by their own surface tensions, i.e.  $\gamma_{i,SL}$  and  $\gamma_{i,SA}$  with separated area fraction  $f_i$  on the substrate satisfying the following equations:

$$f_1 + f_2 + \dots + f_n = 1 \quad (2.8)$$

$$\gamma_{SA} = \sum_i^n f_i (\gamma_{i,SA}) \quad (2.9)$$

$$\gamma_{SL} = \sum_i^n f_i (\gamma_{i,SL}) \quad (2.10)$$

Thus, a modification of the Young equation can be written as:

$$\cos\theta_{CB} = \frac{\sum_i^n f_i (\gamma_{i,SA} - \gamma_{i,SL})}{\gamma_{LA}} = \sum_i^n f_i \cos\theta_i \quad (2.11)$$

For a simple situation in which a composite surface is composed of two different types of material, and these two surfaces are not interfering with each other; their intrinsic contact angles are  $\theta_1$  and  $\theta_2$ , and  $f_1$  and  $f_2$  are their fractions on a unit area ( $f_1 + f_2 = f$ ). If we combine the Young and the Wenzel equations [4]:

$$\cos\theta_{CB} = f_1 \cos\theta_1 + f_2 \cos\theta_2 \quad (2.12)$$

For a composite interface consisting of a solid–liquid fraction ( $f_1 = f_{SL}$ ,  $\theta_1 = \theta_0$ ) and liquid–air fraction ( $f_2 = f_{LA} = 1 - f_{SL}$ ,  $\theta_2 = -1$ ), the equation 2.12 can be rewritten as:

$$\cos\theta_{CB} = f_{SL} \cos\theta_0 - f_{LA} = f_{SL} (\cos\theta_0 + 1) - 1 \quad (2.13)$$

where  $\theta_{CB}$  represents the Cassie-Baxter contact angle and  $f_{SL}$  represents the fraction of the solid in contact with the liquid, as it shown in the Figure 2.6b.

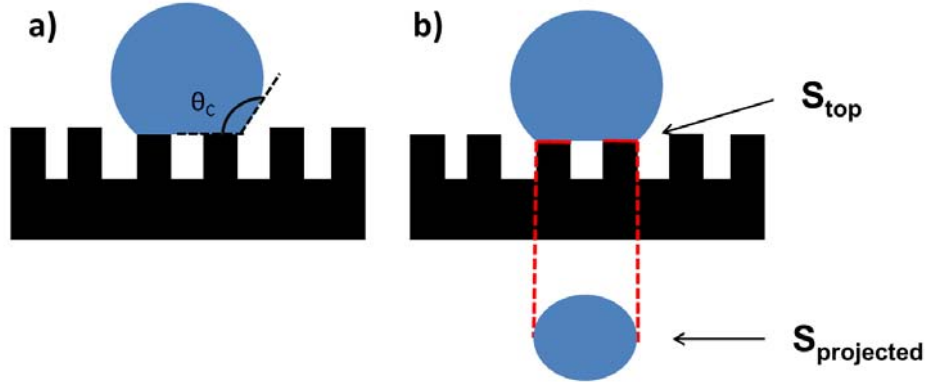


**Figure 2.6:** a) Schematic illustration of a droplet in the Cassie-Baxter state. b) Illustration of the solid-liquid contact fraction  $f_{SL}$  defined in the Cassie-Baxter equation.

When a water droplet rests on top of the surface asperities, the surface tension is reduced, and this leads to an increase in the CA. In this situation, air can be trapped in between the features (Figure 2.6a), so the liquid droplet rests on a surface with a distribution of solid asperities and air-pockets. According to the Cassie-Baxter equation, it is possible to tailor the surface topography to let the solid fraction  $f_{SL}$  approach zero by introducing asperities on the surface and making the contact angle close to  $180^\circ$ .

## 2.4 Stability of the Superhydrophobicity

Since superhydrophobicity requires a stable composite (Cassie-Baxter) interface, it is important to understand the destabilization mechanisms for the Cassie-Baxter and Wenzel wetting transition. If the Cassie state collapses and water penetrates into the structures, the droplet will transfer into the Wenzel state. A droplet in the Wenzel state will be difficult to move because of the increased adhesion force from the increased liquid surface contact area and the hysteresis would be much larger than for droplets in the Cassie state. Many factors can influence the collapse of the Cassie state. The rate at which water penetrates into the structures will vary for



different materials, geometries and external stimuli.

The transition of a liquid-air interface to the Wenzel state is governed by the mutual free energy values of the possible wetting states (Cassie and Wenzel). The transition from one wetting regime to the other occurs by one of two possible mechanisms, sag or depinning (Figure 2.7). In the case of the sag mechanism, the borders of the roughness valleys pins the liquid, thereby causing a part of the liquid-air interface to sag owing to a external force (Figure 2.7a) [31, 32]. If the external forces acting on the solid-liquid contact overcome the shear forces, the solid-liquid contact area becomes depinned from the borders of the roughness feature, and the corresponding mechanism is called depinning (Figure 2.7b) [33, 34]. The intermediate state that takes place between the pure Cassie and the pure Wenzel is called ‘metastable Cassie state’ [35–37]. A metastable Cassie state is characterized by its penetration depth, i.e., the degree of liquid penetration inside the valleys created by the roughness and the geometric configuration of the liquid-air interface. The metastable Cassie states attained via sag and depinning mechanisms are also termed as the sagged state and depinned state, respectively.

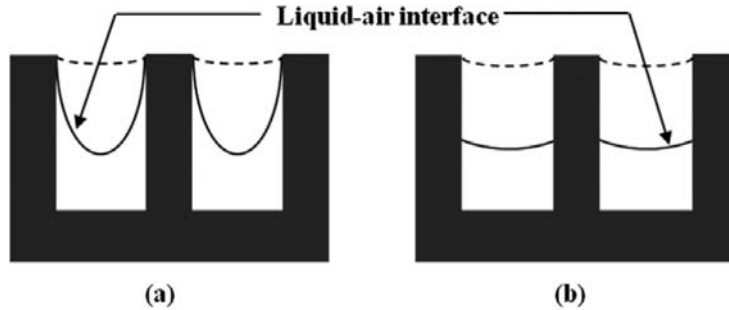


**Figure 2.7:** Mechanisms showing transition from Cassie to Wenzel states: a) sag mechanism and b) depinning mechanism [34].

Intensive research has been conducted during the last years to identify the factors for the Cassie-Baxter stability. The robustness of the heterogeneous wetting regime can be investigated from the dual perspectives of thermodynamics and mechanics. We will address below the factors that affect the stability of the Cassie state from the two points of view.

### 2.4.1 Thermodynamic Analysis

From a thermodynamic point of view, the equilibrium states are the minima of Gibbs free energy of the droplet lying on a rough surface. The global minimum corresponds to a stable state, while the other minima correspond to metastable states [38]. This trend is depicted in Figure 2.8.

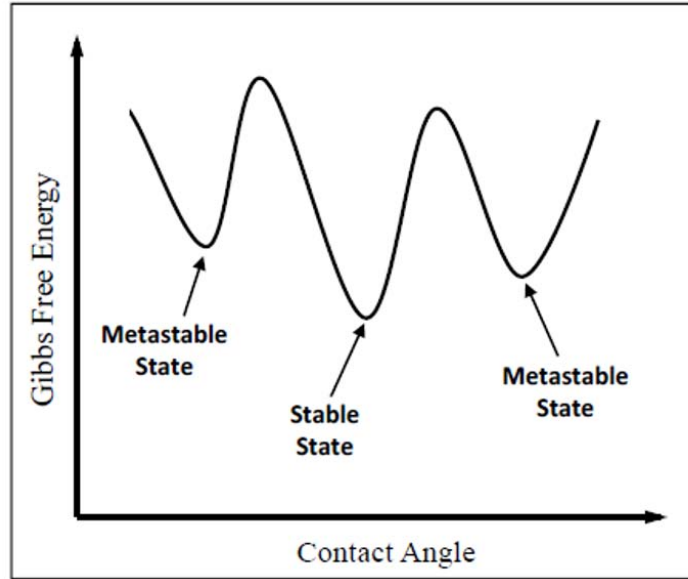


**Figure 2.8:** Multiple minima of the Gibbs energy of a droplet deposited on a rough surface.

The Cassie state, metastable Cassie states (multiple for various penetration depths and different configurations of the liquid-air interface) and the Wenzel state can be sequentially encountered as the liquid-air interface penetrates the roughness valleys. At constant temperature and pressure, the droplet starts with the Cassie state and settles at the wetting state with the lowest free surface energy. Additionally, the relative values of free surface energy need to be considered for each wetting state with respect to another wetting state.

For a sagged state, pinning of the liquid-air interface under the droplet results in a rise of liquid-air interfacial area and free surface energy. For a depinned state, the liquid occupies the sidewalls of the surface topology, thereby raising the total free surface energy. Hence, the surface energy of any metastable Cassie state (depinned or sagged) is higher than that of the Cassie state.

A transition from Cassie state to Wenzel state is possible if the droplet can

overcome the energy barrier separating the Cassie and Wenzel states. The rougher the surface is, the higher the energy barrier between the Cassie and Wenzel states, and the more stable the Cassie state is.

Due to this fact, we assume that the metastable Cassie state acts as an energy barrier in the transition to a Wenzel state. Transition between the different thermodynamic states may occur if the energy barrier needed to surmount the minima of Gibbs energy is achieved. This energy can be surmounted by applying external forces, such as pressure, electric voltage, vibration or droplet impact [39–45].

It has been suggested that the transition takes place when the net surface energy of the Wenzel regime becomes equal to that of the Cassie–Baxter regime or, in other words, when the contact angle predicted by the Cassie–Baxter equation is equal to that predicted by the Wenzel equation. Hence, the Cassie–Baxter state is the most stable state if the CA satisfies the following condition [44, 46]:

$$\cos\theta_C \geq \frac{f_{SL} - 1}{r - f_{SL}} \quad (2.14)$$

where  $\theta_C$  is the critical intrinsic CA of the flat surface above which a stable composite state is possible. When the CA of the flat surface  $\theta_0$  is larger than  $\theta_C$  ( $\theta_0 > \theta_C$ ), the Cassie state is more stable; otherwise when  $\theta_0 < \theta_C$ , the Wenzel state is thermodynamically more favourable.

This equation relates the surface topography with the chemistry of the material, since it is observed that the higher the contact angle of the flat surface, the lower the roughness necessary to achieve a stable superhydrophobic surface. This relationship is depicted in the Figure 2.9, where the dotted line represents the meta-stability.

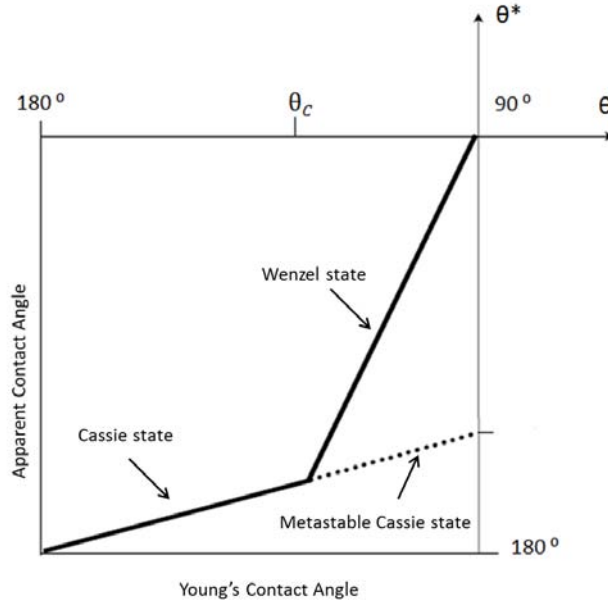


**Figure 2.9:** Apparent contact angle  $\theta^*$  plotted in function of the Young CA, denoted by  $\theta$ . Theoretically, the Wenzel state exists when  $90^\circ < \theta < \theta_C$ , and the Cassie-Baxter state exists when  $\theta_C < \theta < 180^\circ$ . However, the Cassie-Baxter state can also be observed for  $\theta < \theta_C$ , shown by the dotted line after the critical point.

### 2.4.2 Dynamic Analysis

The force (pressure) based approach (i.e., the forces experienced by the droplet and the surface) analyzing the stability of a superhydrophobic surface is possible in parallel with the energy-based one. To analyze the criteria for having a stable superhydrophobic surface, a pressure balance is carried out, which lists the pressure acting on the surface, i.e., the wetting pressures ( $P_{wetting}$ ) and the pressures exerted by the surface, i.e. the antiwetting pressures ( $P_{antiwetting}$ ). If the pressure imparted by the droplet on the surface ( $P_{wetting}$ ) exceeds the surface energy required to penetrate a unit volume of roughness valleys ( $P_{antiwetting}$ ), a wetting transition can be observed.

The antiwetting pressure ( $P_{antiwetting}$ ) corresponds to the energy difference between the homogeneous (Wenzel) and heterogeneous (Cassie) wetting regimes [47,48], the energy barrier that has to be surmounted in order to provoke the wetting transition. The  $P_{antiwetting}$  will depend of the material and the structures imposed to the surface. More details on the form of the antiwetting pressure will be given in

the Chapter 7.

On the other hand, there exist two independent and unique definitions for the wetting pressure ( $P_{wetting}$ ). The first definition of wetting pressure attributes the wetting pressure to the droplet weight and droplet curvature, and it is associated with the Laplace pressure. The second definition of wetting pressure involves the external possible stimuli than can be applied to the droplet [47–52].

When a droplet is resting in the Cassie state and a external force is applied, the meniscus will start to move down into the structures. The shape of the meniscus is spherical as long as the dimension of the droplet is smaller than the capillary length of water ( $\approx 2.7\text{ mm}$ ).

The shape of the meniscus can be calculated from the Young Laplace equation for a given pressure [53]:

$$\Delta P = \gamma_{LA} \left( \frac{1}{R_1} + \frac{1}{R_2} \right) \quad (2.15)$$

where  $R_1$  and  $R_2$  are radii of curvature and  $\Delta P$  is the change in pressure over the liquid-gas interface. For droplets or structures with circular shape, equation 2.15 reduces to:

$$\Delta P = \frac{2\gamma_{LA}}{R} \quad (2.16)$$

An increase in pressure will decrease the radius of curvature for the meniscus enabling the meniscus to penetrate deeper into the structures. During this process, the sidewall contact angle will increase. A schematic drawing of a meniscus at a given contact angle is shown in Figure 2.10.

The structure size becomes an important factor when designing superhydrophobic surfaces. Short structures can be problematic since the meniscus might touch the bottom of the structures, and thereby lead to a transition into the Wenzel State. As a general rule, taller structures will perform better than shorter ones, since the meniscus will have to penetrate deeper into the structures before the liquid transits into the non-recoverable Wenzel State.

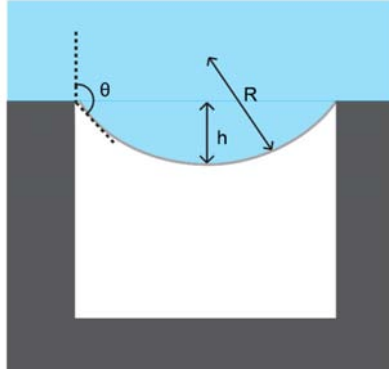


**Figure 2.10:** Cross-section of the meniscus on a pillar structure;  $R$  is the radius of curvature of the meniscus,  $h$  the penetration of the meniscus and  $\theta$  is the contact angle.

## 2.5 Superhydrophobic States

The above mentioned wetting models depict only two specific and ideal situations. In the last years, several new wetting states have been experimentally observed. Partial wetting states have been observed [54, 55]. Furthermore, for the case of hierarchical structures, the droplet can wet either the microstructures, the nanostructures, none of them, or both of them [8, 20]. Actually, pure Cassie and Wenzel wetting situations are rare in occurrence [56].

Marmur introduced a mixed wetting state [54, 55], in which a droplet partially wets the side surfaces of asperities and partially sits on air pockets, as depicted in Figure 2.11. The CA is supplied in this case by:

$$\cos\theta = R_f f_{SL} \cos\theta_0 - 1 + f_{SL} \quad (2.17)$$

where  $R_f$  is the roughness of the portion of the solid that is touching the liquid. When  $f_{SL} = 1$ , the equation 2.17 is reduced to the Wenzel equation. This state is the most common one on real surfaces, which always have some irregularities, either physical or chemical.

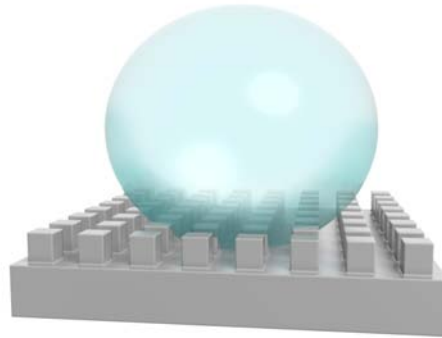


**Figure 2.11:** Schematic illustration of a droplet in the mixed state. The droplet partially penetrates into the cavities.

Recent experimental findings and theoretical analyses made it clear that the early Wenzel and Cassie-Baxter models do not explain the complexity of interactions during wetting of a rough surface which can lead to different scenarios [8,20–22,57,58]. Wang and Jiang (2007) [57] suggested five superhydrophobic states: Wenzel state, Cassie state, the ‘Lotus’ and ‘Gecko’ states, and a transitional state between Wenzel and Cassie states, as depicted in Figure 2.12.

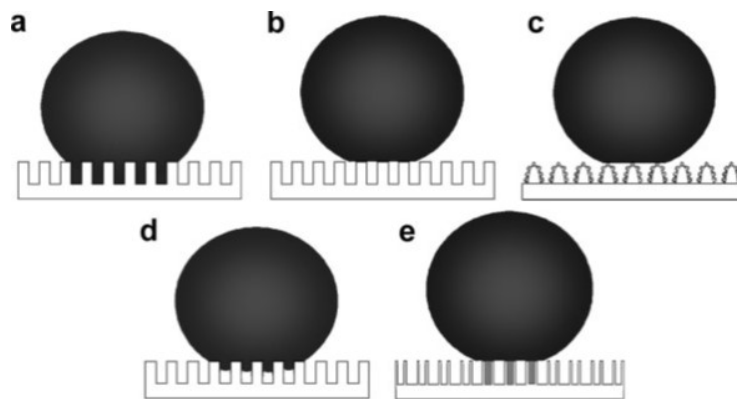


**Figure 2.12:** Different states of superhydrophobic surfaces proposed by Wang and Jiang [57]: a) Wenzel state, b) Cassie superhydrophobic state, c) the ‘Lotus’ state (a special case of Cassie superhydrophobic state), d) the transitional superhydrophobic state between Wenzel and Cassie states, and e) the ‘Gecko’ state, characterized by a large adhesive force.

Bhushan and Nosonovsky (2010) [20] pointed out that for a hierarchical surface, with nanoscale roughness superimposed on microscale roughness, there can exist nine modes of wetting depending on whether water penetrates in micro and/or nanostructures. As a result, there are several modes of wetting of a rough surface (Figure 2.13). Therefore, wetting cannot be characterized by a single number such

as the CA. The adhesion of the drop, i.e., the CAH, is a very important factor to consider.

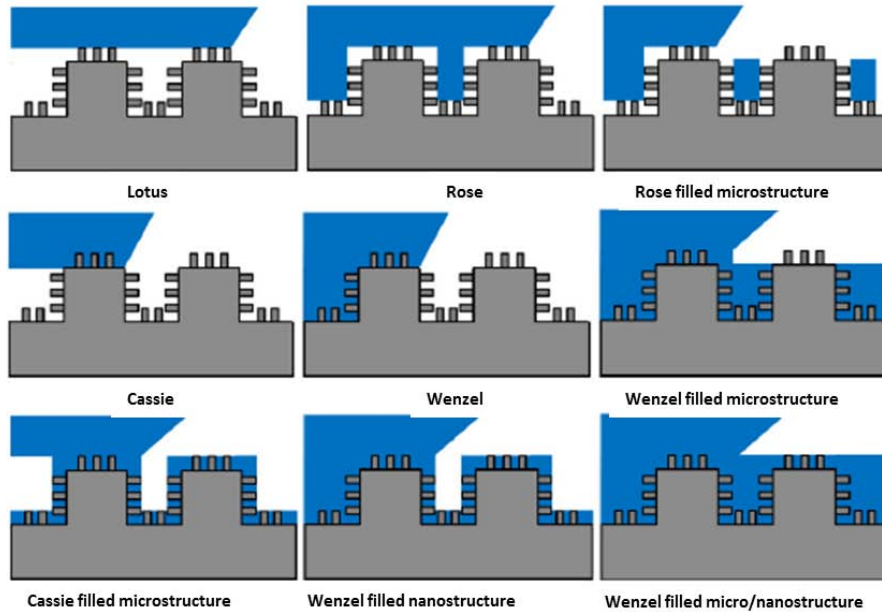


**Figure 2.13:** Schematics of nine wetting regimes for a rough surface characterized proposed by Bhushan and Nosonovsky [20], characterized by no penetration, partial penetration, and complete penetration of water into microroughness, nanoroughness and both micro and nanoroughness.

The CA is a macroscale parameter characterizing wetting behavior. However, the wetting behavior is also dependent of the adhesion of water molecules to the solid. On the one hand, a high CA is a sign of low liquid–solid adhesion. On the other hand, a low CA hysteresis is a sign of low liquid–solid adhesion as well. However, it has been recently observed that a surface can be superhydrophobic and at the same time strongly adhesive to water. The phenomenon of large CA values and high water adhesion have been observed on rose petals [8, 20]. This state is named ‘rose petal’ effect, where the water droplet coming in contact with the surface can impregnate the microstructure but no the nanostructure.

These special surface have demonstrated to be useful in several applications, such as transporting small volumes of aqueous solution without loss of liquid, localized chemical reactions or microfluidic lab-on-a-chip devices [59, 60].



## 2.6 Effect of Hierarchical Roughness

Many natural superhydrophobic surfaces have hierarchical or multiscale roughness usually built of nanostructures superimposed to microstructures. Although superhydrophobicity has been observed on single-scale (non-hierarchical) surfaces, it is believed that the hierarchical structure is very essential for robust superhydrophobic surfaces. The reason for that is that wetting is a multiscale phenomenon. The hierarchical (multiscale) roughness is needed to deal with processes at various scale levels and, in particular, to maintain a stable composite interface.

In order to form a stable composite interface with air pockets between solid and liquid, the destabilizing factors such as capillary waves, nanodroplet condensation, surface inhomogeneity, and liquid pressure should be avoided. These factors are described below:

- First, the capillary waves at the liquid–air interface may destabilize the composite interface. Due to an external perturbation, a standing capillary wave can form at the liquid-air interface. If the amplitude of the capillary wave is greater than the height of the asperity, the liquid can touch the valley between the asperities [61]. The effect of capillary waves is more pronounced for small asperities with height comparable with wave amplitude.
- Second, nanodroplets may condensate and accumulate in the valleys between asperities and eventually destroy the composite interface. Cheng et al. (2005) [62] observed condensation of submicron-sized droplets on a Lotus leaf surface and found that droplets tend to condense at areas adjacent to bumps (i.e. in the valleys) and have a contact angle of less than  $90^\circ$ , whereas larger droplets have higher contact angles, thus demonstrating that the contact angle is scale-dependent.
- Third, even hydrophobic surfaces are usually not chemically homogeneous and can have hydrophilic spots. It is known from experiments that for droplets of submicron size, the value of the contact angle is usually smaller than for droplets at the macroscale. Checco et al. (2003) [63] suggested that surface

inhomogeneity is responsible for this scale effect, since nanodroplets tend to sit at the highest free surface energy (most hydrophilic) spots and thus have lower contact angles.

Nosonovsky and Bhushan, between 2007 and 2008 [35, 64–66], demonstrated that a combination of microroughness and nanoroughness (multiscale roughness) can help resist the destabilization by pinning the interface. It also helps in preventing the gaps between the asperities from filling with liquid. The effect of roughness on wetting is scale-dependent, and the mechanisms that lead to destabilization of a composite interface are also scale-dependent. To effectively resist these scale-dependent mechanisms, it is expected that a multiscale roughness is optimum for superhydrophobicity. A microstructure resists capillary waves present at the liquid-air interface. A nanostructure prevents nanodroplets from filling the valleys between asperities and pin the drop. A combination of microstructures and nanostructures can help resist the destabilization by pinning the interface. Based on the modelling and observation of natural objects, it is widely accepted that a hierarchical surface structure is needed to develop a composite interface with high stability.

Furthermore, a hierarchical surface helps to decrease the total solid-liquid contact fraction of the solid without being affected the robustness. For a hierarchical micro nanostructure, the solid-liquid fraction of the solid surface in contact with a liquid is calculated by multiplying the area fraction of the microstructure and the area fraction of the nanostructure (Figure 2.14) [67]. As a result, the solid-liquid contact fraction of a two-level structure in contact with a liquid is much smaller than that of a single-level structure.

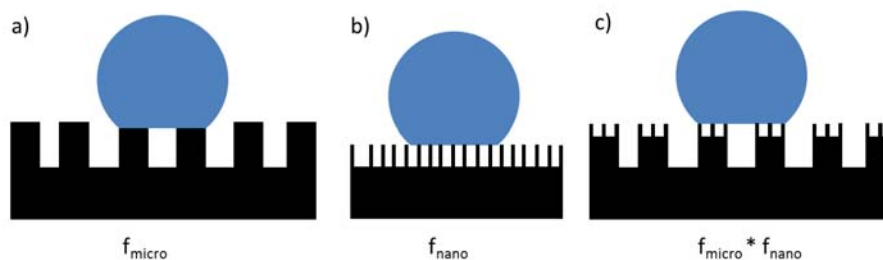


**Figure 2.14:** The solid-liquid fraction of a microstructure, a nanostructure, and a hierarchical micro nanostructure in contact with a drop.

## 2.7 Special wetting: Oleophobicity

While there are several natural and engineered super water repellent surfaces, it is very challenging to find natural oleophobic surfaces that could survive against organic liquids. This is because organic liquids are non-polar and they typically have low surface tension in comparison to that of water consisting of polar  $H_2O$  molecules, as depicted in Table 2.1.

<i>Liquid</i>	<i>Surface Tension (mN/m)</i>
Water	71.99
Diiodomethane	50.80
Ethylene glycol	47.70
Peanut oil	32.23
Olive oil	32.03
Hexadecane	27.05

**Table 2.1:** Surface tension of common liquids used to assess repellency of a surface [68].

The only natural example of texture with oleophobic properties has recently been observed in springtails [69]. However, a natural surface with repellency to liquids with surface tensions  $< 30 \text{ mN/m}$  has yet to be found.

To design a oleophobic surface it is not sufficient to fabricate a low energy surface with a high roughness on the nano or micrometer scale. The fundamental difference

between water and non-polar liquids is the contact angle on flat low-energy surfaces. Water can form a contact angle above  $90^\circ$  with these surfaces. In contrast, no flat surface exists that forms a contact angle larger than  $90^\circ$  with non-polar liquids.

Numerous studies have demonstrated that fabricating superhydrophobic surfaces with water contact angles greater than  $150^\circ$  and low contact angle hysteresis is relatively a simple process. However, engineering surfaces that show low affinity toward most of the low surface tension liquids, like hexadecane, is not achievable unless re-entrant or overhanging structures in addition to surface roughness and low surface energy are provided [68, 70] (Figure 2.15b).

To illustrate this qualitatively, consider the two types of textures shown in Figures 2.15a and b, both having the same solid surface tension. The texture shown in Figure 2.15a is concave (texture angle  $\psi > 90^\circ$ ) and the texture shown in Figure 2.15b is convex (texture angle  $\psi < 90^\circ$ ) facing upwards. In both cases, any liquid contacting the texture in the Cassie–Baxter state locally displays a contact angle equal to the Young contact angle  $\theta$ . A stable Cassie–Baxter state results only when  $\theta \geq \psi$  [68, 71, 72].

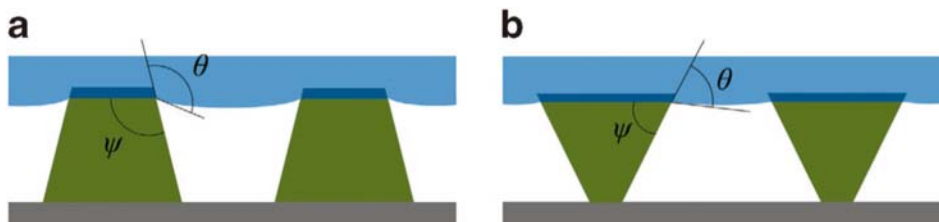


**Figure 2.15:** a) A schematic of a concave texture ( $\psi > 90^\circ$ ) showing a liquid droplet with  $\theta > 90^\circ$  in the Cassie–Baxter state. b) A schematic of a convex texture (re-entrant texture,  $\psi < 90^\circ$ ) showing a lower surface tension liquid with  $\theta < 90^\circ$  in the Cassie–Baxter state.

This is because if  $\theta < \psi$ , the net traction on the liquid–vapor interface is downward due to the capillary force, which promotes penetration of the liquid into the solid texture, leading to a fully wetted Wenzel state. Consequently, low surface tension liquids, which display a Young contact angle  $\theta < 90^\circ$ , cannot be in a stable Cassie–Baxter state on textures with  $\psi > 90^\circ$  (Figure 2.15a). However, they can be in a robust Cassie–Baxter state on textures with  $\psi < 90^\circ$  (Figure 2.15b). Such convex topographies, with  $\psi < 90^\circ$ , are called re-entrant textures.

However, it must be noted that re-entrant texture that enables the condition

$\psi \leq \theta$  for low surface tension liquids, is a necessary but not sufficient condition for the formation of a robust Cassie–Baxter state.

Re-entrant topography should be combined with low surface energy materials. According to Nishino et al. [73], the surface energy provided by hexagonally packed  $-CF_3$  groups is the lowest possible, thus fluorinated coatings are commonly used to lower this surface tension. The most famous non-sticky material is Teflon, a derivative of polytetrafluoroethylene. However, there is a drawback in using hydrophobic coatings, since, due to their low surface energy, it is difficult to attach them to the substrate, which limits the durability of such coatings.

## Chapter 3

# Realization of Surfaces with Special Wetting

### 3.1 Superhydrophobic Surfaces

Onda et al. (1996) [74] were the first to report the synthesis of an artificial superhydrophobic surface by using alkylketene dimer wax with a water contact angle of  $174^{\circ}$ . Their paper was the start of an explosion in the number of published papers on artificial superhydrophobic surfaces. From then, a number of studies have been carried out to replicate the water biomimetic effect for a wide range of applications. Some studies have pure scientific value and are focused on improving the understanding and knowledge of the superhydrophobic effect, while others focused on applications.

The two main requirements for a superhydrophobic surface are that the surface should be rough and that it should be hydrophobic (low surface energy). These two requirements lead to two methods of producing a superhydrophobic surface: first, to make a rough surface from an initially hydrophobic material and, second, to modify a rough hydrophilic surface by modifying the surface chemistry or applying a coating of hydrophobic material on it.

There are several methods to create surface roughness, however, only few of the are limited to inherent hydrophobic materials, such as polydimethylsiloxane (PDMS) or polytetrafluoroethylene (PTFE). Modifying the surface chemistry with

a hydrophobic coating opens the possibility to impose superhydrophobicity over a wide range of different materials. However, these methods usually include toxic materials and have a limited life time.

Depending on the type of procedure that is used to fabricate the surfaces, these methods can be categorized as *top-down* or *bottom-up* approaches. A top-down approach refers to the generation of superhydrophobic surfaces with preferred shapes and characteristics, starting on a larger scale, where the surface topography required for the condition of superhydrophobicity is imparted through the removal of material, using, for example, etching techniques. Conversely, bottom-up approaches tend to employ additive approaches whereby the topographical conditions for superhydrophobicity are achieved through the nanoscale assembly of structures.

### 3.1.1 Top-down Techniques

To produce superhydrophobic rough surfaces by top-down techniques, various methods have been used including lithography, plasma treatment, injection molding and laser ablation, among others. These methods are briefly discussed below:

#### Lithography

Lithographic techniques such as electron beam lithography, micro/nano nanosphere lithography, photolithography and block-copolymer lithography are used in the development of different surfaces, where micro and nanopatterns are transferred from the master to the substrate surface. This technique is generally used for making superhydrophobic surfaces where the shapes of features and patterns are well defined.

Electron beam lithography (EBL) is a commonly used lithographic technique for the fabrication of surfaces with high WCAs. EBL offers significant advantages toward the development of hierarchical structures due its high precision. The hierarchical structures fabricated by EBL are particularly useful for gaining a better understanding of the concept of superhydrophobic surfaces, as they offer the ability to fabricate well-defined primary microstructures with secondary nanostructures [75,76]. However, it is not a suitable technique for real life applications, due to its high cost

and slowness.

Micro/nano sphere lithography is an emerging technique, due to its low cost in comparison with conventional lithographic techniques. This process involves the use of particles as removable templates. Recent studies have reported that nanostructured surfaces fabricated using an organic template such as polystyrene (PS) can produce surfaces that exhibit WCAs as high as  $150^{\circ}$ .

Li et al. (2010) [77] reported superhydrophobic and antireflective silica surfaces fabricated with PS microspheres as a template. The morphology of the silica micropillars was changed by varying the reactive ion etching (RIE) time. Contact angles of  $151^{\circ}$  were achieved after silanization with trichloro-(1H,1H,2H,2H-perfluorooctyl) (Figure 3.1a).

Park et al. (2012) [78] fabricated hierarchical superhydrophobic surfaces over fluorinated silicon consisting on patterned micro/nano rod hierarchical structures. The structures were fabricated by a combination of the two-step microsphere lithography–RIE and nanosphere lithography–RIE processes. Contact angles of  $160^{\circ}$  were achieved with a microrod structure with diameter, distance and height of  $840\text{ nm}$ ,  $2\ \mu\text{m}$  and  $1\ \mu\text{m}$  respectively; and with a nanorod structure with diameter, distance and height of  $150\text{ nm}$ ,  $420\text{ nm}$  and  $250\text{ nm}$  respectively (Figure 3.1b).

Wang et al.(2015) [79] fabricated vertically aligned hierarchical hair arrays on a PMMA substrate using PS sphere lithography combined with oxygen plasma reactive ion etching. After fluorination, the hierarchical hair arrays exhibit a maximum water contact angle of nearly  $160^{\circ}$  (Figure 3.1c). Furthermore, the planar PMMA plate covered with the hierarchical hair arrays presents a large loading capacity on a water surface, as well as a stable behavior over impacting droplets.



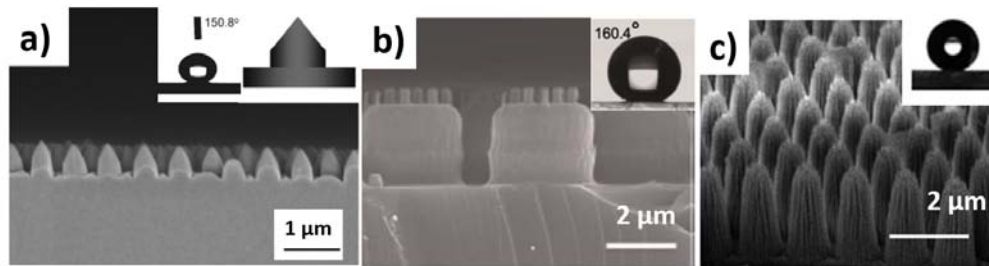


**Figure 3.1:** SEM image and WCA images of a) silica micropillars [77], b) silica micro nano rod hierarchical structure and [78] and c) vertically aligned hair arrays of PMMA [79].

Other lithographic techniques have been used to obtain well-defined superhydrophobic surface. Park et al. (2012) [80] designed antireflective silica surfaces with superhydrophobic behavior. They prepared nanotextured silica surfaces presenting conical feature by interference lithography (Figure 3.2a). The surfaces presented superhydrophobicity after chemical vapor deposition of 1H,1H,2H,2H-perfluorodecyltrichlorosilane. The surfaces exhibited an excellent behavior over impacting droplets.

Checco et al. (2014) [81] reported a block-copolymer based fabrication approach for creating robust water repellent surfaces with well-defined textures at the 10 nm scale. A tapered cone geometry (Figure 3.2b) provides optimal superhydrophobic behavior with large static water contact angles, low hysteresis and resistance to water infiltration under high pressure.

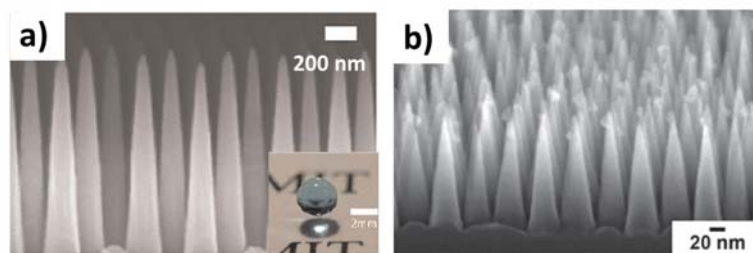


**Figure 3.2:** SEM image and WCA images of a) nanocone structure of fused silica surface [80] and b) nanocone array made by means of block-copolymer lithography [81].

## Etching

A number of etching techniques have been applied to various substrates for precise fabrication of engineered surfaces. Plasma etching of polymeric substrates is an effective method for the fabrication of superhydrophobic surfaces, as it involves the use of highly reactive plasma species to modify the surface functionality of the substrate [82]. The scientific advantage of using this technique lies in the fact that the plasma etching method can be used in conjunction with other fabrication techniques such as lithography to create the desired surface. Plasma reactive processes, such as deep reactive ion etching (DRIE), use chemically reactive ionized gases generated from an electromagnetic field to fabricate surfaces that exhibit superhydrophobicity.

This technique results in a etched uppermost surface, giving rise to the formation of defined structures such as nanopillars or nanocones [83]. The surface features significantly change upon variation of the etching parameters, such as the etching gas ratio, reaction exposure time, and applied power. Considerable differences in the hydrophobicity of the surface can result. *Black Silicon* is one of the most used structures which leads to superhydrophobicity [84, 85].

Like other etching techniques, the femtosecond laser irradiation process is also used for roughening surfaces. Yong et al. (2014) [86] developed line-patterned polydimethylsiloxane (PDMS) surfaces which exhibited superhydrophobicity and controllable water adhesion (Figure 3.3a).

Ta et al. (2015) [87] fabricated superhydrophobic copper and brass surfaces. The wettability of the textured surfaces develops from hydrophilicity to superhydrophobicity overtime when exposed to ambient conditions. The change in the wetting property is attributed to the partial deoxidation of oxides on the surface induced during laser texturing. They achieved textures exhibiting contact angles up to  $152^\circ$  with contact angle hysteresis of around  $3 - 4^\circ$  (Figure 3.3b).

Ellinas et al. (2014) [88] developed superhydrophobic and superoleophobic polymeric surfaces through a plasma texturing process and a subsequent grafting of self-assembled perfluorododecyltrichlorosilane monolayers (SAMs).

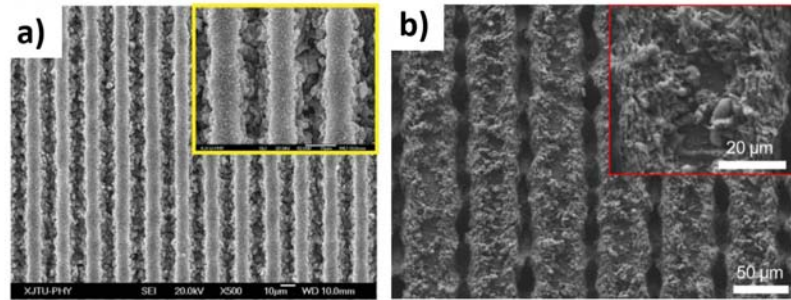


**Figure 3.3:** SEM image and WCA images of a) line-patterned PDMS surfaces [86] and b) laser textured brass surface [87].

### Anodic Oxidation

Anodization methods have been applied to metallic substrates to generate porous nanoscale structures, on substrates such as aluminum and copper. Films with high uniformity and pore density can be readily obtained from aluminum metal by adjusting the preparation parameters. It has also been observed that superhydrophobicity can be induced by the fabrication of an array of dead-end nanopores on the metallic surface. These dead-end nanopores act as ‘air-pockets’ and help to strike a balance between the adhesion properties and the hydrophobicity of the surface (Park et al. (2010) [89]).

Anodic oxidation in combination with etching techniques give good results on metallic superhydrophobic surfaces (Wu et al. (2015) and Ganne et al. (2016) [90,91]).

#### 3.1.2 Bottom-up Techniques

The most common methods of this approach to fabricate superhydrophobic surfaces are hydrothermal deposition, chemical vapor deposition (CVD), electrospinning, sol-gel and others. Some of these techniques are briefly discussed below.

### Hydrothermal Reaction

Hydrothermal reaction is recognized as an efficient method for the production of superhydrophobic materials with a variety of patterns and morphologies. Hydrothermal reactions are relatively simple to design, since the additional problem associated with creating a specific template can be avoided.

Gong et al. (2014) [92] fabricated hierarchical structures by growing ZnO nanowires on micro scale silicon pyramids. A water contact angle as high as  $169^{\circ}$  with a contact angle hysteresis less than  $13^{\circ}$  was formed by growing ZnO nanowires of a suitable length on silicon micro pyramids (Figure 3.4a).

Wang et al (2014) [93] fabricated  $\gamma$ -AlOOH nanoflakes on glass substrates. After a treatment with trichloro(1H,1H,2H,2H-perfluorooctyl) silane (PFOS) the surfaces exhibited a contact angle of  $160^{\circ}$  and a sliding angle of  $3^{\circ}$  (Figure 3.4b).

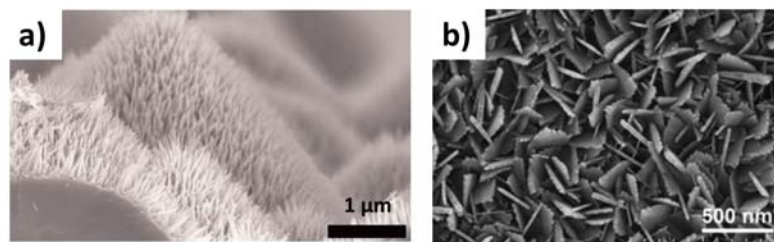


**Figure 3.4:** SEM images of a) hierarchical structure surfaces with ZnO seed layer on silicon pyramid surfaces [92] and b) nanoflake film grown on a glass substrate [93].

### Electrospinning

Inspired by the intriguing hierarchical structures formed on the lotus leaf, electrospinning is a highly versatile technique that allows the continuous fabrication of synthetic and natural polymers, nanoparticles, metals, and ceramics in nano and microscale. Electrospinning has been shown to possess several advantages for the fabrication of polymers or composite nanofibrous mats with high specific surface area and high surface roughness [94].

Lee et al. (2013) [95] prepared superhydrophobic membranes by deposition of polystyrene (PS) nanofibers onto a stainless steel mesh via electrospinning. These membranes absorbed oil selectively, being efficient for oil-water separation.

Dong et al. (2015) [96] fabricated nanofiber membranes of poly(vinyl alcohol) (PVA), followed by chemical cross-linking with glutaraldehyde and surface modification via low surface energy fluoroalkylsilane (FAS). The resultant nanofiber membranes exhibited self-cleaning properties as well as superhydrophobicity.

Liu et al. (2016) [97] have recently fabricated superhydrophobic electrospun poly(vinylidene fluoride) (PVDF) membranes with controllable structure and tunable wettability through incorporating ZnO nanoparticles.

### **Chemical Vapor Deposition**

The chemical vapor deposition (CVD) process is used to produce high purity and high performance solid materials. Generally, this process is used in the semiconductor industry for developing thin films. In a typical CVD process, a substrate will be exposed to a volatile precursor, which reacts and decomposes on the substrate surface for producing desired materials. In this process, various materials are used, including silicon, carbon nanofibers, filaments, carbon nanotubes,  $SiO_2$ , and titanium nitride.

Bao et al (2014) [98] prepared superhydrophobic surfaces by deposition of ZnO on various substrates, followed by a treatment with PDMS deposited by CVD. Thanks to this treatment, the wettability of various metal oxide nanoparticles-coated substrates including glass slide, print paper, fabric and sponge, changes from hydrophilicity to superhydrophobicity.

Liu et al (2016) [99] created superhydrophobic PDMS coated glass surfaces fabricated through CVD, obtaining contact angles of  $170^\circ$ .

### **3.1.3 Nanoimprint-based methods**

Nanoimprint Lithography (NIL) is one of the non-conventional lithographic techniques that allow the fabrication of superhydrophobic surfaces where the shapes of features are well defined. NIL has several advantages over other lithographic techniques, such as its high-throughput, high-resolution, low-cost and its ability to produce three-dimensional structures in a one-step process if the proper mold is fabricated.

Huovinen et al. (2012) [67] fabricated a hierarchical structures based on

micro structures by injection molding on polypropylene (PP). Hierarchically micro structured polymer surfaces exhibited the same superhydrophobic wetting properties as the hierarchically micro nano structured surfaces (Figure 3.5a). Micro micro structures had superior mechanical robustness in wear tests as compared to the micro nano structured surfaces.

Choi et al. (2013) [100] fabricated superhydrophobic and oleophobic surfaces with an overhanging structure by reverse nanoimprint lithography and reactive ion etching (Figure 3.5b). In order to lower the surface energy of the substrates, a fluoroalkylsilane-based self-assembled monolayer (SAM) was coated on the substrates by using a liquid-phase SAM coating technique. After the treatment, the surfaces exhibited repellency towards water, diiodomethane and hexadecane.

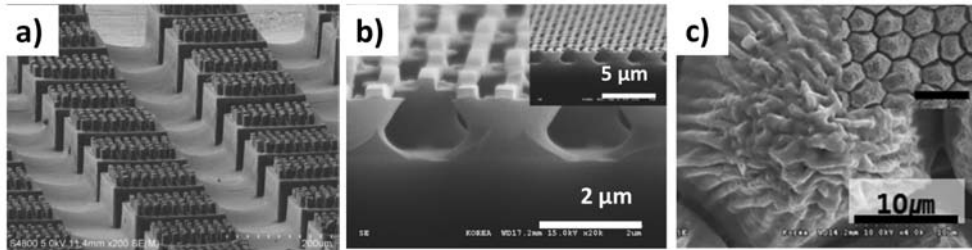


**Figure 3.5:** SEM images of a) hierarchical micro structures on a PP surface [67], b) nanopattern over the overhanging structures [100] and c) UV imprinted PFPE surface [101].

Ryu et al. (2014) [101] replicated the hierarchical structures of rose petal by using a nickel electroforming process. With this Ni shim, the hierarchical structure of rose petals was imprinted in perfluoropolyether (PFPE) (Figure 3.5c), which exhibited the petal effect, characterized by high water contact angle and high adhesion.

Choi et al. (2013) [102] fabricated hierarchical micro nanostructures by a combination of sol-gel based nanoimprint lithography and hydrothermal growth to tune the surface morphology. Microstructures were fabricated on  $TiO_2$  by the sol-gel nanoimprint lithography method. After the imprint, the  $TiO_2$  gel microstructures became a  $TiO_2$  microstructure by annealing. Then,  $TiO_2$  nanostructures were fabricated by hydrothermal growth (Figure 3.6a). These structures had contact angles over  $160^\circ$  for water.

Sung et al. (2015) [103] fabricated hierarchical structures using UV-nanoimprint

lithography (UV-NIL) and thermal shrinkage films (TSFs). Firstly, they fabricated nanoscale pillar patterns on the TSFs by UV-NIL, then, the TSFs were shrunk (Figure 3.6b). The nano and microscale complex-patterned TSFs were then coated with a self-assembled monolayer to reduce the surface energy of the structures. These structures exhibited superhydrophobic and oleophobic behavior.

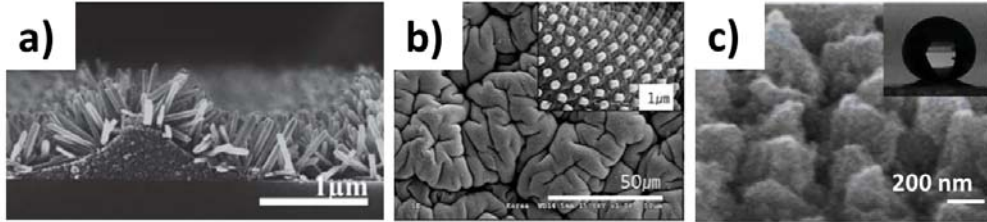


**Figure 3.6:** SEM images of a) hierarchical  $TiO_2$  structures [102], b) nanopatterned and shrunken thermal shrinkage film (TSF) [103] and c) nanopillars treated with  $C_4F_8$  plasma [104].

Liang et al. (2015) [104] produced flexible polycarbonate (PC) films by nanoimprint using a perfluoropolyether (PFPE) mold. After treating the PC nanopillar arrays with  $C_4F_8$  plasma, hierarchical structures with superhydrophobic behavior were obtained (Figure 3.6c).

### 3.1.4 Summary

In summary, superhydrophobic surfaces can be fabricated with a wide range of techniques over different materials. The created roughness can be either well defined or randomly distributed. Some of the techniques have the limitations of the available materials for their fabrication. Some materials require a post surface treatment in order to lower the surface energy. Most of the techniques are limited to one level structures, since usually hierarchical structures need a combination of different methods to be produced. Summary of all the formerly mentioned techniques are depicted in Table 3.1.

In this study, we have depicted NIL as a technique that present several advantages over the other techniques, such as:

- Nanoimprint Lithography can be used over low surface energy materials, such as common polymer materials (Polypropylene (PP) or polydimethylsiloxane

(PDMS)).

- Nanoimprint lithography is a flexible technique that allow the patterning over flexible or transparent materials.
- Well defined hierarchical surfaces can be fabricated in one-step imprint when selecting the proper mold.

Technique	Common Materials	Comments	Reference
Lithography	Silicon, $SiO_2$	Used to produce well defined structures	Li et al. (2010) [77] Park et al. (2012) [78] Wang et al.(2015) [79]
Etching	Polymers, Metals	Commonly used in combination with other techniques.	Yong et al. (2014) [86] Ta et al. (2015) [87] Ellinas et al. (2014) [88]
Anodic Oxidation	Metals	Porous metallic films	Wu et al. (2015) [90] Ganne et al. (2016) [91]
Hydrothermal Reaction	Monocrystalline solid	Random distribution	Gong et al. (2014) [92] Wang et al. (2014) [93]
Electrospinning	Polymeric fibers	Random distribution of fibers	Dong et al (2015) [96] Liu et al (2016) [97]
Chemical Vapour Deposition	Carbon based materials, Silicon, $SiO_2$	High purity materials	Liu et al (2016) [99]
Nanoimprint Lithography	Polymers, Resists	Possibility of produce direct 3D surfaces	Ryu et al (2014) [101] Sung et al (2015) [103] Liang et al (2015) [104]

**Table 3.1:** Typical techniques and corresponding materials to produce micro nanoroughness for superhydrophobic purposes.



## 3.2 Oleophobic Surfaces

The appropriate surface roughness and surface chemistry are both crucial factors to the fabrication of oleophobic surfaces. Moreover, the demands are stricter than for superhydrophobic surfaces.

Suitable low surface energy materials, like fluorinated compounds and thiols, are important to superoleophobic surfaces.

For surface roughness, a simple micro/nano dual scale structure is not enough. A new idea of re-entrant geometry structures, such as the T-shape [105], overhanging [106] and mushroom-like [107] is needed into the construction of superoleophobic surfaces.

### 3.2.1 Origin of Oleophobicity

Tuteja et al. (2007) [71] were the pioneers on analyse re-entrant structures for superoleophobicity. They fabricated a regular re-entrant structure on SiO<sub>2</sub>-silicon wafer (Figure 3.7a). The superoleophobic surface with hoodoo's structure was obtained by etching the silicon dioxide layer followed by chemical treatment with 1H,1H,2H,2H-perfluorodecyltrichlorosilane, by which the fabricated surfaces showed high contact angles and low sliding angles against various low surface tension liquids.

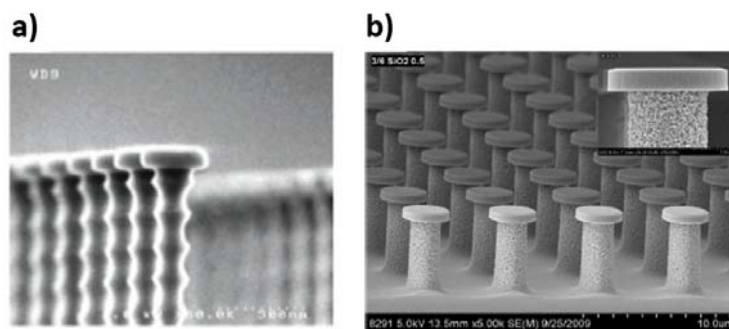


**Figure 3.7:** SEM images of a) re-entrant structures fabricated by Tuteja et al. [71] and c) re-entrant structures fabricated by Zhao et al. [108].

Zhao et al. (2011) [108] utilized photolithography followed by surface treatment of fluoropolymer monolayer to obtain superoleophobic surfaces and further investigated

their different wetting properties through changing diameter, height, and side shape of the pillars. After comparing different pillar dimensions and shapes, Zhao et al. concluded that the pillar geometry that is represented by the re-entrant structure along with the surface chemistry are major contributors for superoleophobicity (Figure 3.7b).

Despite the fact that tremendous efforts are dedicated to fabricate surfaces that have high repellency toward different types of liquids especially those with low surface tensions, nothing truly has been proven yet as a rigorous solution to address the fabrication of superoleophobic surfaces using manufacturing-intend techniques.

The fabrication methods currently used can be also divided into two basic approaches: the top-down and the bottom-up techniques.

### 3.2.2 Top-down Techniques

#### Etching

Using Al as the substrate, Ji et al. (2013) [109] prepared lotus-like hierarchical structures with HCl containing isopropyl alcohol (IPA). After surface fluorination they obtained repellency towards water and hexadecane.

Copper substrates are also used to fabricate superoleophobic surfaces by etching. Ou et al. (2013) [110] prepared the micro/nano hierarchical structure of superoleophobic surfaces on copper substrates. They successively immersed the pre-treated copper substrates in an aqueous solution of  $HNO_3$  and cetyltrimethyl ammonium bromide.

Random and ordered hierarchical micro nano structures were obtained by Ellinas et al. (2014) [88] using plasma texturing on polymeric surfaces.

#### Lithography

By the combination of ultraviolet nanoimprint lithography (UV-NIL) and hydrothermal synthesis, Jo et al. (2014) [111] fabricated superamphiphobic surfaces based on ZnO nano/micro hierarchical structures. They firstly prepared a ZnO nanoparticle dispersion resin and then patterned a circular cone shaped micro pattern with the as-prepared resin by UV-NIL. Subsequently, ZnO nanorods were grown on

the surface of the micro pattern by low temperature hydrothermal synthesis (Figure 3.8a). The values of CA for diiodomethane on the obtained surfaces were more than  $155^{\circ}$  with a low contact angle hysteresis (CAH).

Other structures were also obtained via similar methods. Lee et al. (2013) [106] designed a superamphiphobic surface with nanoscale re-entrant curvature via transfer molding and isotropic etching (Figure 3.8b).

Choi et al. (2013) [100] prepared superamphiphobic surfaces with overhanging structures via reverse nanoimprint lithography (Figure 3.8c). The CAs on the simple overhanging surface for water and diiodomethane are  $164^{\circ}$  and  $151^{\circ}$ , respectively.

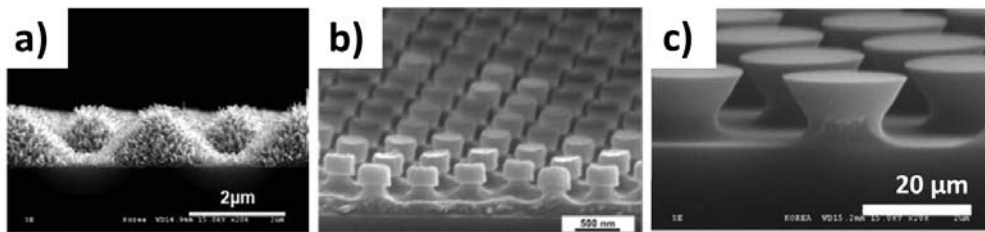


**Figure 3.8:** SEM images of a) nanoin-micro hierarchical structure, b) nanoscale re-entrant curvature and c) simple overhanging structure.

### 3.2.3 Bottom-up Techniques

#### Hydrothermal method

The hydrothermal method is another useful technique to create roughness. The products are of high purity and uniformly dispersed. The principle of the hydrothermal method is to dissolve substances making use of high temperature and high pressure.

Wang et al. (2014) [112] prepared an underwater superoleophobic coating based on hierarchical rutile  $\text{TiO}_2$  flowers through a simple one-step hydrothermal method. These obtained coatings showed superamphiphilicity in air and superoleophobicity in water with an oil CA of  $155^{\circ}$ .

### **Electrospinning**

Electrospinning is an inexpensive, simple, scalable and universal method to produce nonwoven micro and nanofibers with a high specific surface area and porosity.

Kota et al. (2012) [113] developed a simple one-step technique based on electrospinning microbeads onto textured surfaces to fabricate superoleophobic surfaces with re-entrant structures. The prepared superoleophobic surfaces exhibited ultralow contact angle hysteresis (CAH) even for extremely low surface tension liquids.

Ganesh et al. (2013) [114] prepared robust superamphiphobic self-cleaning coatings on glass substrates. The rice-shaped TiO<sub>2</sub> nanostructures were prepared by electrospinning and subsequently silanization. The water CA and oil CA (ethylene glycol) were 166° and 152°, respectively. The CAH for the droplet water and hexadecane were 2° and 12°, respectively. In addition, the coatings showed excellent mechanical and thermal stability with high adherence to glass substrates.

## Chapter 4

# Nanopatterning Techniques

The number of techniques that to produce superhydrophobic surfaces has increased during the last years, since nanotechnology has made possible both bottom-up and top-down approaches to fabricate nanostructured surfaces. Researches have devoted much effort in developing superhydrophobic surfaces on a wide range of materials and structures.

In order to apply the learned knowledge from nature to real life applications, efficient and low cost methods are needed to produce superhydrophobic surfaces. Furthermore, as it was already mentioned, even if the coating-based methods yield very good results in the laboratory scale production, the application to real life products present important drawbacks, such as toxicity or limited life time. For this reason, it is logic to think that the best approach to obtain superhydrophobic surfaces for real applications rely on the adequate roughening of low surface energy materials. Moreover, there are several plastic materials in the industry that exhibit a low surface energy.

Nanoimprint lithography (NIL) based methods are a good alternative, due to its high-throughput, high-resolution and low-cost. Furthermore, NIL-based methods can be used to pattern a wide range of materials and over a wide range of different substrates, allowing surface structuring of transparent and flexible materials [16].

It has been a subject of an active research and development since it was introduced by Prof. Stephen Chou in 1995 [115]. The technique is based on the replication idea: first, a substrate is coated with an imprint resist. Then, a high-resolution pattern on

a stamp surface is pressed into the resist film applying mechanical force. The resist layer is cured under pressure with the help of thermal or UV curing. It has been shown that imprint lithography resolution can reach below 5 nm [116]. Different NIL-based techniques have been developed since 1995, however, its fundamental principle is the same [117].

## 4.1 Nanoimprint Lithography

There are several nanoimprint lithography techniques, but most of them are variations of the two main techniques: thermal nanoimprint lithography and ultraviolet light assisted nanoimprint lithography (UV-NIL). An overview of this techniques will be presented in this section.

### 4.1.1 Thermal and UV-assisted NIL

Thermal NIL was developed in 1995 [115] while UV-assisted NIL was developed in 1996 [118], both processes are illustrated in Figure 4.1.

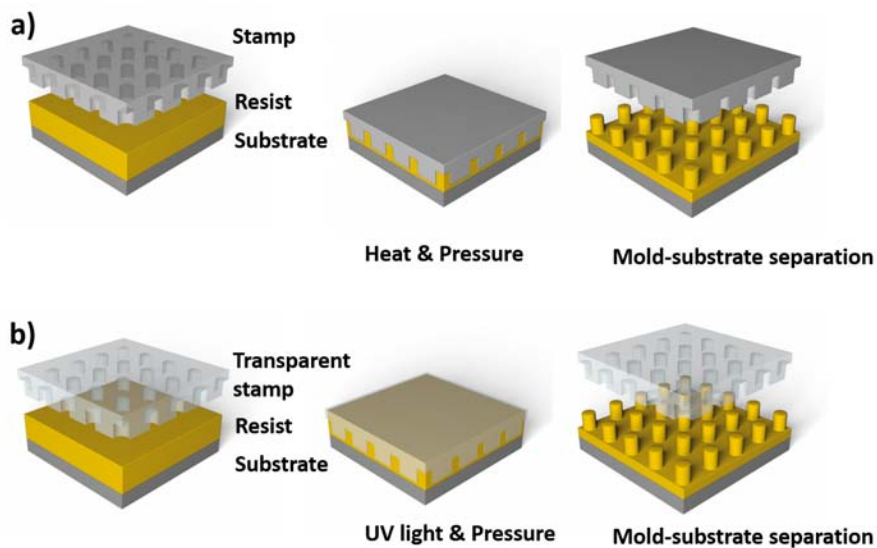


**Figure 4.1:** a) Schematic of thermal nanoimprint lithography. b) Schematic of UV nanoimprint lithography.

During thermal nanoimprint, a rigid mold is pressed into a thin thermoplastic polymer film, generally deposited by spin-coating, and heated above its glass

transition temperature ( $T_g$ ), above which the polymer can flow under certain pressure. After a certain time, the system is cooled down, and the mold and the substrate are separated [117].

On the other hand, in UV nanoimprint a photocurable resist is pressed at room temperature with a transparent mold under a fixed pressure and later polymerized by UV radiation. After some seconds, the stamp is separated from the patterned layer on the substrate.

After pattern formation, the polymer layer can be used as a resist mask for additional processing steps (transfer etching in the substrate, lift-off, etc.), or the imprinted layer can be used as a functional material.

In thermal NIL, a thermoplastic material is used as the imprint resist. When the material is heated above its glass transition temperature ( $T_g$ ), it becomes a viscous liquid and can flow. The Young's modulus and viscosity decrease by several orders of magnitude compared to their values at room temperature. Due to the decrease on the viscosity, it is easier to fill in the cavities of the stamp.

To fully fill the cavities of the stamp, the pressure needed can reach up to 50–70 bar, which means that the stamp material needs to have high mechanical strength, such as Si, SiO<sub>2</sub>, diamond-like coatings or metals. High thermal stability, low thermal expansion coefficients and low roughness are required for hot embossing stamp material.

In contrary, the viscosity of the UV-NIL resist is much smaller, thus UV-NIL has the advantages of room temperature operation and lower applied pressure (below 10 bar). Stamps for the UV-NIL process use to be transparent, such as quartz or PDMS, however, other stamps can be used if the UV light is applied through a transparent substrate.

#### 4.1.2 Reverse NIL

The thermal and UV assisted NIL techniques refer to a process working with a resist which is deposited on a substrate. In 2002 Huang et al. [119] proposed a modified version of the thermal nanoimprint process, where the resist was deposited onto the stamp and then was transferred to the substrate. This is called reverse

nanoimprint lithography. RNIL can be carried out either using thermal [119] or photocurable [120] resists. The key factor for a successful reverse nanoimprint lithography process is to make sure that the surface energy of the substrate is greater than that of the stamp, so the transferred polymer can be easily separates from the stamp but firmly adhere to the substrate. The main advantage of this process is that one can pattern over non-planar or difficult to spin coat substrates. The RNIL process has open the path for multilayer stacking and the creation of 3D structures [121–123], as will be discussed in the following Section.

Depending on the imprint conditions of the RNIL process, at least two different modes are possible depending on whether the pattern transfer is either complete or partial. The main differences between these two modes are:

- *Whole layer transfer*: If the imprint takes place at high temperatures ( $T > T_g$ ), the polymer flows. Under such conditions, the action of reversal imprinting technique is very similar to that of conventional NIL, and the whole polymer layer is transferred to the substrate (Figure 4.2a).
- *Inking mode*: On the other hand, if the reversal imprinting technique is carried out at a temperature around or even slightly below the  $T_g$ , the behavior of the reversal imprint technique is different, and only the polymer on the elevated parts of the protrusions is transferred to the substrate (Figure 4.2b).



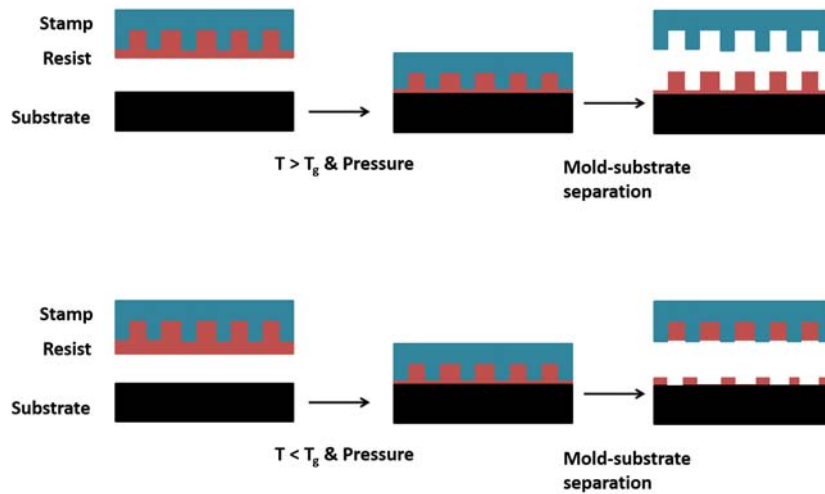


**Figure 4.2:** Schematic of the reverse nanoimprint lithography process at a temperature a) higher than  $T_g$  and b) lower than  $T_g$ .

### 4.1.3 3D NIL

There is significant progress in building 3D polymer structures by NIL. Compared with other 3D fabrication techniques, nanoimprint enjoys advantages such as simple equipment and high throughput. This section mainly addresses the fabrication of 3D polymer micro and nanostructures by nanoimprint. It includes a survey of 3D printing techniques reported in literature. The applications of hierarchical 3D structures in biomimetic surfaces gives a clear advantage over the 2D structures. In this regards, NIL is one of the most promising techniques to fabricate this kind of structures.

#### Direct Patterning of 3D Structures in One Step

Since nanoimprint is a physical replication process, it is easy to create 3D structures in a polymer layer if the template contains a 3D micro or nanostructure topography. The replication process could be identical to a conventional thermal or UV nanoimprint process if the proper mold is selected. The key factor in one-step fabrication of 3D nanostructures through nanoimprint is the fabrication of the 3D stamp.

In general, multiple steps of electron beam lithography or photolithography followed by reactive-ion etching (RIE) are used in 3D template fabrication. It is important to highlight that these multiple processes need to be done only once during the fabrication of the template. However, the conventional techniques for fabricating these stamps are not applicable for high-volume and large-area manufacturing.

During this thesis, we demonstrate the possibility of creating 3D stamps in a simple way by combining NIL techniques and electroplating. An example of a 3D nickel mold fabricated in this thesis is depicted in Figure 4.3.

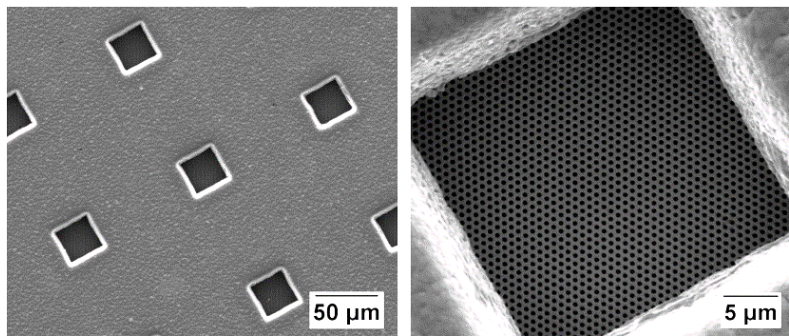


**Figure 4.3:** SEM images of a 3D nickel mold fabricated by NIL and electroplating techniques.

### Transfer Bonding and Sequential Layer Stacking

The reverse nanoimprint technique discussed above has been extended to transfer bonding of a polymer layer onto an existing polymer layer to form 3D structures (Figure 4.4). A standard nanoimprint step is used to pattern the first polymer layer (Figure 4.4a). To prepare for reversal nanoimprint, the polymer layer after a second nanoimprint will be transferred onto the stamp surface (Figure 4.4b). This layer will be transfer bonded to the first polymer layer formed in Figure 4.4a by reversal nanoimprint to form a two-layered polymer structure. The whole process can be repeated many times to form multilayer complex 3D polymer structures.

Compared to other 3D polymer structure patterning techniques based on serial writing or tedious layer-by-layer fabrication using multiple lithography and etching steps, the whole processing is simple and has good process throughput.

The first 3D structure by reverse nanoimprint was achieved by transfer polymer layers on mold to the surface of a pre-patterned substrate by Bao et al. (2002) [124].

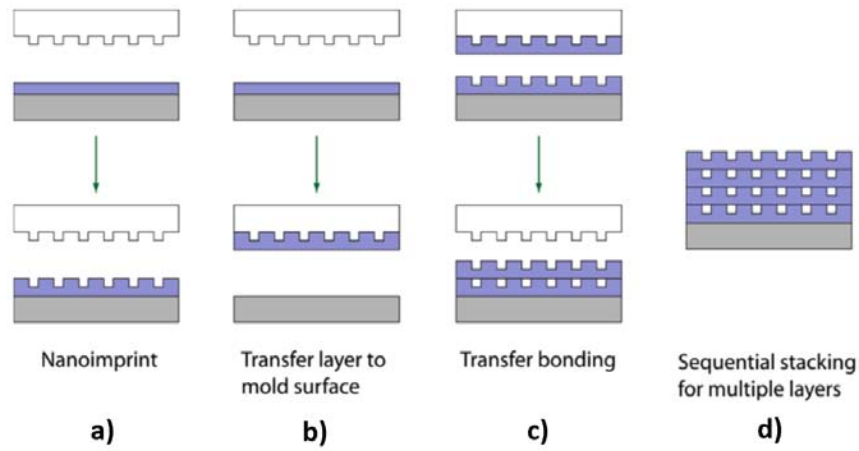


**Figure 4.4:** Schematics of building 3D micro and nanostructures by transfer bonding and sequential layer stacking.

Depending on the mechanical properties of the polymer materials and the pattern density in the substrate, two polymer transfer modes occurred (Figure 4.5).

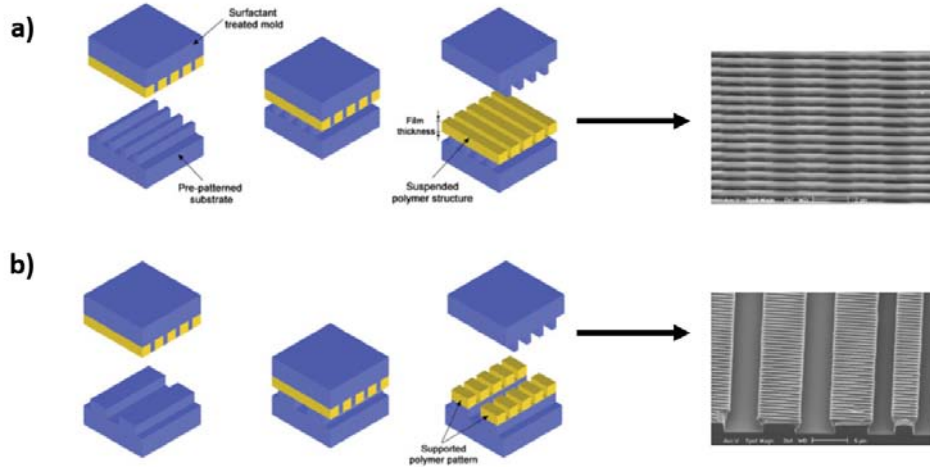


**Figure 4.5:** Schematics of nanoimprint over topography with two different results: a) whole layer transfer ( $700\text{ nm}$  period PMMA grating transferred onto substrate line patterns with spacing of less than  $2\ \mu\text{m}$ ) and b) layer transfer only on protruded surfaces ( $700\text{ nm}$  period PMMA grating transferred onto substrate line patterns with spacing of  $5\ \mu\text{m}$ ) [124].

If the substrate pattern density is very high, the polymer layer will be transferred as a whole (Figure 4.5a). If the substrate line spacing is too large, only resist on

line protrusions is transferred due to the weak mechanical strength of the polymer layer. Both transfer modes are useful to create different 3D structures for specific applications. The substrate pattern size and density and the polymer mechanical properties need to be taken into account when designing the 3D structures.

These experiments were performed using a hard silicon stamp, which limits the pattern transfer to the elevated parts of the previously patterned structure. However, if soft stamps could be used, the pattern transfer could take place both in the elevated parts and at the bottom of the structure, thus increasing the possibilities and the flexibility of the method. During this thesis, we demonstrate how using a soft PDMS stamps can produce several configurations of 3D structures.

### 3D Nanostructures by Two Consecutive Nanoimprints

Ordered 3D hierarchical structures can also be obtained by two or more consecutive nanoimprint steps without using 3D templates. This technique was firstly developed by Zhang et al. (2006) [125]. The schematic fabrication process is depicted in Figure 4.6.

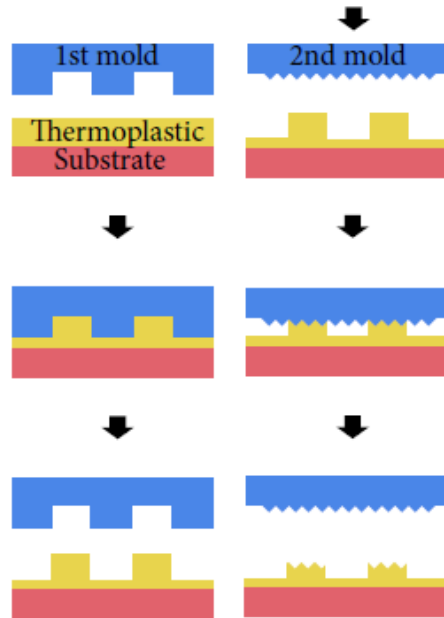


**Figure 4.6:** Schematic diagram for hierarchical surface by two consecutive nanoimprints.

The first nanoimprint is done at a temperature above the  $T_g$  of the polymer to

be patterned. The second nanoimprint is performed on the previously patterned structure at a temperature below polymer  $T_g$ . In this case, the secondary patterns on top of the protrusions of the previously patterned structures were formed by purely mechanical forming under high pressure instead of melt flow. In the same manner, a tertiary or higher order pattern can also be created above the secondary pattern.

### **Comparison of 3D printing approaches**

Although one-step replication of 3D structures by nanoimprint is very attractive, this approach is limited to 3D structures that are easy to demold after nanoimprint. There are many useful 3D structures, such as 3D photonic crystals and 3D microfluidic devices, which cannot be achieved by direct NIL alone. To fabricate such 3D multi-layer structures one need to utilize a sequential transfer techniques such as reversal nanoimprint or transfer bonding.

An important advantage of these processes is that the material and the structure in each layer can be varied. This provides great flexibility in designing the 3D multi-layer structures to suit targeted applications. A summary of the advantages and drawbacks of the presented methods to fabricate 3D structures is given in Table 4.1.

Technique	Advantages	Drawbacks
<i>Direct Patterning</i>	<ul style="list-style-type: none"> <li>• The replication of the 3D structure is accomplished in a single step.</li> <li>• Better uniformity.</li> </ul>	<ul style="list-style-type: none"> <li>• Limited to 3D structures that are friendly to the demolding process.</li> <li>• Expensive.</li> </ul>
<i>Transfer Bonding &amp; Sequential Layer Stacking</i>	<ul style="list-style-type: none"> <li>• Material and structure in each layer can be varied.</li> <li>• Simple and high throughput.</li> </ul>	<ul style="list-style-type: none"> <li>• Pattern alignment for multi-level structures is difficult.</li> </ul>
<i>Two Consecutive Nanoimprints</i>	<ul style="list-style-type: none"> <li>• No need of complex fabrication processes for the stamp fabrication.</li> </ul>	<ul style="list-style-type: none"> <li>• Very high pressures needed.</li> <li>• Only suitable for thermoplastic polymers.</li> </ul>

**Table 4.1:** Nanoimprint-based techniques to produce 3D structures with their corresponding advantages and drawbacks.

## 4.2 Electroplating

The stamp material and geometrical parameters in the NIL process directly affect the template deformation and therefore the quality of pattern transfer. Moreover, the high cost of the master stamps still remain the main bottleneck of the process. Therefore, the production of high-quality, high-precision imprint template is a key issue.

In this regard, electroplating (electrodeposition) has become one of the most important technologies for producing stamps, as it produces high-quality metal films in a simple way and at a low cost. Various metal and alloy films such as Ni, Cu, Au and NiFe, NiP, CoFe have been formed by electroplating [126].

Electroplating can be considered a simple technique that has been used for many years for protective and decorative purposes. Nowadays, it is one of the

most cost-effective techniques used in a wide range of technological fields. Overall, electroplating is used in many industrial areas including home appliances, jewellery, automotive, aerospace and electronics.

During the last years, researchers are starting to use this technique as a way to create micro and nanoscale features for different purposes [127–131]. Nickel is a common material for electroplating, which has the benefit of high strength, hardness, and resistance to corrosion in comparison to silicon stamps.

Electroplating is a process of coating a working electrode with another material which is present in its ionized form in the electrolyte. Thermodynamically, it is not possible to achieve movement of charges in presence of solitary electrode-electrolyte. Therefore, electroplating processes are always conducted in electrochemical cells. An electrochemical cell is a device capable of either deriving electrical energy from chemical reactions, or facilitating chemical reaction through the introduction of electrical energy. These electrolytic cells consist of two electrodes, the electrolyte and an external source of current, as depicted in Figure 4.7.

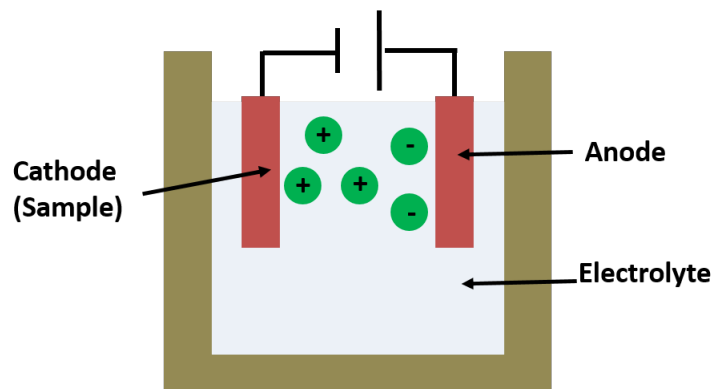


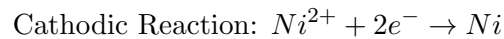
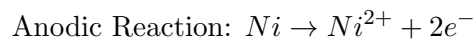
**Figure 4.7:** Schematics of the electroplating process.

The stamp to be plated is the cathode of the circuit. The anode is made of the metal to be plated on the stamp. Both parts are immersed in a solution called an electrolyte containing one or more dissolved metal salts as well as ions.

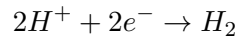
By applying an over-potential through an external power supply between the two electrodes, the flow of the current causes the anode, in this case metallic nickel, to dissolve in the solution as positively charged nickel ions. Subsequently, the nickel ions dissolved in the solution react with the electrons being supplied at the cathode

surface and are deposited as metallic nickel. The flow of current between the two electrodes enables the anode to dissolve and replenish nickel ions that are being depleted when being deposited at the cathode. The potential represents the energy available to drive charges between the electrodes and its magnitude controls the direction and the rate at which charges are transferred between the two interfaces.

The mechanism of electrical transfer in the solution is by means of electrically charged ‘particles’ called ions. Positive ions (cations) travel towards the negative electrode (cathode) and negative ions (anions) travel toward the positive electrode (anode) when the potential is applied, thus completing the electrical circuit. The chemical reactions which take place are described here:



In electroplating from aqueous solutions, hydrogen evolution may consume part of the current density input as a secondary reaction, reducing the current efficiency:



The resulting  $H_2$  bubbles may be incorporated into the deposit, causing defects in the deposition process. To avoid this, either a recirculation system or a moving cathode are necessary to produce uniform depositions.

Faraday Laws of electrolysis (1833) are basic to electroplating. They relate the current flow, time and the equivalent weight of the metal with the weight of the deposit and can be summarized as follows [126]:

- The mass of the substance produced by electrolysis is proportional to the quantity of electricity passing through the electrode.
- The amount of electricity in coulombs required to produce 1 mole of a substance is a multiple of a constance  $F = 96485 \text{ C/mol}$ .

The Faraday Laws are mathematically expressed as:



$$m = \frac{MI t}{zF} \quad (4.1)$$

where  $m$  is the mass of the substance liberated at an electrode in grams,  $I$  is the current that flows through the plating tank in amperes,  $t$  the time,  $z$  is the valency number of ions of the substance (the number of electrons required to plate each ion) (2 in the case of the  $Ni$ ),  $F$  is the Faraday constant ( $96485C/mol$ ) and  $M$  is the atomic weight of nickel (58.69).

The density of the deposited Nickel is a known parameter, and is given by:

$$\rho = \frac{m}{V} = \frac{m}{d \cdot A} \quad (4.2)$$

where  $\rho$  is the density of the  $Ni$  ( $8.908 g/cm^3$ ),  $d$  is the thickness of the deposited  $Ni$  and  $A$  is the area of the deposited  $Ni$ . Thus, the deposition rate can be calculated as follows:

$$\frac{d}{t} = \frac{MI}{zF\rho A} \quad (4.3)$$

where the ratio  $I/A$  is the current density and thus the above expression shows that the coating thickness depends on the current density and time.

Faraday Law assumes a current efficiency of 100%, which means that the hydrogen evolution and other secondary reactions are not taken into account. Thus, it constitutes an approximation to determine the weight of deposited mass.

#### 4.2.1 Template-assisted electroplating

Template-assisted electroplating (up-plating) methods [132] allow synthesizing micro and nanostructure with controlled shape and size. They involve the use of restrictive templates as a cathode in the electrochemical cell. The template can be removed after the electroplating process. The experimental set-up of electroplating using restrictive templates is schematically shown in Figure 4.8.

The template is made of a non-conductive material, thus acting as a mask that avoids the deposition of the metal on the non-conductive areas. This produces the metal to be deposited only in the opened areas of the template, producing controlled

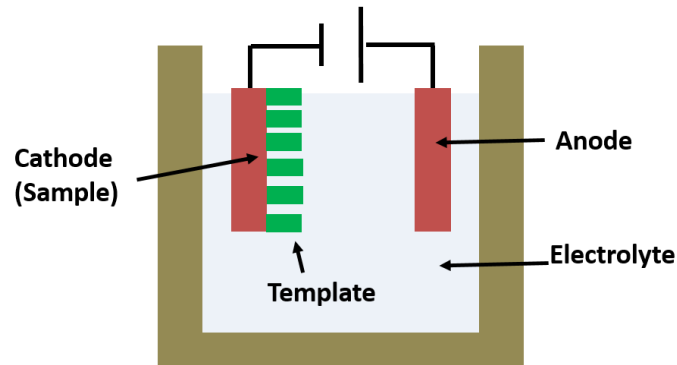


**Figure 4.8:** Schematics of the cathode arrangement for the production of micro and nanostructures by means of electroplating.

micro and nanostructures. This method has been used to produce large aspect ratio metallic nanowires [132–134] with diameters ranging from hundreds of micrometers down to tenths of nanometers, depending of the template and the desired application.

Several structures have been created by this method on a wide range of different electroplated metals. Liu et al. (2013) [135] fabricated ordered macroporous zinc films by using polystyrene (PS) spheres as templates. Hnida et al. (2013) [136] produced indium–antimonide (InSb) nanowires by using anodic aluminum oxide (AAO) templates with the pore diameter of 100 nm. InSb is a III–V compound semiconductor that in a form of nanowires can possess improved thermoelectrical and optical properties compared to the corresponding bulk crystal. Burek et al. (2010) [134] created gold and copper nanopillars on patterned polymethylmethacrylate (PMMA) by electron beam lithography. Electrodeposited nanostructures can be used in different fields, such as MEMS/NEMS, thermoelectricity, batteries and solar cells, among others.

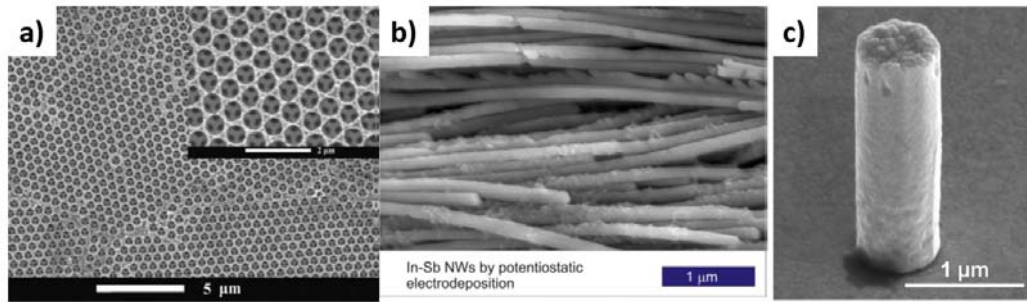


**Figure 4.9:** SEM images of different electroplated structures: a) zinc macroporous film, b) indium-antimony nanowire and c) gold nanopillars.

In this thesis we used the electroplating technique to produce masters with different morphologies that can be used either to prepare soft molds from them or as an insert for an injection molding tool. Both direct electroplating and up-plating approaches were followed, depending on the desired end use application. Further details on the produced micro and nanostructures by electroplating techniques will be given in the Chapter 6.

### 4.3 Injection Molding

Injection molding is recognized as a powerful mass-production tool in which uniform quality products can be realized over a wide range of sizes and with a high shape degree of freedom. Injection molding is a process technology that has been well established in the production of polymer parts in the macro-dimensional range for decades, since it is widely used to manufacture molded products from car bumpers (meter size) to cellular phone connectors (millimeter size).

Fields of application of micro and nano molded products are: optics (waveguides, micro lenses, fiber connectors), micro mechanics (micro gears, micro actuators, micro pumps, micro switches), information storage and data carrier devices (CDs, DVDs, sensor discs), micro fluidic systems (blood analysis, DNA analysis), medical technology (hearing aid, components for minimal invasive surgery). Among all the plastic-processing methods, injection molding accounts for 32% by weight of all the polymer material processed [137].

Microstructures are already injection molded on a big scale and with very low

cost by the industry on flat surfaces; such as everyday items like DVD and Blu Ray discs. In the laboratory, it is possible to injection mold up to 50 nm structures [138].

The complexity of the injection molding process comes from the design of the mold and process optimization. Once a mold insert has been made and the process has been optimized, several thousands parts can be molded automatically.

The basic principle of injection molding is simple, a melted polymer fills a predefined mold and the part is removed once the polymer has solidified. An injection molding machine transforms thermoplastic granules into usable parts, the process requires almost no supervision and is fully automated. In reality, the injection molding process is complex with multiple parameters involved.

In order to maintain their functionality, all the micro/nano features of a fabricated polymer part must have high accuracy and good reproducibility. Therefore interfacial effects, such as capillary forces, friction, and entrapped air strongly influence the good quality of the replicated micro/nano scale features.

The schematic drawing of the injection molding process is shown in Figure 4.10.

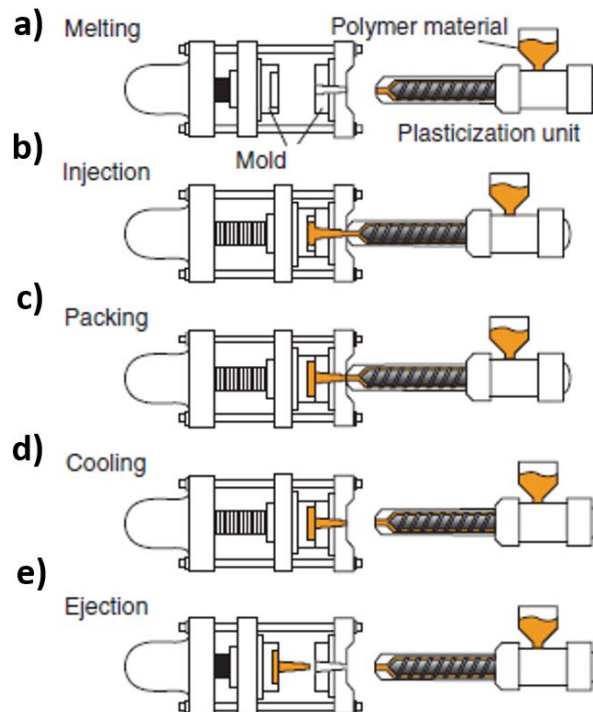


**Figure 4.10:** Schematic of the injection molding process [139].

First, a granular polymeric material is placed in the plasticizing unit of an injection molding machine. The screw rotating in the unit melts and mixes the material until a uniform molten polymer is obtained (Figure 4.10a). This is called the melting process, and it is an important process in which the physical properties of the molded product are determined. This temperature, of course, is higher than the glass transition temperature ( $T_g$ ) of the polymer; thus, the injected molten plastic mass does not harden prematurely.

Subsequently, the injection process that fills the mold cavity with the molten polymer is started (Figure 4.10b). In general, the metal mold for the injection molding is divided into two halves (a fixed half and a movable half). Molten polymer is injected into the space of the mold that is formed by closing these halves.

One of the most important phases inside the injection molding process is the filling phase. As the mold is filled, polymer is pushed into the mold cavity until the cavity is almost full. During this process, polymer in contact with the metal mold will solidify in a thin layer between the mold and the molten polymer. The freezing process is almost instantaneous and once the frozen layer is formed the polymer will be static and cannot flow. The frozen layer is a big issue when injection molding nano and microstructures, since the polymer will have to flow into the mold cavity before the frozen layer is formed. Once formed, the frozen layer will prevent further nano or microstructure filling. The mold temperature becomes an important parameter when optimizing the filling process, since the formation of the frozen layer will influence the surface quality of the part. A higher mold temperature will decrease the frozen layer thickness, but increase cycle time. Typically, in industrial fabrication a compromise between replication quality and fabrication speed is made. The frozen layer can be avoided if the mold is preheated to a higher temperature than the polymer melting temperature.

The packing phase (Figure 4.10c) starts after the cavity is almost full. During the packing phase, pressure is increased further forcing more polymer into the mold. Thereby shrinkage of the part will be uniform and reduced. When the polymer has filled the cavity, and packing begun, material will flow to regions of the part that are less densely packed, until a uniform packing is achieved. The packing flow will

be influenced by the compressibility and thermal expansion of the polymer melt. Over-packing of the mold can occur if a too high holding pressure is used, this will reduced shrinkage, and in some cases, after demolding, the parts can be larger than the mold cavity. Sometimes an over packed part can be impossible to demold. For this reason, the optimum pressure needs to be carefully determined in order to avoid the effect from low and high packing pressure.

Next is the cooling process (Figure 4.10d), which occupies a large portion of the cycle time of the injection molding process. The cooling period depends on the kind of polymer material and the size of the molded product. A series of injection molding processes ends by removing the molded product from the mold (Figure 4.10e).

### 4.3.1 Injection molding for functional plastic surfaces

Polymer surfaces are the most promising ones to produce superhydrophobic materials for real life applications, due to the avoidance of using chemical coatings. Most of the methods described in the literature are not compatible with conventional large scale fabrication methods, for this reason, injection molding arises as a promising method to produce large area superhydrophobic surfaces. Some studies have already been reported in this regard.

Hopmann et al. (2014) [140] fabricated superhydrophobic surfaces made from liquid silicone rubber by injection molding. Cold liquid silicone rubber is injected into a preheated mold, cured and ejected. The structures consist of conical pillars made from steel inserts fabricated by picosecond laser. After structuring the contact angle was increased over  $155^\circ$ .

Michaelli et al. (2011) [141] show a method to have a fast laser based variotherm injection molding process, with a heat up rate up to  $300K/s$ . A mold with superhydrophobic structures was tested with laser heating versus a traditional injection molding process. Results from the paper are clear and the variotherm process is required in order obtain the replication quality required for the superhydrophobic effect.

Huovinen et al. (2012) [67] fabricated a hierarchical structures based on

micro/micro structures by injection molding on polypropylene (PP). Hierarchically micro/micro structured polymer surfaces exhibited the same superhydrophobic wetting properties as the hierarchically micro/nano structured surfaces. Micro/micro structures had superior mechanical robustness in wear tests as compared to the micro/nano structured surfaces.

#### 4.4 Process flow

In this section we present a summary of the process chain followed throughout this thesis to produce functional plastic surfaces, including the design of the functional surface and the developed fabrication approaches, as shown in the schematic diagram from Figure 4.11.

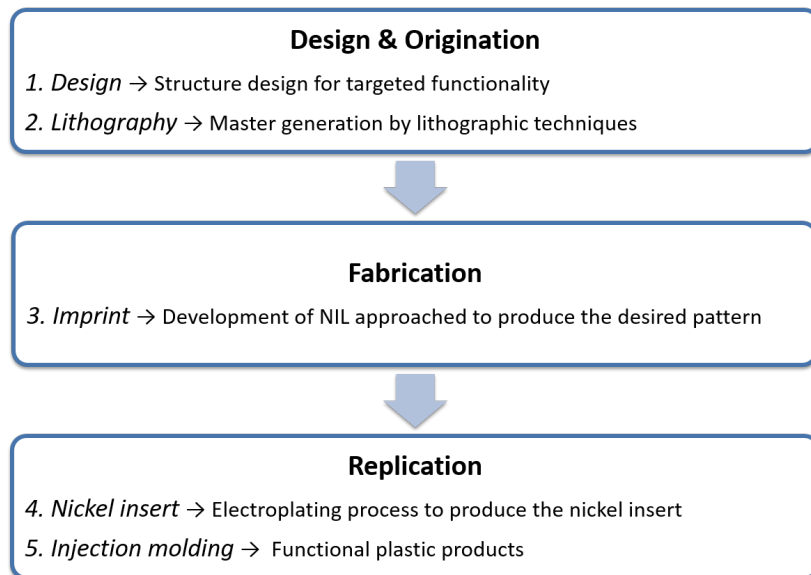


**Figure 4.11:** Schematic of the process chain followed in this thesis to produce functional plastic products.

We start with the design of the desired superhydrophobic surfaces, taking into account the theory developed in Chapter 2.

By means of conventional lithographic techniques we produce the needed masters to fabricate the desired hierarchical structures. Subsequently, by combining different NIL-based methods, the hierarchical surfaces are developed. These surfaces can be used as functional surfaces or to produce suitable molds for the injection molding

process.

Nickel electroplating was the selected technique to produce the nickel inserts for the injection molding tool; within this framework, two different approaches were used: 1) direct electroplating over the hierarchical surface and 2) template-assisted electroplating (up-plating) to directly produce a patterned surface.

Finally, these nickel inserts were mounted in the injection molding tool and used repeatedly to generate identical copies of the functional surfaces.



## Chapter 5

# Materials and Processes

In this thesis, a number of fabrication techniques, processes, structures and equipments were employed. In this chapter we present a review on all the fabrication processes used throughout this work, as well as the employed materials for every specific process. The main equipments used for the fabrication of the superhydrophobic structures over different substrates were a thermal and a UV-based NIL equipments. Industrial electroplating was used to produce stamps and nickel inserts for an injection molding tool. Injection molding was tested with our designed nickel inserts to produce functional plastic surfaces. Other techniques, such as photolithography, electron beam lithography or etching were used to define the masters, the starting point for the silicon masters fabrication.

Different characterization techniques were used to analyse the resultant surfaces, divided in imaging and surface wetting techniques. Optical and scanning electron microscopy were used to analyse the surface morphology of the fabricated samples. A contact angle system was used to measure the surface contact angle as a tool to estimate the wettability of the material surfaces. Apart from the contact angle values, further wetting experiments were performed, using stages with a tilt option and a high speed camera.

## 5.1 Materials

The material processing and properties of substrates, resists, and anti adhesive coating were investigated. Fabrication with nanoimprint-based processes opens the possibility to use a wide range of materials and substrates. Depending on the selected material, different approaches should be followed. Furthermore, mechanical and thermal stability, viscosity or glass transition temperature are some of key parameters that need to be addressed in order to have a competitive process. One of the advantages of NIL based methods is that high temperatures, pressures or beams are not employed. Therefore, the physical and chemical properties of the polymeric materials were not affected in our experiments. Although there are large variety of polymers suitable for NIL we have been using polymers synthesized by Micro Resist Technology *GmbH*.

### 5.1.1 Stamps & Molding materials

Many materials have been proposed to be used as stamps for NIL. The choice of the material is correlated to the NIL imprint techniques which is employed. Standard materials for NIL stamps are silicon, quartz, nickel and polymeric soft stamps for thermal, UV, roll-to-roll and soft lithography techniques, respectively. The most commonly used material is silicon. This material has many advantages over all other proposed materials, as it is available in moderate cost and size. It has good strength, it is not too fragile and has low thermal expansion coefficients. Furthermore, this material have been extensively studied, in consequence, many different structures can be fabricated over silicon. In this thesis, silicon was the selected materials to fabricate the masters, due to the possibility of fabricate a wide range of different structures. These masters or templates were subsequently replicated on polymeric soft stamps.

On the other hand, metals such as nickel have been successfully used as stamps in injection molding. High quality, high resolution, durable stamps can be fabricated by electroplating. In this work, we fabricated nickel stamps by electroplating and up-plating techniques, depending on the targeted application.

The need for inexpensive stamp copies has led several groups to try to develop polymer stamps for NIL applications. PDMS is one of the most used materials for use it as a stamp. It is flexible, transparent and has a low Young's modulus. Moreover, due to its low surface energy, there is no need to apply an antiadhesive layer to achieve a proper demolding process. PDMS stamps can be fabricated from a silicon stamp very simply, and they can be used up to multiple times.

PDMS normally includes two parts: part A is a base polymer containing polydimethylsiloxane bearing vinyl groups; part B is a curing agent containing a platinum-based catalyst that catalyzes the addition of the silicon hydride (Si-H) bonds across the vinyl groups forming  $Si - CH_2 - CH_2 - Si$  linkages. Controlling the mixing ratio of the two components (part A and part B), different mechanical properties of PDMS can be achieved. Young's modulus can be tuned by changing the mixing ratio from 1:10 to 1:5 (part A : part B): the smaller the ratio, the lower the resulting Young's modulus (the softer the nature) [142].

The PDMS stamps used during this thesis were fabricated by pouring the PDMS solution into the relief structure of the silicon master mold. Depending on the dimensions and aspect ratio of the structures to be replicated, we used different ratios of the PDMS precursor:curing agent. The curing time was set to 12 h at 60<sup>0</sup>C, while a de-gasing step was introduced to eliminate any bubbles which could have been trapped while stirring the PDMS mixture. We optimized the thickness of the PDMS molds to be 3 mm in order to avoid pattern deformation due to the stretching of the mold [143]. Once the PDMS was cured, we manually peeled it off from the silicon stamp.

### **Antiadhesion treatments**

One important parameter to achieve a reliable NIL imprint is to avoid adhesion between the polymer and the stamp. This difficulty is inherent to the high density of nanoscale protrusions patterned on the mold surface which effectively increases the total area that contacts the resist. Depending on the stamp material, different anti-adhesion surface have to be applied.

Fluorinated Antiadhesive Layers (F-ASLs) based on perfluoropolyether molecule

(Optool DSX from *Daikin Chemical*) were used to create an antiadhesive layer on the silicon molds, based on a previously reported method [144].

Prior to the ASL deposition, molds are cleaned using a ‘CARO’ solution (2:1 volume mixture of  $H_2SO_4$  and  $H_2O_2$ ) for 15 min. This solution removes organic compounds from the surface and promote the creation of -OH bonds. The used technique includes three steps illustrated in Figure 5.1.

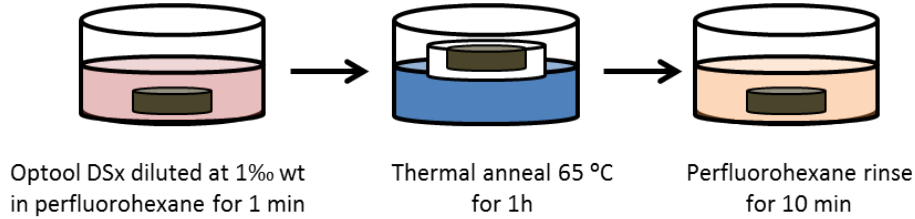


**Figure 5.1:** Schematic of the followed method for the deposition of a fluorinated antiadhesive layer on the mold surface.

The mold is first introduced in a low concentration Optool DSX solution (1‰ wt into perfluorohexane) during 1 minute. It is then placed in a water-saturated environment at 65°C for one hour before being rinsed in perfluorohexane during 10 minutes.

### 5.1.2 Patterning materials

In general, the choice of the polymers to be processed during NIL process depends on the targeted application. Properties such as high etching resistance, high mechanical stability, low glass transition temperature and functionality are few of the material properties which have to be carefully considered.

#### Thermal NIL

Two commercially available thermoplastic resist materials were processed by thermal NIL throughout this thesis.

PMMA is a positive resist based on special grades of polymethyl methacrylate designed to provide high contrast, high resolution for e-beam and NIL process. Different molecular weights (35000 – 75000) and different viscosities (3.2 – 9.3 mPa·s) were used in this thesis, depending on the imprint process and the structures to be fabricated. The glass transition temperature of the PMMA is  $T_g = 105^{\circ}C$ .

mr-NIL 6000E is a newly developed resist that exhibits photocurable and thermoplastic properties. This resist allows the thermal imprint at low temperatures, and can be subsequently cured by UV irradiation. The glass transition temperature of the mr-NIL 6000E is  $T_g = 1^{\circ}C$ .

### UV-NIL

Apart from thermoplastic resist materials, two commercially available different photocurable resist were used, namedOrmocomp and XNIL-26 SF. Both materials are solvent-free and exhibit low surface energy values. Ormocomp is a UV curable inorganic-organic hybrid polymer designed for UV imprinting or molding that after processing has glass-like properties. It exhibits excellent thermal stability at temperatures up to  $300^{\circ}C$ . It has an excellent mechanical and chemical stability (does not dissolve in organic solvents) once it is cured.

On the other hand, XNIL-26 SF has some intrinsic antiadhesive characteristics, due to its fluorinated compounds, that make it excellent for investigation on superhydrophobicity. Furthermore, it has a shorter curing time as compared to Ormocomp. XNIL-26 SF is purely organic, making it easy to remove once cured by applying a oxygen plasma. Ormocomp has a intrinsic contact angle of  $90^{\circ}$ , whereas mr-XNIL26 SF exhibits an intrinsic contact angle as high as  $105^{\circ}$ .

### Injection molding polymers

A wide range of polymers can be used for injection molding, since it is a well established technique for industrial applications. Depending on the targeted application, one could select the physical and chemical properties of the molded polymer. In this thesis, low surface energy polymers were required, since the targeted application was to generate superhydrophobicity functionalities to the produced plastic component without the need of any chemical post treatment. Two different polymers were selected for our experimental investigations. These were polypropylene (PP) and TOPAS. These polymers have a Young contact angle of  $91^{\circ}$  and  $90^{\circ}$  respectively, making them suitable candidates for superhydrophobic application.

## 5.2 Processes

During this thesis several fabrication approaches and equipments were used. The masters were fabricated by conventional lithography techniques, including photolithography, deep-UV lithography and electron beam lithography. The fabrication of the 3D hierarchical structures was performed by combining different NIL-based techniques. Electroplating and injection molding were used to up-scale the processes obtained on the laboratory to industrial processes. Nickel surfaces were fabricated by electroplating for its subsequent use as inserts on injection molding tools.

The characterization techniques used in this thesis can be divided on imaging techniques, to analyse the surface topography as well as the quality of the different replication processes, and surface characterization techniques, responsible of analyse the wetting behavior of the fabricated surfaces.

### 5.2.1 Pattern definition by conventional lithographic techniques

The masters with the microstructures were defined by conventional photolithography process, while the masters with the nanostructures were fabricated by electron beam lithography (EBL) or deep-UV lithography. Subsequently, the pattern is transferred onto the substrate using an etching process. The master with the nanospike structures was created by a dry etching process. The main masters were fabricated on silicon. Subsequently, soft replicas for develop the different fabrications approaches were fabricated.

#### Photolithography & Deep-UV lithography

Photolithography is a widely used lithography technique, only suitable for generating patterns with microstructures. The resolution of this technique is low, however, is a well known and relatively cheap process that can be used if the required structures are in the micro regime. For this reason, this technique was used to generate the masters with the microstructures.

On the other hand, deep-UV lithography uses UV light, which possess a lower

wavelength, allowing to produce patterns at higher resolution than the microscale. This technique is a high-cost technique, therefore, it was used when the resolution of the photolithography was not enough to produce the desired nanostructures. Section 7.1.3 gives a review of the structures that were fabricated with photolithography and deep-UV lithography.

Steps involved in the light-based lithography process are: wafer cleaning, photoresist application, exposure and development, as illustrated in Figure 5.2.

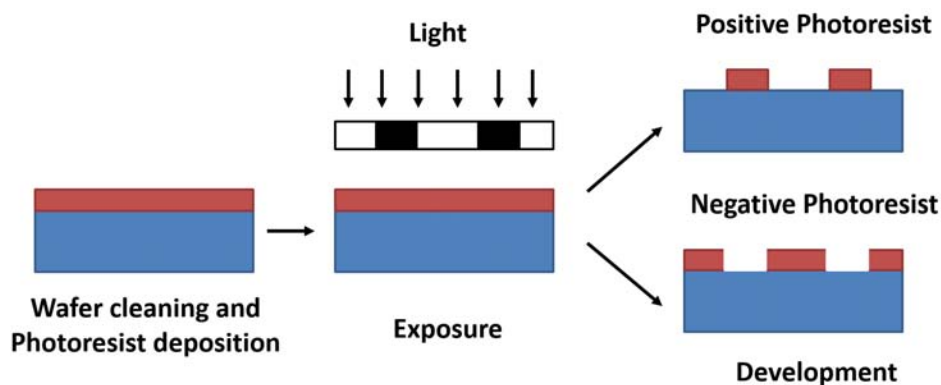


**Figure 5.2:** Schematic diagram showing the photolithography process using a negative and a positive resist.

In the first step, the wafer is cleaned to remove particulate matter on the surface as well as any traces of organic compounds and metallic impurities. After cleaning, photoresist is applied to the surface of the wafer by ‘spin coating’, a technique that ensures a thin uniform resist film. In function of the type of the resist two different processes can take place in this step:

- **Positive resists:** In these resists, exposure to the UV light changes the chemical structure of the resist so that it becomes more soluble and easier to remove. The exposed resist is then washed away, leaving windows of the bare underlying material. The mask, therefore, contains an exact copy of the pattern which is to remain on the wafer.
- **Negative resists:** Exposure to the UV light causes the negative resist to become polymerized, and more difficult to dissolve. Therefore, the negative

resist remains on the surface when it is exposed to light. Masks used for negative photoresists, therefore, contain the inverse of the pattern to be transferred.

The last step involves the removal of the residual resist with a chemical product called the ‘developer’. Generally, the developed resist can have two functions: final coating layer or template material. In the last case, the resist acts as a temporary template for one of several methods of image transfer, such as etching. The remaining resist is removed or stripped after the image transfer step.

### Electron Beam Lithography (EBL)

Electron beam lithography (EBL) is one of the most powerful methods for creating high resolution nanoscale structures. The main advantages of EBL over the conventional photolithography techniques include very high resolution, greater accuracy and the ability to write a variety of pattern geometries.

In EBL, a beam of electrons is utilized to generate patterns on a substrate surface. A high-vacuum environment allows electron travel without scattering by the air. The principle of this technique is to use a high voltage electrons in the range of 1 kV - 100 kV to nanopattern the electrosensitive resist deposited on the substrate by directly writing onto it. A very high resolution of several nanometers can be obtained with this method. The schematic process is shown in Figure 5.3.

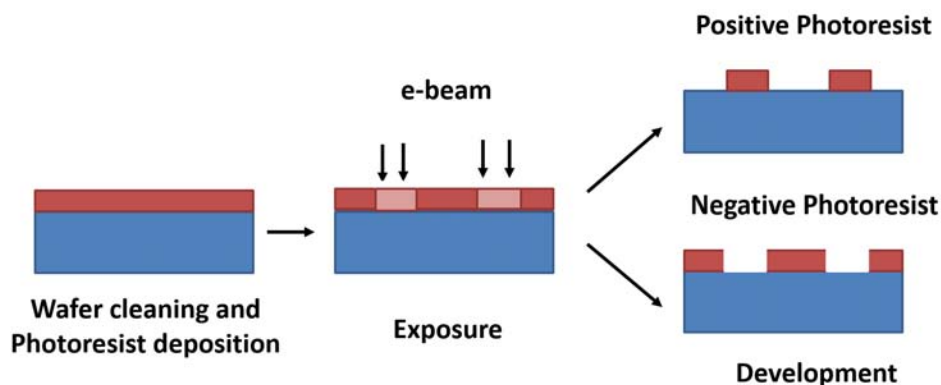


**Figure 5.3:** Schematic diagram showing the electron beam process using a negative and a positive resist.



The short wavelength associated with high-energy electron beam gives to EBL an ultra high resolution capability. However, the resolution limit is determined not by the beam size, but by the scattering effects occurring in the resist after interaction with the electrons of high energy.

The fundamental process is the same than in photolithography, but, since the exposure is carried out by an electron beam instead of a light source, the resolution is higher in this method. However, some drawbacks arise from this technique, mainly its slowness and its high cost.

### **Reactive Ion Etching**

Etching process can be used for a wide range of targeted objectives in function of the desired applications. It can be used to transfer a pattern to a master using a resist as a mask, to remove undesired resist (e.g. residual layer) on the surface or even to produce rough patterns. In function of the desired applications and materials to be etched, different chemicals or gases can be used.

Wet chemical etching with acid or base solutions is normally used to transfer a pattern onto semiconductor materials. It involves either the oxidation or reduction of the semiconductor surface followed by removal of the soluble reaction products. Wet etching is generally fast, with low damage and low cost. However, the isotropic etches obtained with wet chemical etchants are difficult to control and have poor resolution [145].

High quality ‘dry’ plasma etching was developed to overcome the limitations of etching the nano scale structures. This etching consists of a chemical reaction and physical damage by ion bombardment. Operating pressure of the plasma etching plays an important role in the way the plasma reacts to the material. Figure 5.4 shows the range of etching processes related to the operating pressure [146].

Wet etching presumably on the far left is 100% chemical reaction, while across to the far right ion milling is 100% physical etching. Plasma etching, reactive ion etching (RIE) and high density plasma etching are achieved by combinations of chemical and physical etching.

The principle of plasma etching consists in that an radio frequency (RF) field

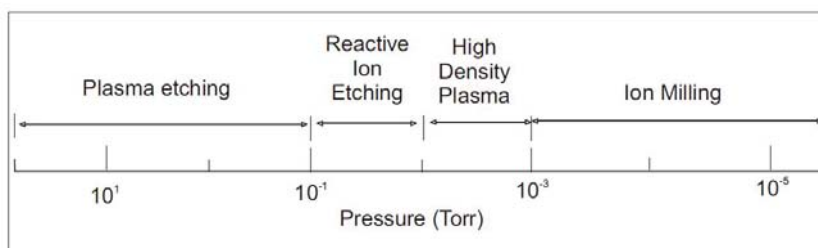


**Figure 5.4:** Different possible plasma etch processes as a function of the chamber pressure scale.

between two electrodes produces plasma. Plasma etching process is illustrated in Figure 5.5 [147].

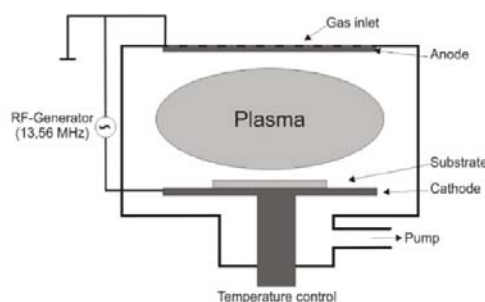


**Figure 5.5:** Schematic process of the plasma etching.

The desired amount of process gasses are controlled and mixed by mass flow controllers (MFC). Then, the mixed gases are distributed into the process chamber which is pumped and kept at a required low pressure. A standard (RF) (13.56 MHz) electric field is coupled between the two parallel-plate electrodes that ionize the process gases and generate the plasma, which includes charged ions, free electrons and neutral radicals. The electrons follow the high frequency due to their small mass and thus generate a bias voltage between the electrodes (called DC bias). The electrical field generated by the DC bias accelerates the positively charged ions perpendicular to the cathode, i. e. to the substrate. While the reactive ions etch the surface of the substrate chemically, they extract the surface material of the substrate by means of physical sputtering due to their high kinetic energy. The volatile etching product of the RIE is mostly pumped out and may partially redeposit on the substrate.

### 5.2.2 Nanoimprint Tools

Throughout this thesis two different Nanoimprint tools were used. A thermal-based tool and a UV-based tool. Figure 5.6 shows the thermal based equipment (CNI Tool from NIL Technology *ApS*), which allows imprinting on any stamp and substrate size up to 4 inch in diameter.

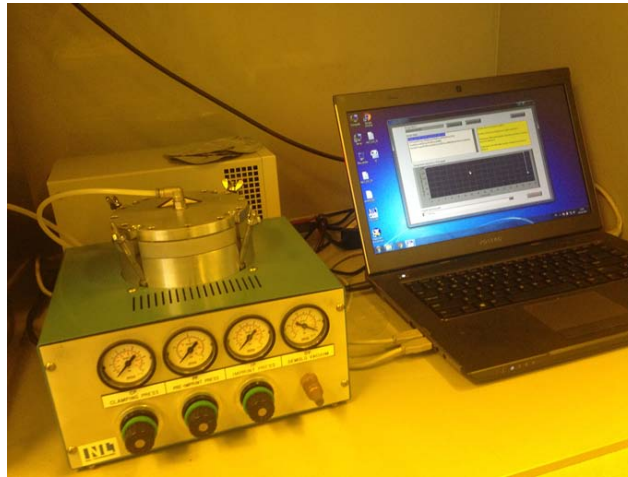


**Figure 5.6:** CNI Tool from NIL Technology *ApS*.

The pressure applied during the imprinting step is delivered by an expanding membrane, which is connected to an external line of compressed air. Electric resistance heating is provided by the named CNI solid stamp, which is in contact with spring loaded pins that deliver the electrical current. The tool comes with its own power supply and a software that lets the user set multi-steps recipes. A schematic of a typical NIL processes performed by this tool is depicted in Figure 5.7. At the beginning of the imprint process, the pressure is applied and at the same time, the power supply intensity increases until the set temperature is reached. Once the imprinting temperature is reached, the equipment maintains the temperature and pressure constant during the holding time. When the imprint process has finished, the power supply lowers its intensity and an embedded fan starts to work until the desired release temperature is reached. The operating ranges from this equipments are from 0 to 8 bars in pressure and from ambient temperature to 250<sup>0</sup>C.

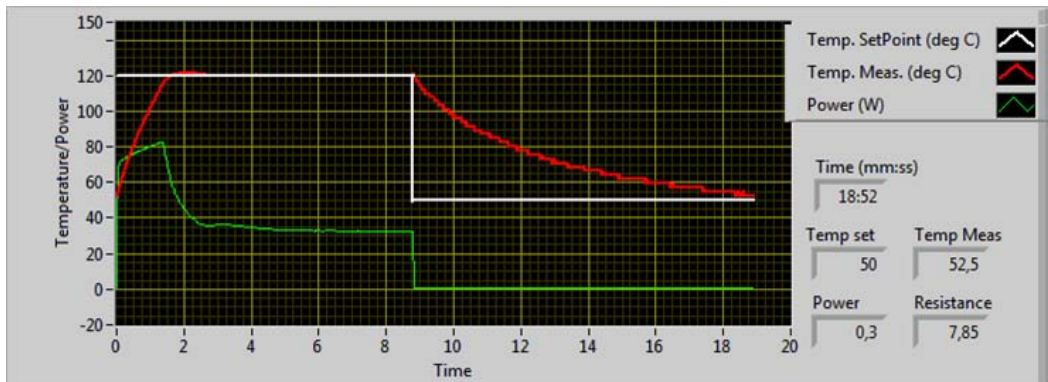


**Figure 5.7:** Schematics of thermal NIL process performed by the CNI Tool.

Figure 5.8 shows the UV-assisted NIL equipment. This equipment works at room temperature and the pressure is applied by direct injecting of air by means of a compressor. The equipment is connected to a UV-light source with a power of 200 W, which applies the light to the system.



**Figure 5.8:** Photograph of the UV-assisted NIL setup

### 5.2.3 Electroplating

As discussed in Section 4.2, throughout this thesis, electroplating technique was used in two different approaches:

- Up-plating technique was optimized and developed. In an up-plating process, a patterned resist is used as a mask to achieve Ni deposition only in the opened parts of the surface (Figure 5.9a).
- Conventional electroplating process was used in order to make metallic shims

with the 3D fabricated structures. These shims are very suitable for injection molding process, since silicon is too brittle for this purpose (Figure 5.9b).

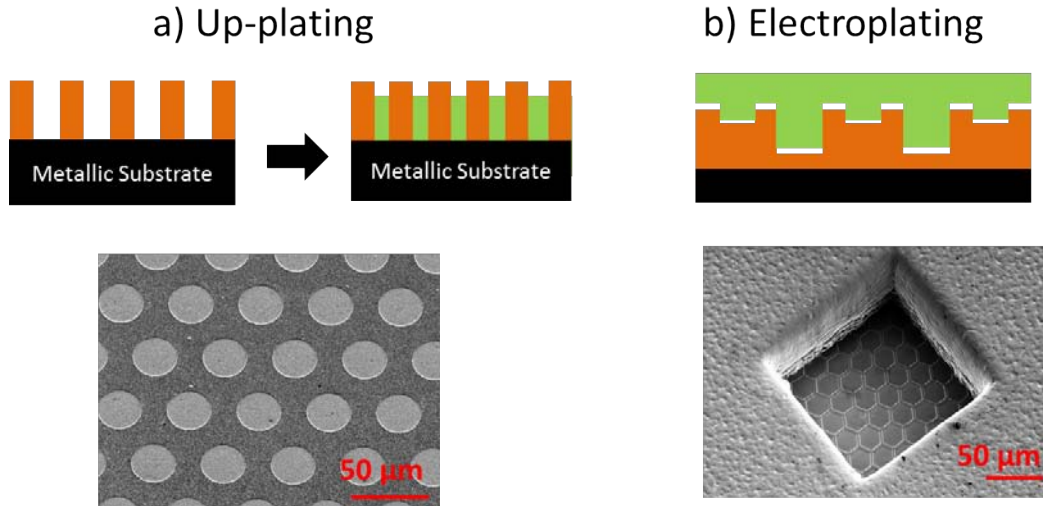


**Figure 5.9:** Schematics of the a) up-plating and b) electroplating processes with two representative SEM images.

Depending on the application and/or type of structures to be made, one of the formerly mentioned approaches can be more convenient. These two methods to produce metallic micro and nanostructures are totally different. In the up-plating approach very good adhesion of every layer added to the surface is needed, whereas the second way has a demand for separation of the structured nickel shim from the surface after electroforming (without destroying the micro and nanostructures). For this reason, it is important to take into account the metal adhesion to different surfaces. For example, for an up-plating process performed in a gold coated silicon wafer, an intermediate adhesive layer of chromium or titanium is essential to achieve a good adhesion of the electroplated material to the substrate. The main advantages and drawbacks of each method are depicted in Table 5.1.

Method	Main advantage	Main drawback
<i>Up-plating</i>	The metallic piece is ready for imprint after one step up-plating process	Adhesion between the two layers
<i>Electroplating</i>	One material piece	Defects can arise in the demolding process

**Table 5.1:** Advantages and problems of the followed electroplating-based approaches.

Figure 5.10 shows a photograph of the electroplating equipment used in this thesis. The general overview photo shows the temperature controller, used to adjust the temperature of the bath, and the power supply, used to apply the current to the system. The inside view shows the anode, where the nickel is placed, the cathode, where the surface to be plated is placed, the electrolyte and a moving system coupled to the cathode, used to avoid bubbles formation during the electroplating process.

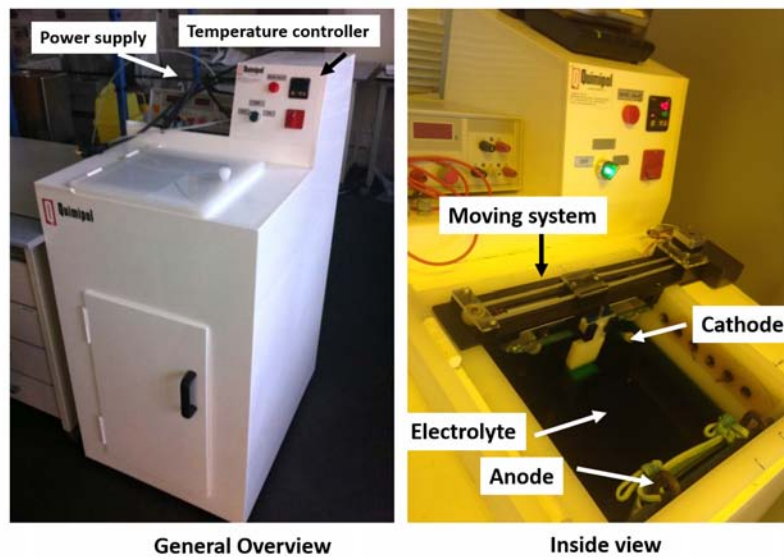


**Figure 5.10:** Photographs of the electroplating equipment used throughout this thesis.

### 5.2.4 Injection Molding

For our injection molding trials, we used an Engel Victory Tech 80/45 injection molding tool, which is installed in Denmark Technical University (DTU). The experimental validation was carried out in collaboration with our industrial partners NIL Technology ApS as part of the EU project PLAST4FUTURE. The key parts of the machine are shown in Figure 5.11, and consist on the hopper (dryer) (1) in which the polymer is dehumidified before it is sent to the heating cylinder (2) where the polymer is plasticized. The nozzle at the end of the heating cylinder injects the polymer into the cavity of the tool (3). A robot removes demolded samples and places them on a conveyer belt. The machine is operated from a series of switches and a touch screen interface (4). The robot can be operated manually with the handhold robot control unit (5). Main valves for cooling water and compressed air are situated at the wall to the left of the machine (6).



**Figure 5.11:** Photographs of the injection molding equipment used throughout this thesis.

For the experimental verification, our developed nickel shims were mounted as inserts on the stationary side of the injection molding mold. Injection molding is the main manufacturing process that industry uses to realize numerous plastic parts, components and devices. The overall process is very well studied and refers to the injection of polymer melt into a predefined mould. Several intermediate step are involved for a successful replication such as packing of polymer melt to reduce

shrinkage, cooling until the polymer melt freezes and become solid, and demolding of the finished polymer part.

The injection process is performed at high pressures, which could reach to up to several thousand tons, in function of the component that has to be molded. After the mold filling, the pressure is increased to pack the polymer. The packing is done to make sure that the finished parts are correctly dimensioned and to prevent the part from shrinking too much during cooling. After packing, pressure is applied until the polymer solidifies.

### 5.3 Characterization techniques

The characterization techniques used in this thesis can be divided into two parts: 1) Topography characterization of fabricated nano and microstructures during the entire fabrication process. 2) Characterization of wetting properties of the samples.

The optical methods of characterization are fast, easy to use and has a large field of view. The large field of view is important when characterizing big samples. To successfully fabricate superhydrophobic surfaces, samples with few defects are needed, because the liquid can pin on the defects.

#### 5.3.1 Scanning Electron Microscope

A scanning electron microscope (SEM) is a type of electron microscope that can be used to observe features much smaller than a conventional optical microscope [148]. Figure 5.12 illustrates a schematic of a typical SEM system. The electron gun is on the top of the column, produces the electrons which are accelerated by electrostatic fields towards the surface at a specified accelerating voltage or energy in keV unit. Electromagnetic lenses and apertures are used to focus the e-beam and to form a focused e-beam spot on the surface. A high-vacuum environment allows electron travel without scattering by the air. The reflection of secondary electrons (SE) or back scattering electrons (BSE) from surface topography are detected by a specialized detector and processed for the surface topography appearance.

The smallest features that can be distinguished in a SEM is typically a few nm. Furthermore, a SEM has a large depth of field. Due to the electron flow SEM



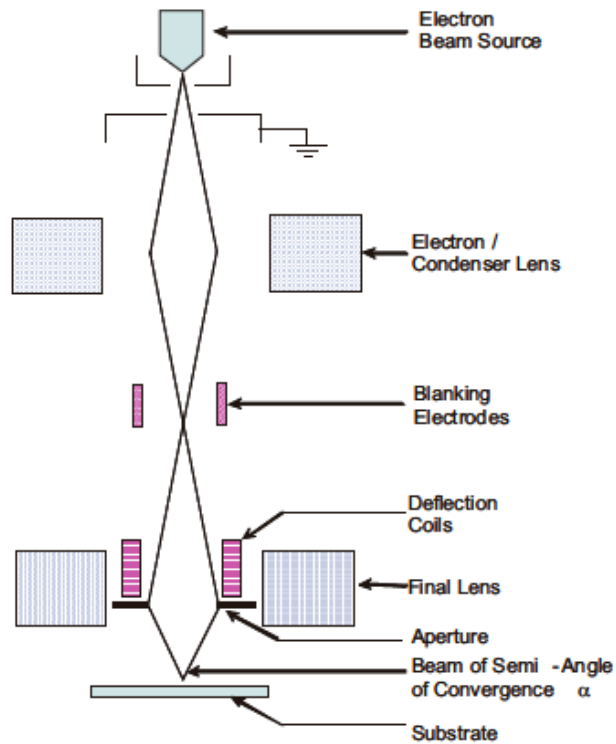


**Figure 5.12:** The schematic diagram of the scanning electron microscopy (SEM) system.

is limited to picturing conductive materials. The incoming electrons will charge insulators and consequently the image is distorted. This happens especially for polymer materials. This can be overcome by coating the surface with a thin layer of metal.

A field emission SEM (FEI Quanta 650 FEG) was used to characterize the nano and microstructures developed in this thesis (Figure 5.13). This is an environmental SEM equipment which allows the utilization of non-conductive samples without using metallic coating.



**Figure 5.13:** Photograph of the FEI Quanta 650 FEG SEM equipment used in this work.

### 5.3.2 Surface wetting

Wetting on surfaces is often characterized with a contact angle goniometer. For measuring contact angles, a technique called the sessile droplet method is typically used [26,27]. A droplet consisting of a known liquid is placed on the surface and the droplet contact angle is determined using a software and fitted to various theoretical models. The contact angle is calculated from the droplet shape, as shown in the representative example from Figure 5.14.

Dynamic contact angle data can be acquired by either tilting the entire machine or enlarging/reducing the droplet volume on the surface.

As discussed in Chapter 2, the contact angle value is not the only key parameter when measuring the wettability; the adhesion of water to the surface is very important when characterizing surfaces for a targeted application. This adhesion is measured by the contact angle hysteresis and by the sliding angle.

When the droplet is placed on a surface, it can have a range of contact angles on a specific solid surface, where the maximum possible attained contact angle is called advancing contact angle, and the minimum possible contact angles is called

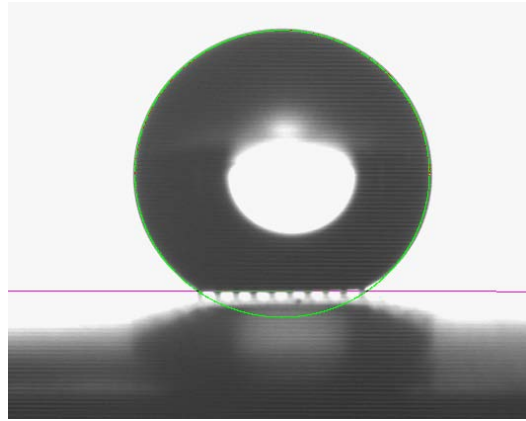


**Figure 5.14:** Contact angle measurement performed by the software from the contact angle goniometer.

receding contact angle. The advancing contact angle is measured at the triple phase line when liquid moves towards an un-wetted area, and the receding contact angle is measured at the triple phase line when the liquid moves from a previously wetted area. If droplets are placed on an ideal surface (atomic flat, chemical homogenies, and with no liquid surface interaction) the advancing and receding contact angle will be identical and equal to the equilibrium contact angle. In reality, ideally flat surfaces do not exist, since real surfaces always have some hysteresis, due to roughness or chemical variation of the surface.

Hydrophobic properties of the fabricated surfaces were characterized by determination of static contact angles, contact angle hysteresis, sliding angle, and bounce experiments with  $10 \mu\text{l}$  droplets. A modern droplet shape analysis instrument from Krüss was used to measure the wetting behavior on prepared superhydrophobic surfaces (Figure 5.15). A water droplet (smaller than the capillary length) is gently placed on the surface using a needle and its contact angle values is measured using the sessile droplet method [26].

A camera and a computer with a special commercial software were used to measure the static CA after the needle was removed. To measure the CAH a syringe is used to add and subtract water to and from the droplet which is resting on the superhydrophobic surface. When a small amount of water is removed from the droplet, the droplet will recede with a constant contact angle, which is the receding contact angle ( $\theta_R$ ). When the water is added to the droplet, then the droplet grows

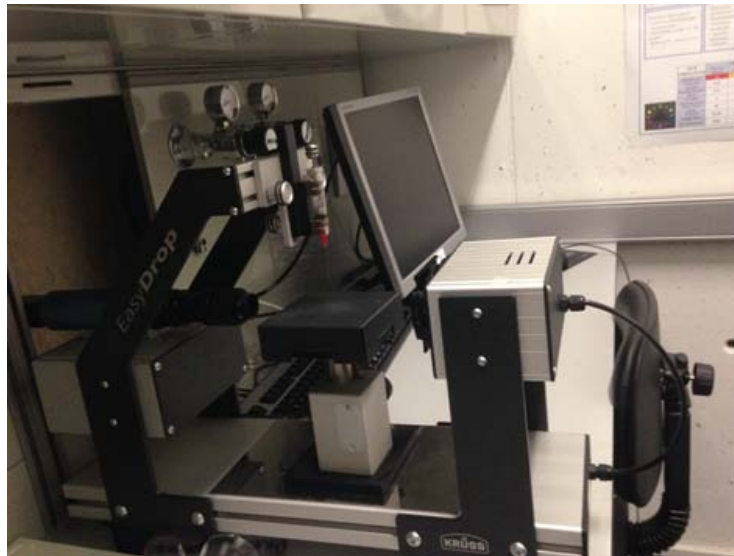


**Figure 5.15:** Photograph from EasyDroplet Standard droplet shape analysis system from Krüss.

while the contact angle is maintained at the advancing contact angle ( $\theta_A$ ).

The droplet roll-of angle and the bouncing experiments were made by using a home-made plane with a tilting option with an accuracy of  $0.5^\circ$  and a high speed camera, recording at a 1200 frames per second.

## Chapter 6

# Development of Nanopatterning Techniques

In the research work reported here, different fabrication methods were used to realize different surface functionalities. Special attention to Reverse Nanoimprint Lithography (RNIL) was paid, since it was the main process that allowed us the production of different hierarchical structures, as well as nanostructures for template-assisted electroplating. Furthermore, different manufacturing industrial techniques were tested and implemented to produce multifunctional plastic products. Details on all the fabrication procedures followed to achieve the different surfaces configurations are presented in this Chapter. Mainly soft PDMS stamps were used to achieve the pattern transfer, i.e., all the fabrication approaches followed required low imprint pressures.

### 6.1 UV-NIL

UV-based nanoimprint lithography technique is a very promising low-cost nanomanufacturing process that involves two steps. The first step is the ‘imprinting’ which relies on deforming a thin UV sensitive monomer layer using a flexible stamp that contains nanostructures and leaving a characteristic pattern in the polymer layer. The second step is the ‘curing’ process; by applying UV-light during few seconds, the resist is crosslinked and cured, giving rise to a negative copy of the

stamp.

UV-NIL was used here in different process steps for the overall fabrication of functional surfaces. The manufacturing process used to realize these surfaces will be discussed in Section 6.2.2. In this section, we will show the results of UV imprints using PDMS stamps, with 2D and 3D patterns. The resists used for UV imprints were Ormocomp and mr-XNIL26 SF, depending of the subsequently use of the fabricated sample. Figure 6.1 depicts two representative examples of the imprints obtained by UV-NIL.

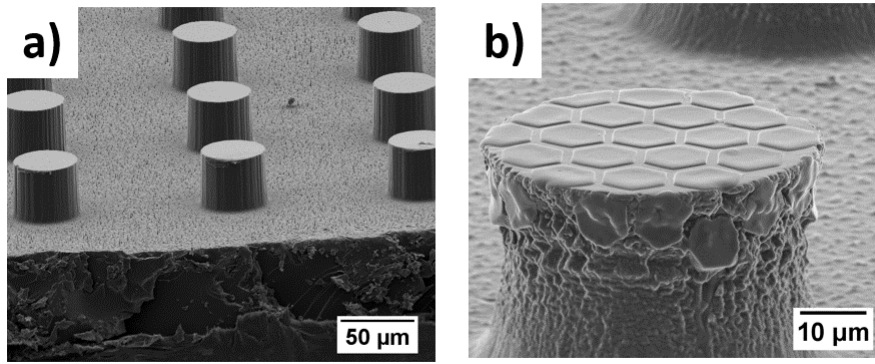


**Figure 6.1:** SEM images of a) 2D micropillars pattern imprinted in Ormocomp by UV-NIL and b) 3D hierarchical pattern imprinted in mr-XNIL26 SF by UV-NIL.

The optimized imprint parameters used for each resist are given in Table 6.1. The process conditions during the imprint step will directly influence the flow behavior, which determines the accuracy of the final geometry of imprinted microscale structures.

Since sufficient material is needed to fill the stamp cavities, the resist viscosity is a key parameter during the resist deposition step. When the resists were spin coated at 3000 rpm during 30 seconds, Ormocomp gave thicker films than mr-XNIL26 SF (i.e. it is more viscous). For this reason, a higher spin velocity is needed to achieve desired film thickness for a higher viscosity. For the spin coating parameters depicted in Table 6.1, a resist film of  $15\ \mu\text{m}$  is achieved in both cases. This film thickness was enough to completely fill our structures. Due to the lower viscosity for the case of the mr-XNIL26 SF, more pressure and longer time were needed to produce a good pattern replication of our structures.

Resist	Thickness	Spin Coating	Imprint	Curing
<i>Ormocomp</i>	15 $\mu\text{m}$	3000 rpm 30 sec	3 bar 4 min	10 sec
<i>mr-XNIL26 SF</i>	15 $\mu\text{m}$	500 rpm 30 sec.	5 bar 7 min	3 sec

**Table 6.1:** Imprinting conditions used in soft UV-NIL for imprints with the two photocurable resists used in this thesis.

The experiments were performed at room temperature and the UV time varied alternatively between 1 to 20 sec. A careful optimization of the UV-curing time was needed in order to obtain good quality replicas of the imprinted features. A curing time of 3 and 10 sec was sufficient for *mr-XNIL26 SF* and *Ormocomp*, respectively.

## 6.2 Reverse NIL

A novel imprint based process, namely reverse nanoimprint lithography, was further developed and implemented for several targeted applications. Figure 6.2 shows the two different approaches used upon which this novel technique is based, and its subsequent application.

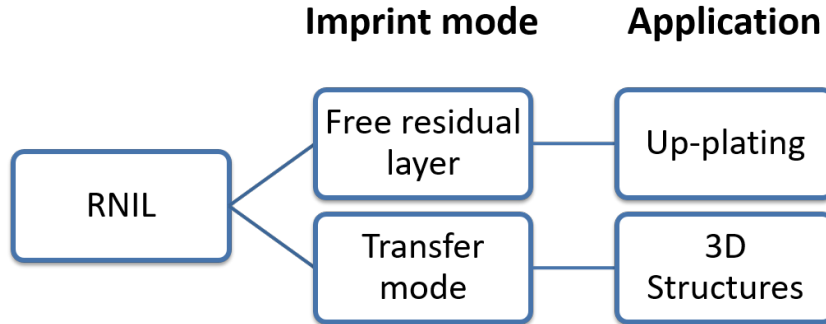


**Figure 6.2:** Diagram showing the targeted applications obtained with the RNIL method developed in this thesis.

In the context of the PLAST4FUTURE EU project, RNIL was optimized to produce zero residual layer imprints and further utilize them as masks in a subsequent up-plating process. These directly electroplated nanostructures were used as inserts in injection molding tools to produce multifunctional plastic products.

This RNIL technique was tailored to realize a variety of different structures, and used to produce 3D hierarchical surfaces in a controlled manner. The possibility of having 3D structures with a controlled topography allowed us to achieve a precise control over the wetting properties of the fabricated surfaces.

### 6.2.1 Free-Residual layer NIL

Although NIL has been extensively developed, there are still issues that need to be addressed to become a mature nano manufacturing technology. One of the challenges is the removal of the residual layer after the imprinting step. Regardless of the type of polymer resists used, a residual layer will always remain between the elevated parts of the stamp and the substrate. Most applications require the elimination of this residual layer via a reactive ion etching (RIE) post processing step. Although RIE is a well-controlled process this additional step increases the overall processing complexity, implies an additional cost and decreases the throughput of the nanoimprint process.

Various methods have been used to create residual layer-free imprints. Attempts include partial UV-curing the resist followed by an additional chemical development process [149, 150], using flexible molds to directly contact the substrate in order to eliminate residual layer [151, 152] and selective filling into the recessed areas of the mold followed by transferring the polymer patterns to a substrate [153, 154].

Hyunsoo et al. (2009) [154] tried to remove the residual layer from a surfactant-coated silicon mold. By creating an incompatibility between the surface and the resist, they induced a dewetting process. Heating the substrate above the glass transition temperature of the polymer, the top of the mold could be moved to mold trenches. Kao et al. (2011) [153] performed a residue-free RNIL by means of a self-assembled monolayer-treated silicon mold, inducing a selective filling of the mold by spin coating. All these free residual layer imprints were achieved by means of various process steps, involving chemical treatments. Furthermore, in all cases hard silicon molds were used, which imply higher imprint pressures and limits the possibility of transferring the process to free-form surfaces.

In this section we introduce a novel one-step residual-layer-free patterning



method (Figure 6.3). By means of the RNIL flexible lithography technique, polymer structures with no residual layer over  $cm^2$  areas on silicon and metallic substrates were obtained as well as on pre-patterned substrates.

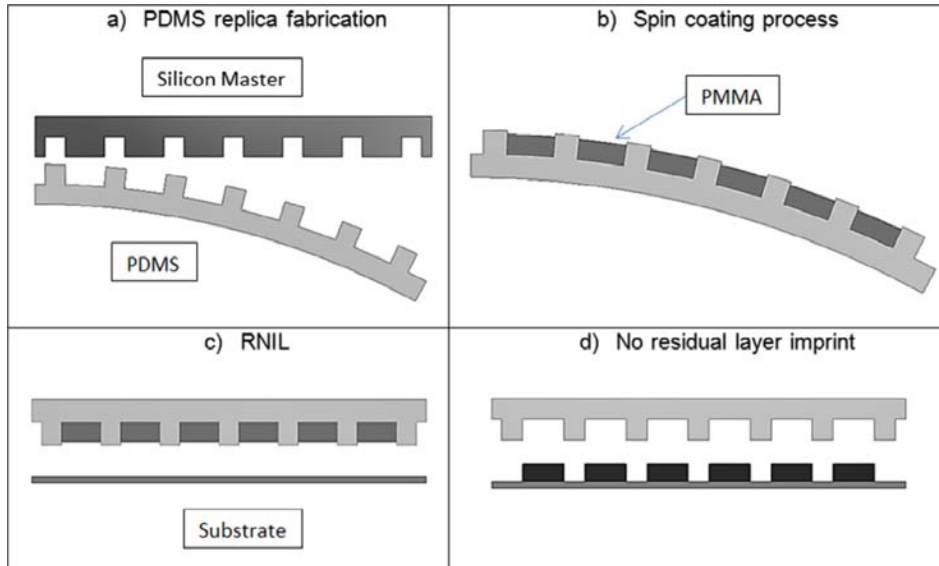


**Figure 6.3:** Schematic illustration of the residual-layer-free reversal NIL process.

### Stamp design & Replica fabrication

This work was developed inside the PLAST4FUTURE framework, therefore a design developed by the Technical University of Denmark (DTU) was used, consisting of a honeycomb-like microstructure (Figure 6.4).

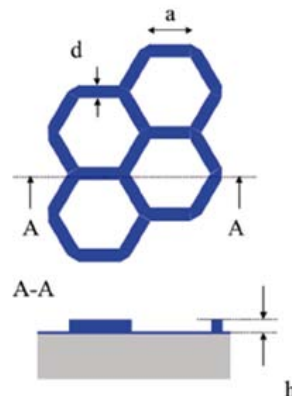


**Figure 6.4:** Schematic of the honeycomb-like structure used in this work.

This design corresponds to a superhydrophobic structure that favours the Cassie-Baxter state, where  $a$  is  $5\ \mu\text{m}$ ,  $d$  is  $500\ \text{nm}$  and  $h$  is  $800\ \text{nm}$ . As it will be discussed in Chapter 7, these geometrical parameters yield a solid-liquid contact fraction of 0.12, which corresponds to a 12% of the surface in contact with the drop. The silicon wafers were fabricated in NIL Technology *ApS*, with patterns defined by electron-beam lithography followed by a reactive ion etching step to create the full silicon master mold. The designed stamp is depicted in Figure 6.5.

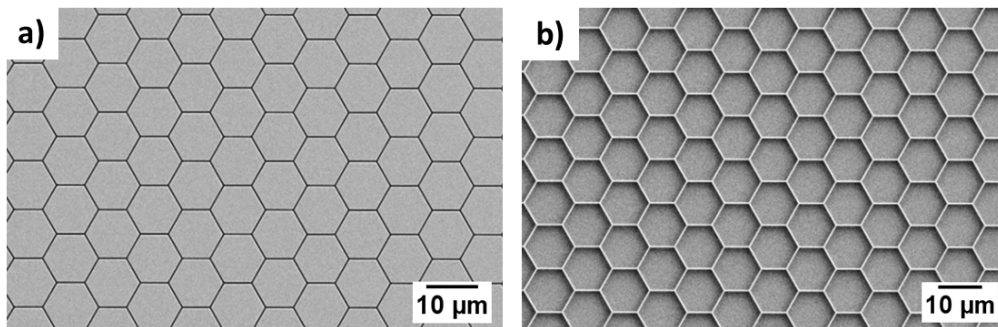


**Figure 6.5:** a) SEM image of the positive honeycomb pattern. b) SEM image of the negative honeycomb pattern.

The target application of this process was to adapt the developed fabrication method to non-planar surfaces. For this reason polydimethylsiloxane (PDMS) was selected as the optimum material for replication of the mold. The PDMS mold used in this work was fabricated according to the experimental procedure mentioned in Section 5.1.1.

### Resist deposition

The polymer deposition onto the PDMS mold is a crucial step since it is necessary to selectively and completely fill in the cavities of the stamp, to avoid undesired deposition on the elevated parts of the features, which would lead to a remaining residual layer on our final imprints. The deposition of the polymer is carried out by spin coating, thus achieving a selective filling, avoiding resist deposition on the top of the features. A compromise between the resist viscosity, as well as the spin coating velocity had to be found in order to achieve the optimum selective deposition parameters. The first pattern selected was the honeycomb-like structure with the

negative polarity (lines) (Figure 6.5b).

The first resist used was micro resist GmbH mr-NIL 6000E. Figure 6.6 depicts examples of coating at 1500, 3000 and 4000 revolutions per minute (rpm) during one minute.

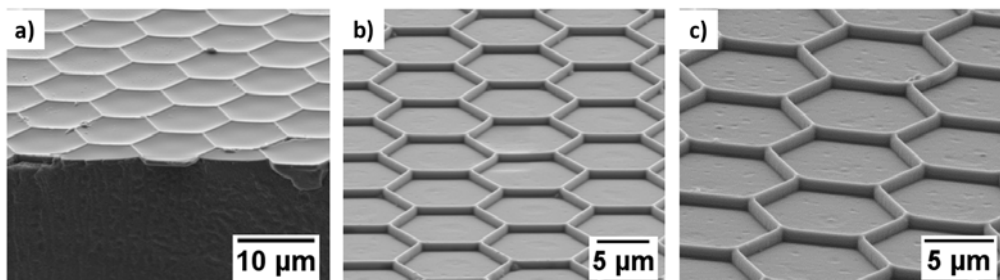


**Figure 6.6:** SEM image PDMS stamps coater with mr-NIL 6000E at a) 1500 rpm, b) 3000 rpm and c) 4000 rpm for 1 minute.

The images show a poor wettability and control over the deposition. At low velocities, an excess of polymer is observed, leading to a residual layer after the imprint process. On the other hand, at higher velocities the resist disappears completely from the PDMS stamp. These results show the need to improve the PDMS wettability for a better resist deposition. A chemical functionalization of PDMS was selected to make it hydrophilic. It was based on self-assemble a layer of polymer on the surface, allowing us to tailor the surface properties of the material. This process was carried out with the ‘Grafting to’ method [155]. It consists of a PDMS surface activation with an oxygen plasma, followed by covering the surface with polyethylene glycol (PEG 200 MW) during one minute. Finally, the surface is rinsed and cleaned with DI water.

After this functionalization, the wettability of the PDMS surface was improved, as can be observed in the from the SEM inspection (Figure 6.7).

While the coverage of the resist was improved, the uniformity and the selective deposition of this coverage were hindered after the functionalization. This lack of uniformity could lead to a thick and uneven residual layer after the RNIL imprint step, which is completely undesirable in our work. Due to the lack of uniformity obtained both with and without functionalization using the mr-NIL 6000E resist, a change towards poly(methylmethacrylate) (PMMA 75K) was carried out. This

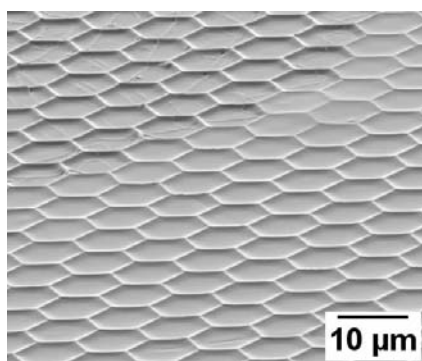


**Figure 6.7:** SEM image of mr-NIL 6000E coated PDMS stamps after PEG functionalization.

resist offered better coverage results than the former one, even without the need of chemical functionalization. In Figure 6.8 an improvement can be observed both in terms of coverage and uniformity.

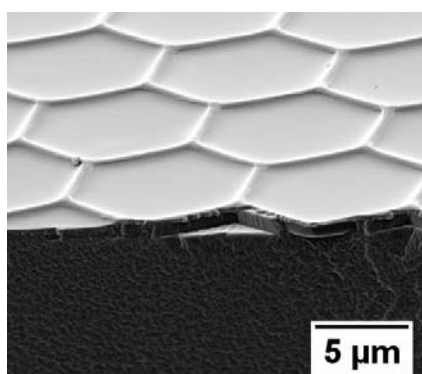


**Figure 6.8:** SEM image of PMMA 75K coated PDMS stamp at 4000 rpm during 1 min.

However, an excess of resist on the features is still observed, leading to an undesired residual layer. After selecting 4000 rpm during 1 minute as the optimum spin coating parameters for complete filling of the cavities, the resist viscosity was modified in order to try to avoid resist deposition on the features. Two PMMA dilutions in anisole were prepared, yielding respectively a viscosity of  $3.2 \text{ mPa} \cdot \text{s}$  and  $5.2 \text{ mPa} \cdot \text{s}$ .

After this dilution, a clear improvement was observed in the coverage of the PDMS stamp (Figure 6.9). SEM inspection showed clearly that the PMMA filled the cavities of the stamp, leaving no resist on surface features. This ideal filling helped us to obtain imprints with no residual layer, in addition to the large area pattern transfer fidelity.

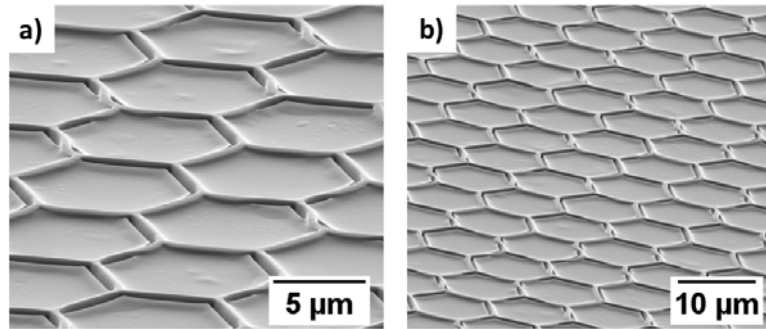


**Figure 6.9:** SEM images of diluted PMMA spin coated on PDMS stamp, speed 4000 rpm for 1 minute (a) PMMA with a viscosity of  $3.2 \text{ mPa} \cdot \text{s}$  and (b) PMMA with a viscosity of  $5.2 \text{ mPa} \cdot \text{s}$ .

### Reserve nanoimprint lithography

The first imprints were performed with the mr-NIL 6000E resist. The only spin coating parameters that yielded coverage with this resist were 1500 rpm during 1 minute. The imprints were performed at low temperature, near the glass transition temperature of the resist  $1^\circ\text{C}$ , and at low pressure, compared to commonly used pressures used in NIL. The low imprinting pressures prevent deformation of the stretchable and flexible stamp. The pressures were varied from 0 bar to 3 bar, finding the optimum to be 2 bar. An example is shown in Figure 6.10, where a good pattern transfer is observed.

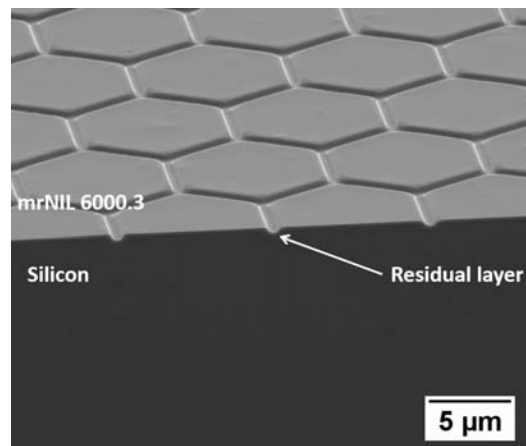


**Figure 6.10:** SEM images of RNIL with mr-NIL 6000E resist on silicon. The imprint parameters were  $40^\circ\text{C}$ , 2 bar during 3 min.

However, a residual layer was still observed, that could be removed by reactive ion etching (RIE), thus increasing the additional required steps to achieve the targeted

application.

Due to the difficulties on the uniform coverage on the PDMS stamp with the mr-NIL 6000E resist, a change to PMM75K was realized. The pressure and the imprinting time were kept constant from the test with mr-NIL 6000E, but the temperature was changed to select one close to the glass transition temperature ( $110^{\circ}C$ ). This imprint temperature allows to the PMMA to flow from the PDMS stamp to the substrate. An example of the imprint is shown in Figure 6.11. The SEM image shows an accurate pattern transfer, but also residual layer is observed.

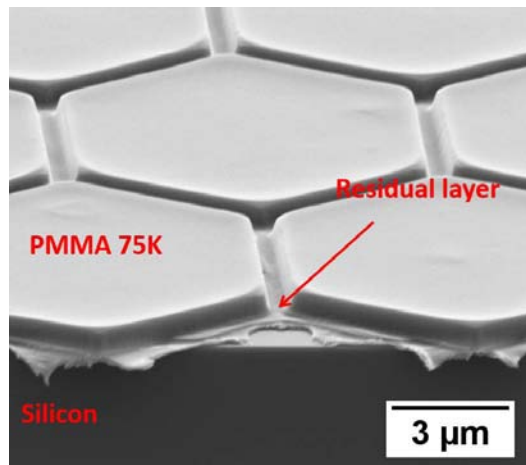


**Figure 6.11:** SEM images of RNIL with PMMA 75K resist on silicon. The imprint parameters were  $110^{\circ}C$ , 2 bar during 3 min.

As discussed in the previous section, a modification of the resist viscosity can avoid the presence of the residual layer. Dilution on PMMA 75K yielded satisfactory results, as shown in Figure 6.12.

The imprints were performed at  $110^{\circ}C$ , 1 bar of pressure and 3 minutes of holding time. We demonstrate that decreasing the PMMA 75K viscosity definitively improves the quality of the imprints and residual layer free transfer is achieved. It is important to notice that there exist a slight variation in critical dimensions of the hexagons separation in comparison with original silicon stamp, more accentuated in the imprints performed with the lower viscosity resist (PMMA  $3.2 mPa \cdot s$ ). This is probably due to the fact that in this situation the filling of the cavities is lower than in the case of the PMMA  $5.2 mPa \cdot s$ .

This technique was further developed and demonstrated over different non-planar

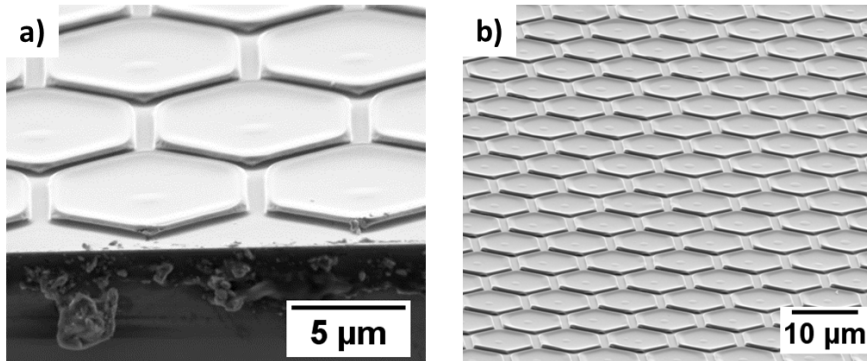


**Figure 6.12:** SEM images of RNIL with diluted PMMA 75K resist on silicon with viscosities of a)  $5.2MPa \cdot s$  and b)  $3.2MPa \cdot s$ .

substrates, such as nickel electroplated steel wafers, and nickel sulphide electroplated steel wafers. These wafers were performed in Karlsruhe Institute of Technology (KIT). RNIL imprint of PMMA  $5.2mPa \cdot s$  on nickel and nickel sulphide are shown in Figure 6.13 and Figure 6.14.

Figure 6.13a shows a photograph of a pattern transferred onto a nickel coated steel substrate demonstrating reflective holographic colors over a  $1\text{ cm}^2$  area. Figure 6.13b shows a cross section SEM image of the honeycomb structures on the nickel coated steel substrate. From the SEM inspection we could clearly see that there is no residual layer in the interspace between the imprinted features.

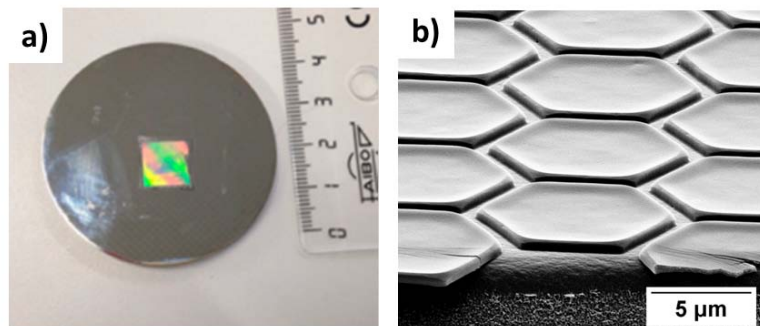


**Figure 6.13:** a) Photograph of a large area imprint on a nickel-coated steel wafer and b) SEM image of the honeycomb structure with no residual layer on a nickel-coated substrate.

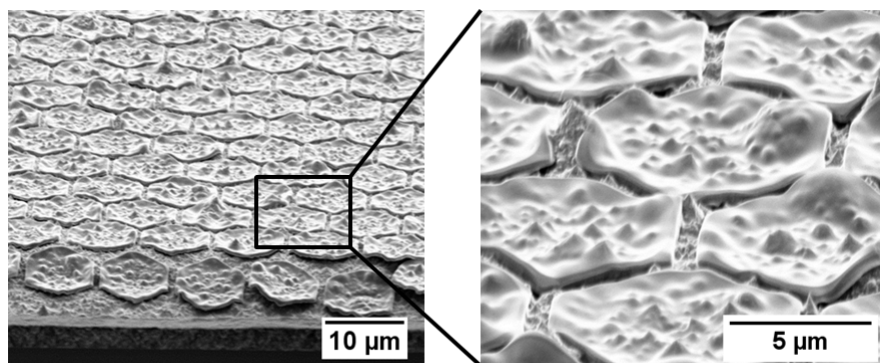


**Figure 6.14:** Tilted SEM image of a honeycomb polymer structure, which is reverse imprinted on a nickel-coated silicon substrate with high roughness of the nickel surface.

Figure 6.14 presents a tilted view SEM image of the honeycomb structures on a nickel sulphide coated silicon wafer, thus demonstrating the feasibility of imprinting on rough surfaces. Even with the high roughness present on the surface, a good pattern transfer can be clearly observed, as well as no residual layer.

Furthermore, the RNIL approach reported here was found to be also suitable to transfer defined structures onto pre-patterned substrates. Figure 6.15 exhibits SEM images of two examples of imprints on patterned silicon wafers, under the same imprint conditions as in the other experiments. The transferred PMMA honeycombs appear clearly on the existing features present in the silicon wafer. These honeycombs are well defined, there is no residual layer and their shape adapts to the changing morphology beneath them, as expected from our process conditions and parameters.

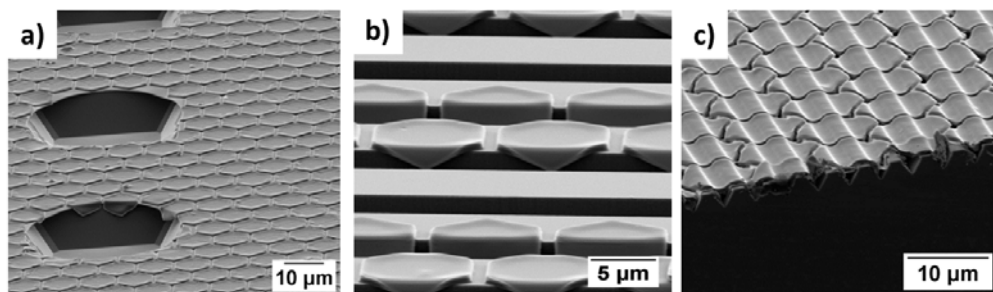


**Figure 6.15:** Tilted SEM image of honeycomb polymer structures reverse imprinted on pre-patterned silicon surfaces on a) holes, b) lines with a size bigger than the honeycomb pattern and c) lines with a size smaller than the honeycomb pattern.



The developed RNIL technique has two main advantages compared to other conventional nanoimprint-based techniques, namely:

- The lack of residual layer shortens the overall process, allowing direct metal deposition after one-step imprint.
- The adaptability of the stamp allows pattern transfer over rough and pre-patterned surfaces, paving the way to developed 3D surfaces in a really easy manner.

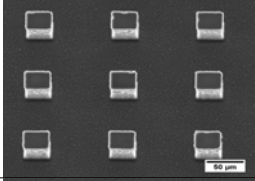
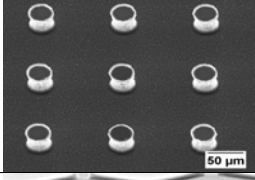
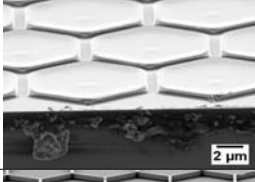
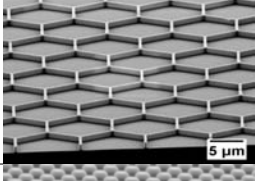
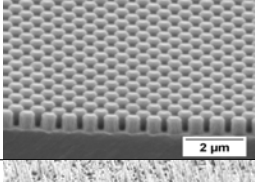
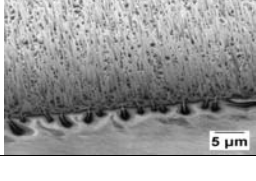
This technique was further implemented throughout this thesis to develop 3D structures with different combinations of micro and nano structures for superhydrophobic applications.

### 6.2.2 RNIL for 3D hierarchical structures

The advantage of our RNIL technique to pattern on non planar surfaces was used to achieve controlled 3D hierarchical surfaces for superhydrophobic applications. The fabricated 3D surfaces were used as templates which were replicated in PDMS and used to directly imprint in our targeted material. Tailored micro and nanostructures were selected in function of their optimum wetting behavior. Further details on how these structures are optimum for superhydrophobicity are given in Chapter 7.

Table 6.2 compiles the geometrical parameters as well as exemplary SEM images of the studied structures. The mold with the microstructures had a square array of squared and cylindrical pillars, with a width, pitch and height of 40, 115 and 40  $\mu\text{m}$ , respectively. Molds with honeycomb structures were used in both possible polarities. Honeycomb designs with 800 nm feature height and 500 nm trench separations were used. The nano pillars had a diameter, pitch and height of 500, 750 and 700 nm, respectively. The mold with the nano spikes resulted in a random distribution of pillars with a diameter from 200 to 600 nm with heights ranging from 1 to 3  $\mu\text{m}$ .

In this Section we will present the fabrication approach that we followed to produce our 3D hierarchical structures, by means of a two step process. Firstly, we started with a UV-NIL process, already mentioned in Section 6.1, followed by a RNIL process on the pre-patterned surfaces. By tailoring the fabrication parameters, we can produce two different configurations of hierarchical surfaces, as depicted in Figure 6.16.

Geometrical parameters of molds				
<i>Surface Structure</i>	<i>Width</i>	<i>Pitch</i>	<i>Height</i>	<i>Image</i>
Squared pillars	40 $\mu\text{m}$	115 $\mu\text{m}$	40 $\mu\text{m}$	
Cylindrical pillars	40 $\mu\text{m}$	115 $\mu\text{m}$	40 $\mu\text{m}$	
Honeycomb pillars	5 $\mu\text{m}$	500 nm	800 nm	
Honeycomb lines	5 $\mu\text{m}$	500 nm	800 nm	
Nano pillars	500 nm	750 nm	700 nm	
Nano spikes	200-600 nm	Random	1-3 $\mu\text{m}$	

**Table 6.2:** Dimensions and SEM images of the different structures studied in this thesis.

Ormocomp was spin-coated on the silicon wafer, and the PDMS mold was placed on the resist surface (Figure 6.16a). Then, pressure and UV light were applied to crosslink the resist (Figure 6.16b). PMMA was selected as the material to transfer the nanostructures, due to its high resolution and easy viscosity modification. A PDMS mold was used to reverse imprint the PMMA nanostructures on the microstructures

by means of the previously reported method. Fine tuning of resist viscosity and spin coating parameters were needed in order to achieve high quality and accurate imprints for each structure. The coated PDMS replica was placed on the microstructures at a fixed temperature (Figure 6.16c) and depending on the imprint pressure and time, two different kinds of transfers could take place. Figure 6.16d.1 shows the inking mode, where the applied pressure is low and the transfer take place only on the elevated parts of the microstructures. Figure 6.16d.2 shows the intact mode, where the applied pressure is high and the transfer take place both on the top and at the bottom of the micropattern. The parameters used to obtain the 3D structures with both methods are listed in Tables 6.3 and 6.4.

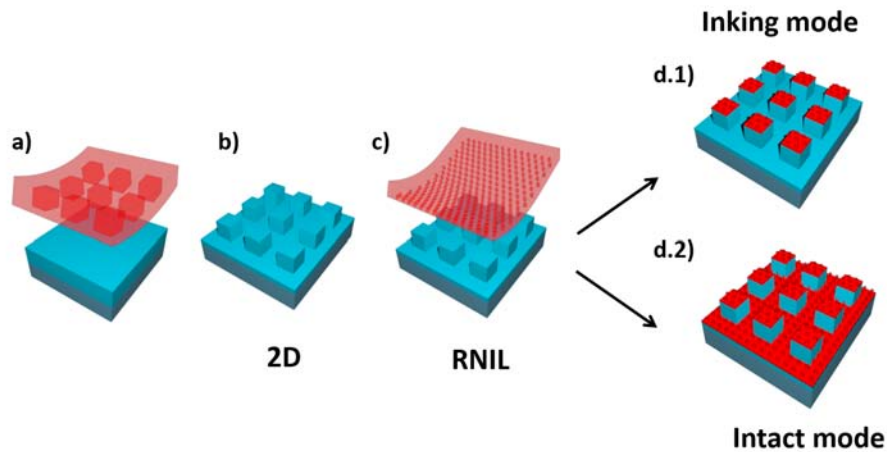


**Figure 6.16:** Schematic of the fabrication of the 3D hierarchical surfaces. The microstructures were fabricated by UV-NIL followed by a RNIL process to transfer the nanostructures from the mold to d.1) the top of the microstructures or d.2) the whole microstructure.

Imprint parameters for the Inking mode			
<i>Structure</i>	<i>Resist viscosity (mPa · s)</i>	<i>Spin coating</i>	<i>Imprint</i>
Honeycomb Pillars + Squared pillars	5.6	4000 rpm 1 min.	110 °C 1 bar 5 min
Honeycomb Lines + Squared pillars	3.2	3000 rpm 1 min	120 °C 2 bar 10 min
Nano Pillars + Squared pillars	4.8	2000 rpm 1 min	115 °C 1.5 bar 7 min
Nano Spikes + Squared pillars	4.8	3000 rpm 1 min	110 °C 1 bar 5 min

**Table 6.3:** Imprint parameters to fabricate 3D structures with the inking mode.

Imprint parameters for the Intact mode			
<i>Structure</i>	<i>Resist viscosity (mPa · s)</i>	<i>Spin coating</i>	<i>Imprint</i>
Nano Pillars + Cylindrical pillars	4.8	2000 rpm 1 min	120 °C 4 bar 10 min
Nano Spikes + Cylindrical pillars	4.8	3000 rpm 1 min	115 °C 5 bar 10 min

**Table 6.4:** Imprint parameters to fabricate 3D structures with the intact mode.

As shown in Table 6.3, the inking mode corresponds to a low pressure imprint, where the transfer of the nanostructures take place only on the elevated parts of the microstructures. Figure 6.17 depicts a series of SEM images with the fabricated 3D structures with the inking mode.

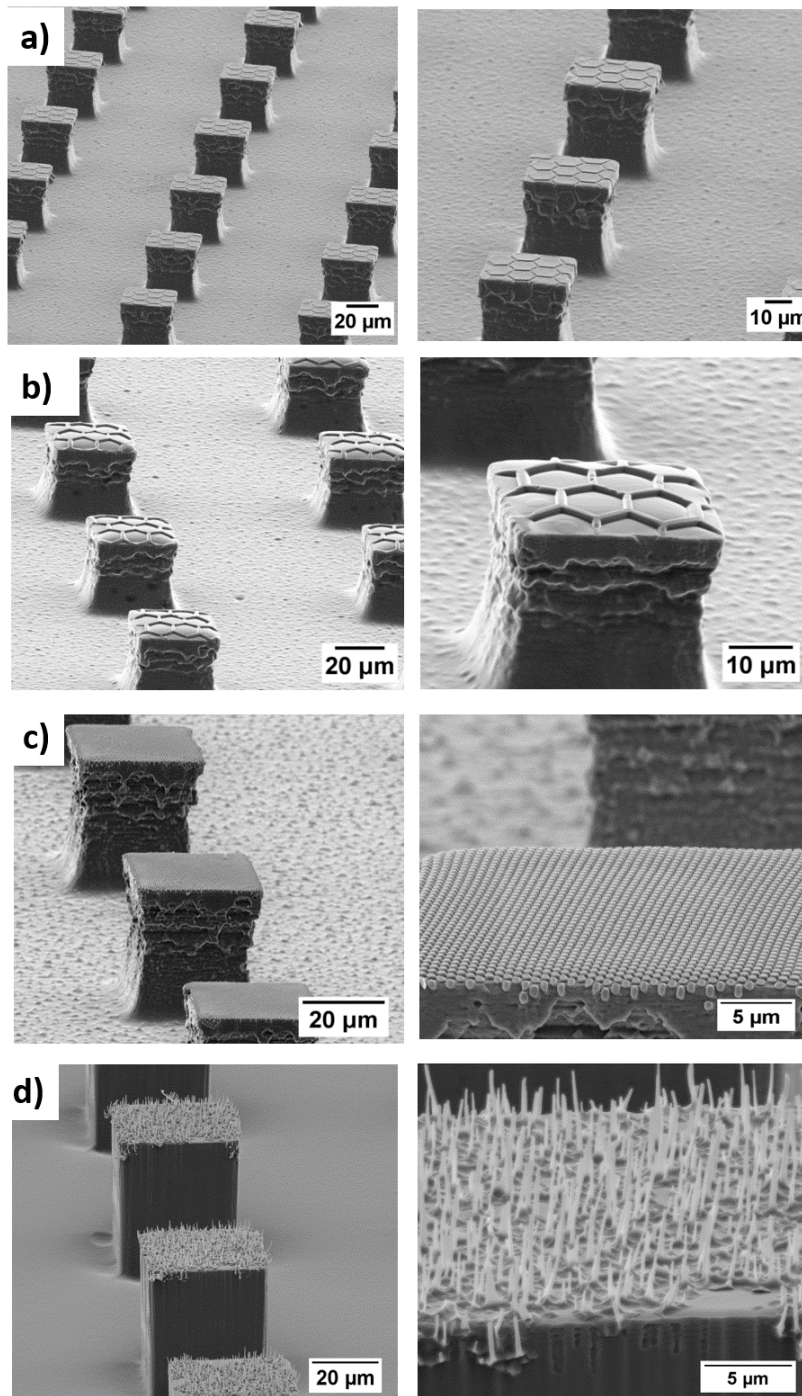


**Figure 6.17:** Tilted view SEM images of squared micropillars with several nanostructures on the top surface, a) the honeycomb pillar structure, b) honeycomb line structure, c) nanopillars and d) nanospikes on top.

An excellent pattern transfer can be observed, maintaining the original geometrical parameters for all the transferred nanostructures.

Table 6.4 shows the imprint parameters used to fabricate the surfaces with the intact mode, which corresponds to a high pressure imprint, where the transfer of the nanostructures take place both on the elevated parts and at the bottom of the microstructures. Figure 6.18 shows a series of SEM images of the fabricated 3D structures with the inking mode.

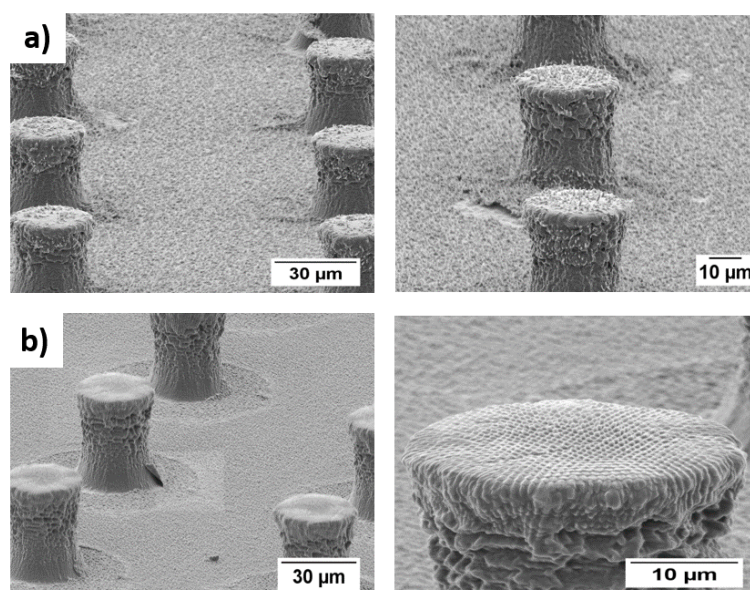


**Figure 6.18:** Tilted view SEM images of cylindrical micropillars decorated with nanostructures with the intact mode. a) Nanospikes on micropillars and b) Nano pillars on micropillars.

In the intact mode, the fidelity of the transfer is not as good as in the inking mode, since, due to the high imprint pressure, the pattern is slightly deformed at the corners of the structures. However, as it will be discussed in the Chapter 7, these structures exhibit important superhydrophobic properties.

### 6.3 Electroplating and Up plating

As discussed in Chapter 4, two different electroplating based approaches were followed, as indicated in the schematic diagram of Figure 6.19:

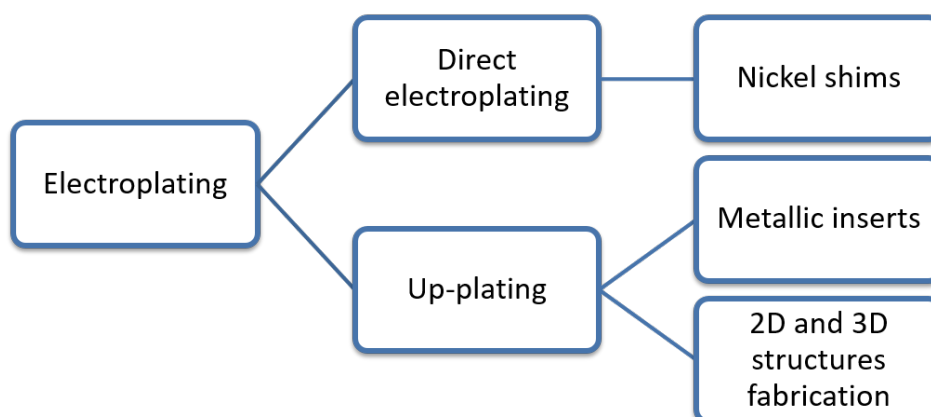


**Figure 6.19:** Schematic diagram of the different electroplating-based approaches followed in this thesis and their corresponding purposes.

1. Electroplating was used to fabricate templates from the 3D structure, for its subsequent use in injection molding.
2. Up-plating or template-assisted electroplating approach was used either to produce nickel shims and to produce structured metallic surfaces for a specific functionality.

The basic principle was the same in electroplating and in up-plating, however, the deposition conditions were changed depending on the surface area to be plated.

### 6.3.1 Electroplating

Nickel templates were fabricated by electroplating a silicon wafer with the pattern made in Ormocomp. The Ormocomp is stable enough to survive the whole electroplating process. However, electroplating process requires a conductive surface; in order to achieve this, a 25 nm thick seed layer of Au was deposited with an electron beam evaporator. Subsequently a 300  $\mu\text{m}$  thick nickel layer was electroplated with a deposition rate of 12  $\mu\text{m}/\text{h}$ .

After electroplating, the remaining Ormocomp was removed by RIE. Simple  $\text{O}_2$  is not suitable to remove the Ormocomp, since because of its hybrid nature,  $\text{SiO}_2$  will appear. For this reason, a specific combination of gasses ( $\text{C}_4\text{F}_8$  : 80sccm;  $\text{O}_2$  : 800sccm at a power of 1200W/100W) was needed. The RIE time was depending on the structures, being between 20-60 min.



Figure 6.20 depicts a set of representative images of nickel shims fabricated by electroplating. It can be observed a good quality of the electroplating process both on the nanostructures and the microstructures. The process allowed us to fabricate 3D stamps for injection molding purposes.

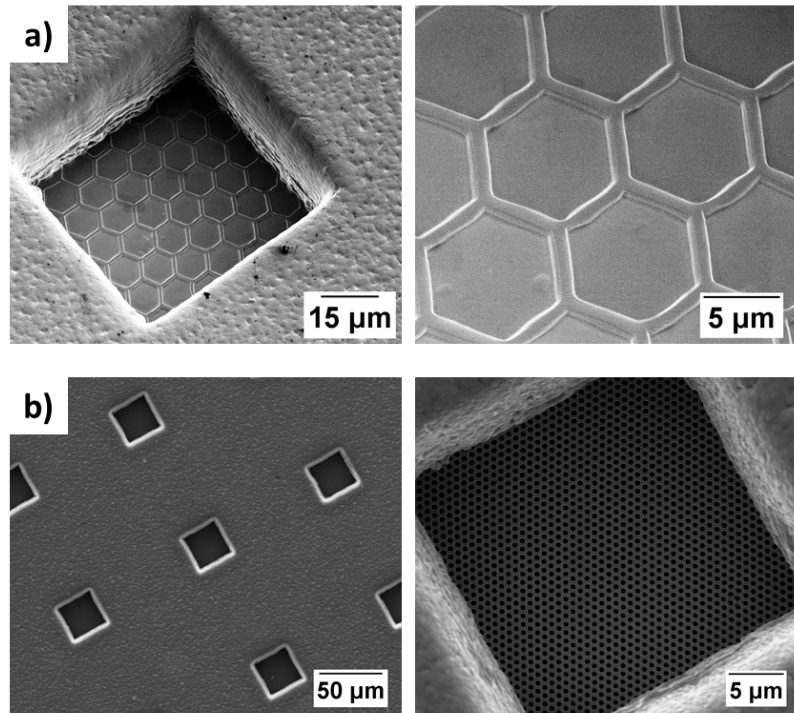


**Figure 6.20:** Tilted view SEM images of nickel shims fabricated by electroplating. a) Negative pattern of the honeycomb pillars on micro pillars, b) Negative pattern of nano pillars on micro pillars.

### 6.3.2 Up-plating

In this thesis we developed a novel method to create full metallic micro or nano structured surfaces on planar or free forms surfaces. As described in Section 4.2, nickel up-plating process involves a patterned polymer layer, which is used as a mask to up-plate metal wires within the opened windows/channels of the metal substrate.

Within this thesis we developed a nanoimprint based process to create nanoscale residual layer free structures and therefore use them as templates for the nickel up-plating process (Figure 6.21). The NIL method developed is described in Section 6.2.1. Alternatively, for micro scale dimension structures we used standard

photolithography processes to create the mushroom-like structures, as shown in Figure 6.22.

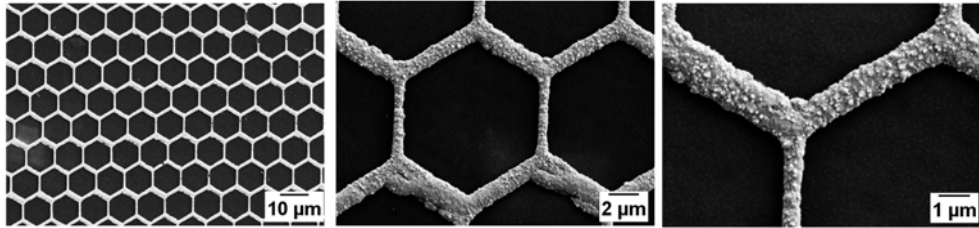


**Figure 6.21:** SEM images of nickel shims fabricated by up-plating. The honeycomb pattern was created with PMMA by means of the free-residual layer RNIL developed in Section 6.2.1.

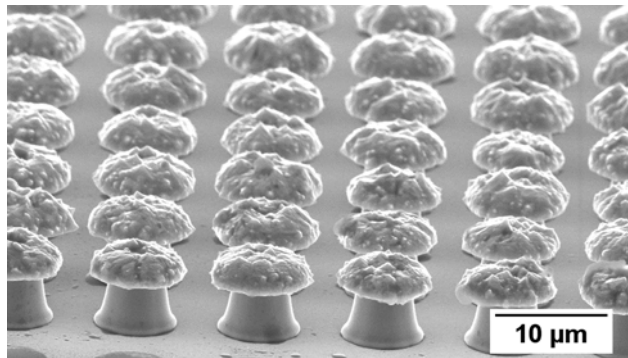


**Figure 6.22:** SEM images of fully metallic nickel surfaces fabricated by the up-plating process. The original mask consisted in an array of cylindrical holes made by photolithography.

Each lithography method has its advantages and disadvantages. For example, the photolithography is a very well known process and can allow simplicity to the process; however, it has a limited resolution that hinder the possibility of creating nanoscale structures. In contrast, the NIL based method is a versatile approach suitable for both micro and nano scale patterning and offers the opportunity to structure over free form (curved) surfaces.

## 6.4 Injection Molding

A single cavity injection molding tool, designed for research purposes (described in Section 5.2.4) was used for the production of polymer parts. Different molding conditions were used, depending on the polymer used and on the structures to be molded.

For TOPAS, the molding temperatures were  $115^{\circ}\text{C}/130^{\circ}\text{C}$ , where the right number is the temperature on the side where the shim is mounted and the left temperature is on the opposite moving part of the tool. The holding pressure was 1150 bar, applied for 6 seconds. The polymer part was demolded when the temperature was  $70^{\circ}\text{C}/82^{\circ}\text{C}$ .

For the PP, the molding temperatures were  $80^{\circ}\text{C}/100^{\circ}\text{C}$ . The holding pressure was 900 bar, applied during 10 seconds. The polymer part was demolded when the temperature was  $60^{\circ}\text{C}/60^{\circ}\text{C}$ . The main issues in the injection molding process were the filling of the nanostructures and the demolding process, as it can be observed in Figure 6.23.

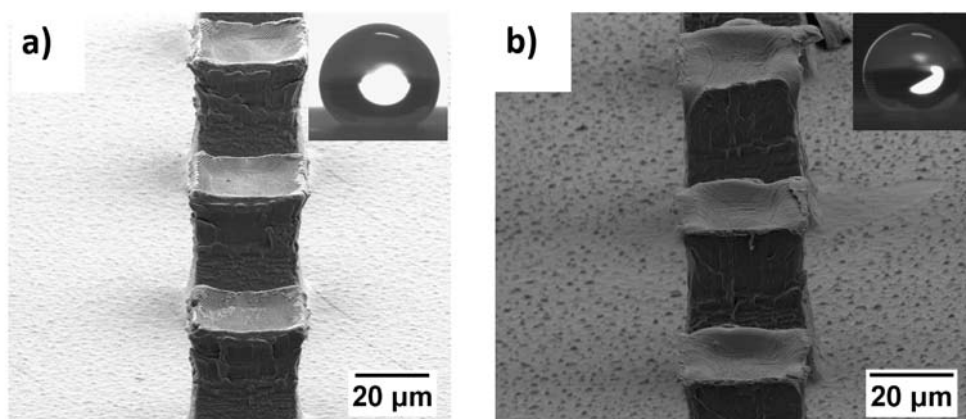


**Figure 6.23:** SEM images of the injection molded surface made of a) PP and b) TOPAS and their corresponding contact angle images.

From SEM investigation of the molded hierarchical structures we noticed a small degree of overhanging, which caused stretching forces in the demolding process, as it can be seen from the concave shape on the micropillars. We noticed that during the molding process the filling of the microstructures was easily achieved, while the filling of the nanostructures was not completely obtained. A mismatch of approximately  $500\text{ nm}$  is observed between the designed nanopillars and the final injection molded component.

When analysing the wetting behavior of the produced hierarchical structures, enhanced self-cleaning properties were realized. Table 6.5 summarizes the experiment

validation of our produced surfaces in terms of static and dynamic measurements for both materials. One can observe the high contact angles that represents superhydrophobicity, as well as small sliding and contact angle hysteresis values.

<i>Material</i>	<b>Contact angles (<math>^{\circ}</math>)</b>		
	<i>Static</i>	<i>Sliding</i>	<i>Hysteresis</i>
PP	$150 \pm 3$	$16 \pm 3$	$15 \pm 4$
TOPAS	$152 \pm 2$	$13 \pm 3$	$10 \pm 3$

**Table 6.5:** Static and dynamic measurements obtained from the wetting analysis of the injection molded polymers.

Although the results from the injection molding does not replicate perfectly the shape from the nickel shims, they can be considered as a proof of concept of the possibility to implement this developed technology on industrial applications.

## Chapter 7

# Results and Discussion

### 7.1 Design of Structures for Superhydrophobicity

During this thesis, several micro and nanostructures were studied and analysed in order to obtain a proper superhydrophobic behavior. The geometrical parameters arising from the *Wenzel* and *Cassie-Baxter* equations were taken into consideration. When fabricating superhydrophobic surfaces a high roughness is needed, and a small solid-liquid contact fraction has to also be achieved. Squared arrays of micropillars with both cylindrical and square shape were analysed. Different nanostructure geometries were also analysed.

#### 7.1.1 Microstructures

Surface structures with pillars are often used to fabricate a superhydrophobic surface as either a single structure or hierarchical structures [67, 75, 76, 78, 79, 100]. Therefore, pillars are a natural starting point for superhydrophobic surfaces. The geometrical design of the microstructures was carried out in function of the geometrical factors existing in the *Wenzel* ( $r$ ) and *Cassie-Baxter* ( $f_{SL}$ ) equations. The starting point was a squared array of pillars, either cylindrical (Figure 7.1a) or square shaped (Figure 7.1b).

The roughness and solid-liquid contact fraction corresponding to a square array of cylindrical pillars are defined as:

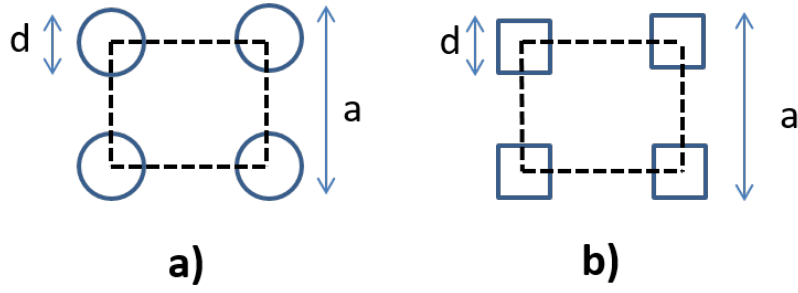


**Figure 7.1:** Schematics of a) square array of cylindrical pillars and b) square array of square pillars.

$$r = 1 + \pi \frac{dh}{a^2} \quad (7.1)$$

$$f_{SL} = \frac{\pi}{4} \left( \frac{d}{a} \right)^2 \quad (7.2)$$

where  $d$ ,  $h$  and  $a$  are the pillar diameter, height and period, respectively. The roughness and solid-liquid contact fraction corresponding to a square array of square pillars are defined as:

$$r = 1 + 4 \frac{dh}{a^2} \quad (7.3)$$

$$f_{SL} = \left( \frac{d}{a} \right)^2 \quad (7.4)$$

where  $d$ ,  $h$  and  $a$  are the pillar width, height and period, respectively. The geometrical parameters were selected in order to get a solid-liquid contact fraction of 0.09. In principle, a wide range of diameter/width and period combination could yield this value, as it is shown in Figure 7.2.

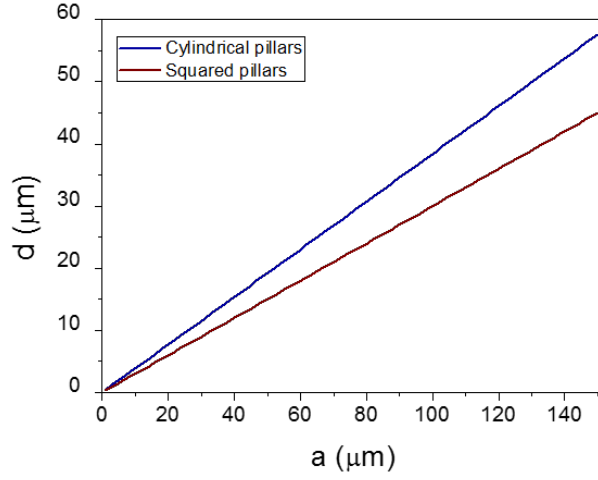


**Figure 7.2:** Plot showing the possible combinations of diameter/width and period to get a solid-liquid contact fraction of 0.09 for cylindrical and squared pillars.

During this thesis, different diameters/width were tested, as summarized in Table 7.1. However, as the size and the space between the pillars is increased, the Cassie State will become more unstable because of the larger meniscus penetration. Therefore, it would be easier for the droplet to move into the Wenzel State. For this reason, 40  $\mu\text{m}$  width/diameter and 40  $\mu\text{m}$  height were selected for this thesis, as depicted in Figure 7.3. This selected height structure yielded a roughness value of 1.48.

Surface Structure	Diameter/Width ( $\mu\text{m}$ )	Pitch ( $\mu\text{m}$ )	Height ( $\mu\text{m}$ )
<i>Cylinders</i>	40	115	40
	60	170	40
	80	230	40
	100	285	40
<i>Squares</i>	40	115	40
	80	235	40
	100	285	40

**Table 7.1:** Geometrical parameters for all the microstructures analyzed in this thesis

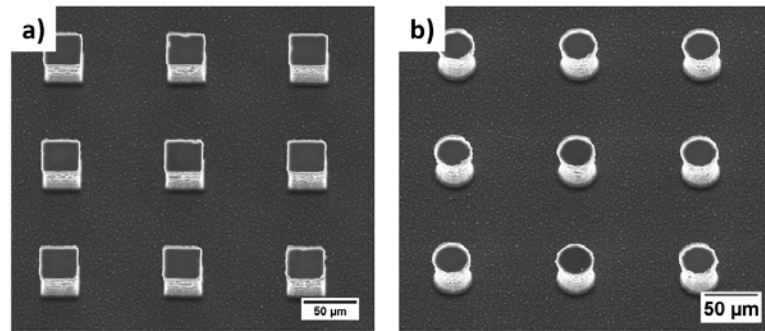


**Figure 7.3:** Tilted view SEM images of the microstructures selected in this work. a) Squared pillars, b) Cylindrical pillars.

### 7.1.2 Nanostructures

The addition of nanostructures to the microstructures has two functions: to increase the surface roughness and to decrease the solid-liquid contact fraction ( $f_{SL}$ ). The solid-liquid contact fraction for hierarchical structures is calculated by multiplying the contribution from the microstructures and from the nanostructures. Different structures were tested throughout this thesis, including honeycomb structures (Figure 7.4a,b), nanopillars structures (Figure 7.4c) and nanospikes structures (Figure 7.4d).



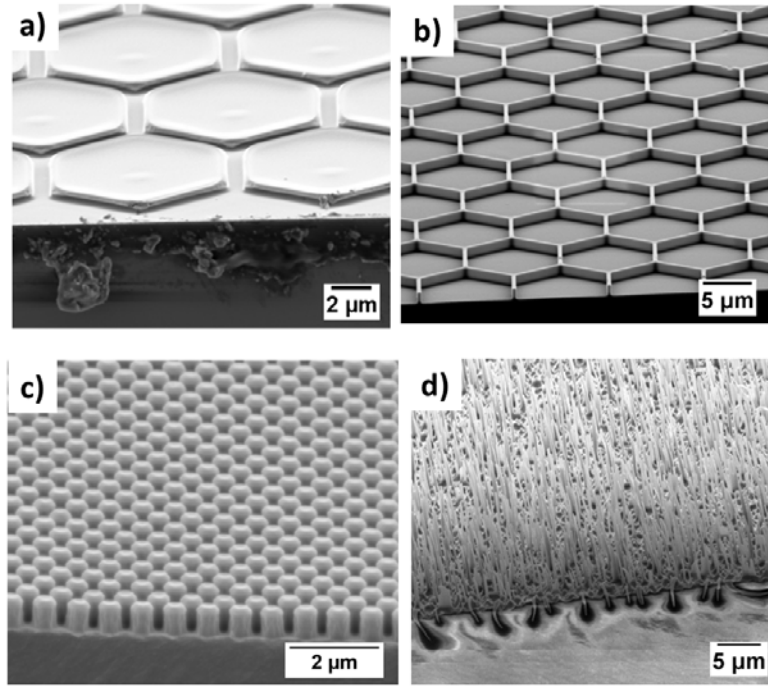


**Figure 7.4:** Tilted view SEM images of squared micropillars with several nanostructures on the top surface, a) the honeycomb pillar structures, b) honeycomb line structures, c) nanopillars and d) nanospikes.

The roughness factor and the solid-liquid contact factor for the honeycomb structures are given by the following equations:

$$r_{\text{honeycomb}} = 1 + \frac{4\sqrt{3}h \left( a - \frac{d}{\sqrt{3}} \right)}{a^2} \quad (7.5)$$

$$f_{SL-\text{Honeycombpillars}} = 1 - \left( \frac{d}{a\sqrt{3}} \right)^3 \quad (7.6)$$

$$f_{SL-\text{Honeycomblines}} = 1 - \frac{\left( a - \frac{d}{\sqrt{3}} \right)^2}{a^2} \quad (7.7)$$

where  $a$  is the width of the hexagon,  $d$  is the thickness and  $h$  is the height. Taking  $a=5 \mu\text{m}$ ,  $d=500 \text{ nm}$  and  $h=800 \text{ nm}$ , the obtained roughness factor is calculated to be the same for both polarities, 2.04. However, the solid-liquid contact fraction is different in each case: the honeycomb pillar structures have a solid-liquid contact fraction of 0.88 compared to 0.12 obtained for the honeycomb lines.

In the case of the hexagonal array of nano pillars, the roughness factor and the solid-liquid contact fraction are given by the following equations:

$$r_{nanopillars} = 1 + \frac{2\pi dh}{\sqrt{3}a^2} \quad (7.8)$$

$$f_{SL-nanopillars} = \frac{\pi}{2\sqrt{3}} \left(\frac{d}{a}\right)^2 \quad (7.9)$$

where  $d$  is the diameter of the pillar,  $a$  is the pitch and  $h$  the height of the pillars. Taking  $d=500$  nm,  $a=750$  nm and  $h=700$  nm, the obtained roughness factor is 3.25 and solid-liquid contact fraction is 0.40. In the case of the nanopikes, due to the random distribution of the structures, it was not possible to calculate the roughness factor and the solid-liquid contact fraction. A summary of the relevant geometrical parameters of the structures used in this thesis are depicted in Table 7.2. As it can be observed, the lower the solid-liquid contact fraction, the lower the roughness. So, when designing superhydrophobic surfaces, a compromise needs to be found between the roughness and the solid-liquid contact fraction.

<b>Geometrical parameters</b>					
<i>Surface Structure</i>	<i>Width</i>	<i>Pitch</i>	<i>Height</i>	<i>r</i>	<i>f</i>
Squared pillars	40 $\mu\text{m}$	115 $\mu\text{m}$	40 $\mu\text{m}$	1.50	0.09
Cylindrical pillars	40 $\mu\text{m}$	115 $\mu\text{m}$	40 $\mu\text{m}$	1.48	0.09
Honeycomb pillars	5 $\mu\text{m}$	500 nm	800 nm	2.04	0.88
Honeycomb lines	5 $\mu\text{m}$	500 nm	800 nm	2.04	0.12
Nano pillars	500 nm	750 nm	700 nm	3.25	0.40
Nano spikes	200-600 nm	Random	1-3 $\mu\text{m}$		

**Table 7.2:** Dimensions, surface roughness ( $r$ ) and solid-liquid contact fraction ( $f$ ) of the different structures used in this work.

### 7.1.3 Structures Fabrication

The silicon masters used in this thesis were fabricated with different lithographic techniques, depending on the selected dimensions. The masters were fabricated on different partners facilities, including the National Center of Scientific Research ‘Demokritos’ (Greece), NIL Technology ApS (Denmark) and IK4-Tekniker (Spain). A summary on the fabrication procedures used to fabricate the masters is listed below:

- *Microstructures*: due to the size of these structures, a UV photolithography process was used to produce these structures. Subsequently, a DRIE process was realized in order to produce the 40  $\mu\text{m}$  height structures.
- *Honeycomb structures*: both polarities of these structures were fabricated by electron beam lithography with a subsequent etching process.
- *Nanopillars*: these structures were fabricated using a deep UV-photolithography equipment with a subsequent etching process.
- *Black Silicon*: black silicon is random cone and/or needle shaped nanostructures etched in a silicon wafer. The fabrication of black silicon is maskless and uses selective etching parameters to produce high roughness silicon surfaces.

## 7.2 Self-cleaning Surfaces

As it was already extensively discussed in Chapter 2, surfaces with self-cleaning properties are in the Cassie-Baxter state. The contact angle of the structured surface is strongly dependent of this solid-liquid contact fraction [35, 64, 156]. For a hierarchical structure, the solid-liquid contact fraction is calculated by multiplying the area fraction of the two structures [67]:

$$f = f_{micro} * f_{nano} \quad (7.10)$$

The solid-liquid contact fraction of a hierarchical structure is then found to be much smaller than the one with only one level of structures, thus leading to the improvement of the superhydrophobicity and the self-cleaning effect of the surface.

In this section we present the fabrication of a multiscale surface with excellent self-cleaning behavior. Different nanostructures and microstructures that exhibit hydrophobicity in the Wenzel state are combined in order to obtain stable Cassie-Baxter surfaces with strong superhydrophobicity and self-cleaning properties. Based on the theory presented in the Section 7.1, we are able to predict or adjust the wettability of a solid surface with known material properties and geometrical values.

The surfaces fabricated with the inking mode method developed in Section 6.2.2 were used as masters to produce well defined 3D PDMS molds. These molds were used to imprint the designed 3D hierarchical surfaces over inherently hydrophobic material and over different substrates, allowing us to produce several superhydrophobic surfaces with the same PDMS mold by one-step process. Figure 7.5 depicts the experimental procedure followed to produce the hierarchical superhydrophobic surfaces. A PDMS soft mold was created from the surfaces fabricated with the inking mode (Figure 7.5b). The PDMS mold was used to imprint the structures by UV-NIL in XNIL26 UV-curable resist (Figure 7.5c-e). The final hierarchical structures were produced both on silicon and on PET substrates, thus demonstrating the feasibility of the developed technique.

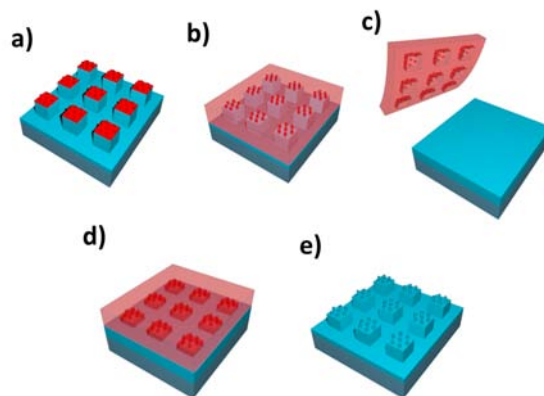


**Figure 7.5:** Schematic description of the fabrication of 3D hierarchical surfaces. a) The starting point are the inking mode fabricated samples, as described in Section 6.2.2, b) a PDMS stamp was fabricated to have a final mold with the 3D structures, c,d,e,) the PDMS was used to make the final imprints over different substrates.

Four different nanostructured patterns were used to create the hierarchical structures, a honeycomb-like structure in both polarities (pillar and line configuration), a hexagonal array of nano pillars and a random distribution of nano spikes. One microstructured pattern was used for this study, a square array of square pillars. In order to characterize individual contributions from the microstructures and the nanostructures, the wettability of both the 2D structures and the 3D hierarchical structures was carefully studied.

### 7.2.1 Wetting of 2D Surfaces

Figure 7.6 shows top view SEM images of the XNIL 26 micropattern selected for the fabrication of the superhydrophobic structures and its corresponding water contact angle value ( $145^\circ$ ).

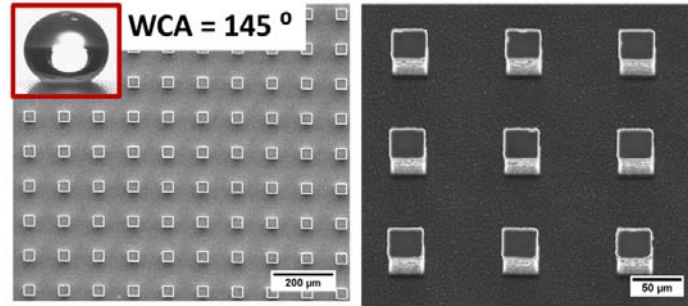


**Figure 7.6:** Top view SEM images of the micropattern used to design the hierarchical structures and its corresponding water contact angle value.

The width, pitch and height of the squared micropillars were tailored in order to minimize the contact area between the water and the solid surface. The surface wettability was investigated by measuring the WCA, the sliding angle and the hysteresis angle. Applying the values obtained in Section 7.1, the theoretical contact angle values for the Wenzel and the Cassie-Baxter model can be obtained and compared with the experimental obtained values. Table 7.3 presents the theoretical and experimental values of the WCA for the micropattern and for the flat XNIL26 surface.

Surface Structure	Water contact angles [ $^{\circ}$ ]				
	<i>Theoretical</i>		<i>Experimental</i>		
	Wenzel	Cassie - Baxter	Static	Sliding	Hysteresis
Flat XNIL 26			$100 \pm 3$	$60 \pm 6$	$25 \pm 5$
Squared Microstructures	111	155	$145 \pm 4$	$35 \pm 5$	$16 \pm 6$

**Table 7.3:** Calculated and experimental contact angles measurements of the micropattern on XNIL26 surface.

An increment in the water CA value of the micropattern, as well as a decrease of the sliding angle was observed. However, the experimental results indicate that a superhydrophobic surface is not obtained only with an array of microstructures. Furthermore, the experimental WCA value is lower than the theoretical Cassie-Baxter, indicating the existence of a mixed state, introduced by Marmur [41], where the droplet partially wets the surface and partially sits on air pockets. The Cassie-Baxter equation is modified for this state as follows:

$$\cos\theta = R_f f_{SL} \cos\theta_0 - 1 + f_{SL} \quad (7.11)$$

where  $R_f$  is the roughness of the portion of the solid that touches the liquid. This mixed state is generally accepted as a transitional state between Wenzel's and Cassie's states [57], as it is observed in the sliding and hysteresis angles measurements ( $35^\circ$  for the sliding angle and  $16^\circ$  for the hysteresis). To consider a surface as superhydrophobic with self-cleaning behavior, a sliding angle below  $15^\circ$  and a hysteresis angle below  $10^\circ$  are generally needed. The angles present on the microstructures are too large to consider them suitable for self-cleaning purposes.

Figure 7.7 shows the tiled view SEM images of the nanostructures selected to create the hierarchical structures and their corresponding water contact angle images.

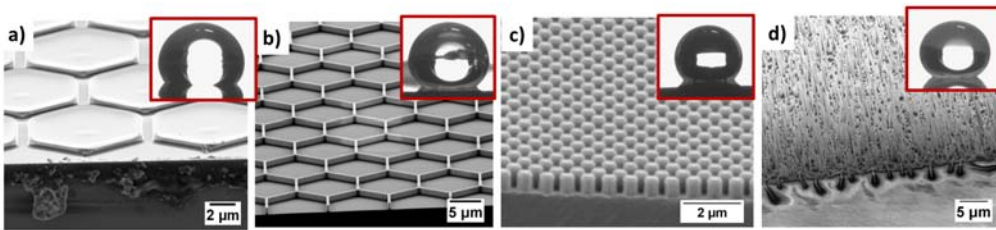


**Figure 7.7:** Tilted view SEM images of the nanostructures selected for the fabrication of the hierarchical structures and their static water contact angles. a) Honeycomb pillars, b) honeycomb lines, c) nano pillars, d) nano spikes.

The theoretical and experimental values obtained for the nanostructures are depicted in Table 7.4. All the nanostructures are in the *Wenzel* state, as it can be observed both in the good agreement with the calculated contact angles given by the Wenzel equation and with the values of the sliding and hysteresis angles. The

droplets were completely pinned to the surface, evidencing the complete wetting of the nanostructures by the water droplets. Droplets in the Wenzel state are not suitable for superhydrophobic properties, since they cannot roll-off from the surfaces. This is a common trend observed on surfaces fabricated only with nanostructures, since the low height of the structures leads to a easier water penetration of the meniscus.

Surface Structure	Water contact angles [ $^{\circ}$ ]				
	<i>Theoretical</i>		<i>Experimental</i>		
	Wenzel	Cassie - Baxter	Static	Sliding	Hysteresis
Honeycomb pillars	120	110	$118 \pm 5$	Pinned	$30 \pm 4$
Honeycomb lines	120	155	$123 \pm 9$	Pinned	$21 \pm 10$
Nano pillars	144	134	$143 \pm 2$	Pinned	$23 \pm 4$
Nano spikes			$146 \pm 3$	Pinned	$45 \pm 5$

**Table 7.4:** Calculated and experimental contact angles measurements of the nanostructures on XNIL26 printed surfaces.

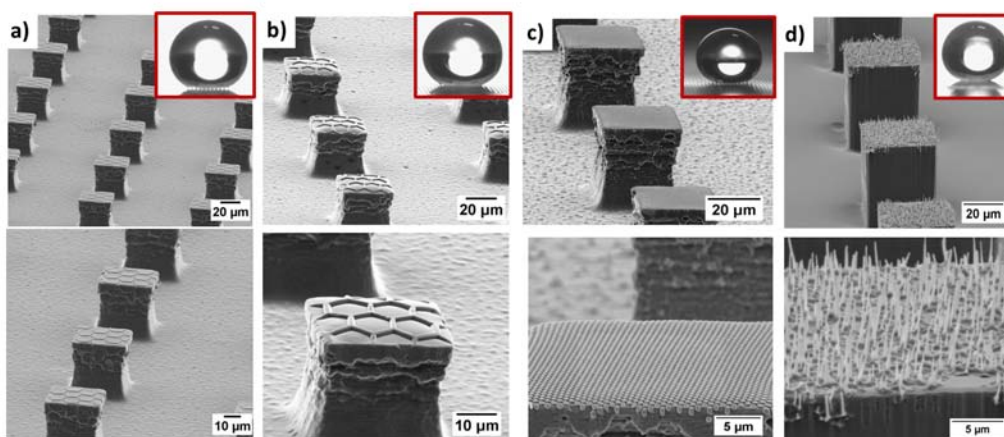
While for the microstructures, only partial penetration occurs; for the nanostructures a complete water penetration is observed. The results coming from the 2D structures evidences that one single level of structures may be insufficient to create a robust self-cleaning. A hierarchical surface is needed to overcome the de-stabilization factors arising from single level structures.



### 7.2.2 Wetting of 3D Hierarchical Surfaces

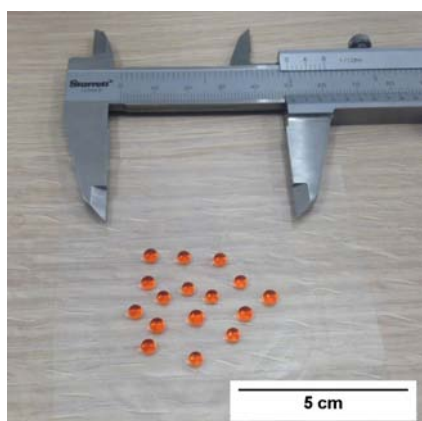
The objective of achieving superhydrophobic surfaces with self-cleaning properties could not be achieved only with one level structures. Using the RNIL technique developed in Section 6.2.2, 3D hierarchical surfaces were constructed over relatively large areas ( $5 \text{ cm}^2$ ). Combining the micro and nanostructures discussed in the previous Section, four different hierarchical structures were realized in the intrinsic hydrophobic resist XNIL26 SF.

Figure 7.8 illustrates the tilted view SEM images of honeycomb pillars (Figure 7.8a), honeycomb lines (Figure 7.8b), nano pillars (Figure 7.8c) and nano spikes (Figure 7.8d) structures printed on the micropillars, showing the corresponding WCA images in the insets. The fabrication technique was demonstrated using silicon and flexible transparent PET as substrates, obtaining exactly the same wetting results, which evidences the flexibility and adaptability of the developed imprinting technique.



**Figure 7.8:** Tilted view SEM images of squared micropillars with several nanostructures on the top surface, a) the honeycomb pillar structure, b) honeycomb line structure, c) nanopillars and d) nanospikes.

Furthermore, the technique was demonstrated on areas up to  $5 \cdot 5 \text{ cm}^2$  areas, as shown in Figure 7.9, thus opening the window towards large area superhydrophobic surface.



**Figure 7.9:** Photograph of the micro/nano hierarchical structure fabricated on a PET substrate over an area of  $5 \times 5 \text{ cm}^2$  with several water droplets resting on the patterned area.

Theoretical and experimental water angle values, as well as sliding and contact angle hysteresis values, are depicted in Table 7.5. As discussed above, the corresponding solid-liquid contact fraction will be the result of multiplying the contributions from the microstructures and from the nanostructures. The surface roughness obtained for multiscale structures will be the sum of the two contributions [67].

Surface Structure	Water contact angles [ $^{\circ}$ ]				
	<i>Theoretical</i>		<i>Experimental</i>		
	Wenzel	Cassie - Baxter	Static	Sliding	Hysteresis
Honeycomb pillars on Micropillars	138	157	$156 \pm 3$	$18 \pm 3$	$12 \pm 3$
Honeycomb lines on Micropillars	138	171	$159 \pm 5$	$17 \pm 2$	$10 \pm 3$
Nano pillars on Micropillars	180	164	$165 \pm 1$	$11 \pm 4$	$7 \pm 2$
Nano spikes on Micropillars			$170 \pm 2$	$7 \pm 2$	$4 \pm 2$

**Table 7.5:** Calculated and experimental measured contact angles of the hierarchical structures fabricated on XNIL 26 printed surfaces.

The measured WCA values on all the samples are larger than  $150^\circ$ , clearly indicating superhydrophobic properties. The honeycomb pillars-on-micropillars, nanopillars-on-micropillars and the nanospikes-on-micropillars structures exhibit a clear Cassie-Baxter state, as it can be observed comparing the calculated Cassie-Baxter and the measured contact angle values. In the case of the honeycomb lines-on-micropillars, the experimental value is lower than the expected for the Cassie-Baxter model. This is probably due to some defects after the fabrication process that provokes that the water partially wet the cavities. As it can be observed in Figure 7.8b, the top of the structures are not fully planar due to the residual layer formed the reverse imprint process. This may be the reason for the partial wettability of these structures.

The wetting behavior of a structured surface cannot be measured with one single parameter, such as the water contact angle value. The adhesion of the droplet to the surface is a key parameter to take into account in the development of self-cleaning surfaces. For this reason, the sliding angle and hysteresis were measured. The sliding contact angle and the hysteresis reach the minimum value for the nanopillars-on-micropillars and the nanospikes-on-micropillars configurations. The contact angle hysteresis is below  $10^\circ$ , which is generally accepted as value to consider a superhydrophobic surface as a self-cleaning surface [4]. The hierarchical structure with the nanospikes-on-micropillars yielded the largest contact angle value of  $170^\circ$  and the smallest hysteresis at  $4^\circ$ . The effect of the hierarchy is evident, showing both large static contact angles and small dynamic contact angle in comparison to the single level structures.

By plotting the theoretical Cassie-Baxter curve obtained for the resist XNIL26 we can observe the expected WCA value for surfaces with different solid-liquid contact fraction values. In Figure 7.10 this theoretical curve can be observed. The obtained WCA values from the four different fabricated surfaces are superimposed to the theoretical curve, allowing us to deduce the real solid-liquid contact fraction values for the different surfaces.

The surface with a honeycomb pillars-on-micropillar structure has a WCA of  $156^\circ$ , corresponding to a value of  $f = 0.10$ . The surface with a honeycomb

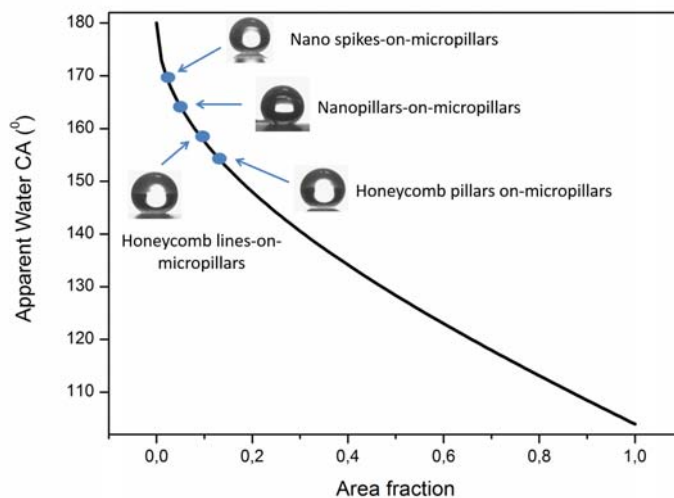


**Figure 7.10:** Measured contact angles of the hierarchical surfaces compared to the theoretical Cassie-Baxter state curve. Snapshots of water droplets contacting the samples are shown as insets.

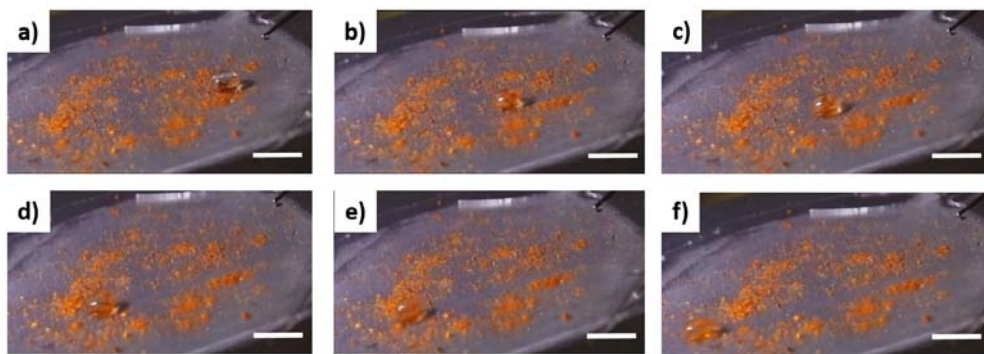
lines-on-micropillar structure has a WCA of  $159^\circ$ , corresponding to a value of  $f=0.05$ . However, the calculated  $f$  value for these structures is  $f = 0.02$ . In this case, the calculated  $f$  factor is not in agreement with the experimental obtained value. This is probably due to a mixed state described before; where the water is partially wetting the pattern, increasing slightly the real solid-liquid contact fraction. For the case of the nanopillars-on-micropillars configuration, the WCA value is  $166^\circ$ , with a corresponding  $f = 0.04$ , which agrees with the theory. Due to the random distribution of the nanospikes it was not possible to calculate a value for the solid-liquid contact fraction. Nevertheless, with a contact angle value of  $170^\circ$  a solid-liquid contact fraction of  $f = 0.02$  is deduced.

### 7.2.3 Dynamic effects

Based on the excellent superhydrophobicity obtained, the robustness of the hierarchical surfaces was evaluated by dynamic measurements. Dynamic effects on a superhydrophobic surface, such as impingement [52, 157] are of great importance to probe energy barriers responsible for wetting transitions. A superhydrophobic surface that could be used in real life applications needs to exhibit a good robustness over impinging droplets, such as rain droplets. Furthermore, if the surface needs to

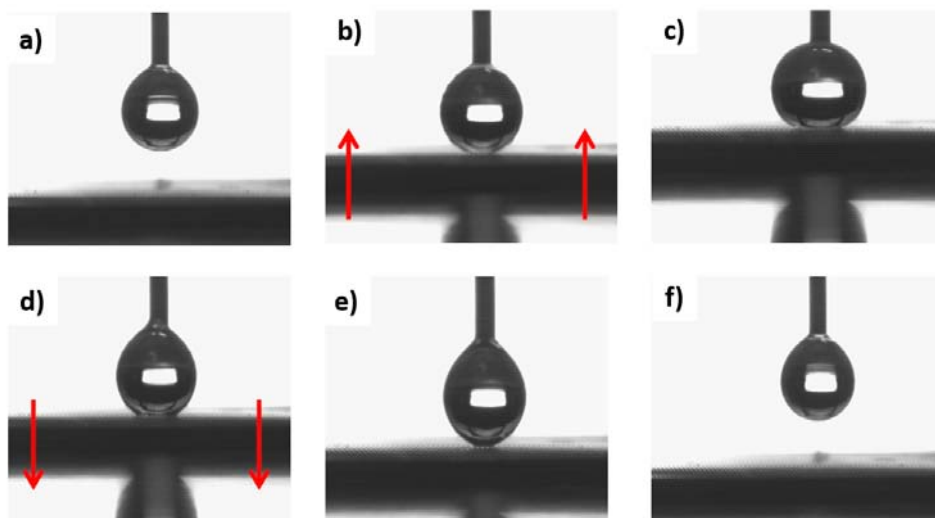
be self-cleaning, a good roll-off behavior in order to remove the contaminants. In this section we analyse the self-cleaning performance, as well as the behavior over impacting droplets of our fabricated hierarchical superhydrophobic surfaces.

Figure 7.11 shows a sequence of images of the hierarchical patterned nanopikes-on-micropillars demonstrating self-cleaning effect of a powder contaminant from the surface, as the water droplet rolls off from a slightly tilted surface ( $10^\circ$ ). It is observed how the droplet starts to roll-off from the releasing point of the surface. As the water droplet advances towards the surface, the contaminants are trapped by the droplet, giving rise to a self-cleaning effect of the surface.



**Figure 7.11:** Self-cleaning of the superhydrophobic surface with hierarchical nanopikes-on-micropillars on PET: a) image of the superhydrophobic surface covered with pepper powder as contaminant, b-f) series of images showing a droplet rolling along the surface taking all the contaminants with it. (The scale bars correspond to 1 cm).

The low adhesion between the water droplets and the fabricated hierarchical surfaces is evidenced in Figure 7.12. It shows a set of images where the water droplet is approached and separated from the surface.



**Figure 7.12:** Sequence showing the low adhesion between a water droplet and the superhydrophobic surface, indicating a small contact angle hysteresis: a) The water droplet is suspended from a needle. b) Approaching of the substrate towards the droplet. c) The droplet undergoes a sliding movement due to the low adhesion between them. d, e) Retracting the substrate from the droplet. f) The droplet remains attached to the needle without wetting the surface.

Firstly, a water droplet was suspended from a metallic needle (Figure 7.12a) and then was brought in contact with the surface by moving up the patterned surface (Figure 7.12b). The droplet does not wet the surface since the air is still trapped under the water droplet (Figure 7.12c). We observed that the shape of the droplet does not deform significantly, which is a clear impact of the non-wetting properties of the micro/nano patterned substrate. As the substrate starts to retract the droplet begins to deform (Figure 7.12d, e) and, after complete separation the droplet remains attached to the needle (Figure 7.12f). This sequence indicates that there is a poor adhesion between the droplet and the hierarchical surface.

To finish the dynamic analysis of our surfaces, experiment on impacting droplets were performed. Using 10  $\mu\text{l}$  droplets and a high speed camera (1200 frames per second) we analyse the behavior of impacting droplet over the 2D squared micropillars surfaces and over the 3D hierarchical surfaces. A comparison on the behavior of water droplets on the two different surfaces is depicted in Figure 7.13 and Figure 7.14.

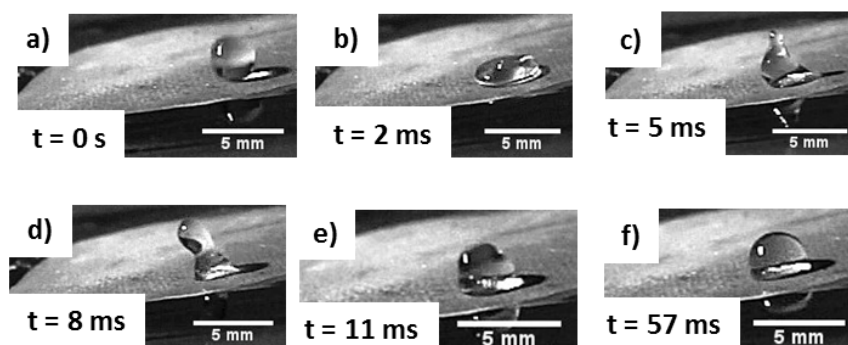


**Figure 7.13:** Sequence of a 10  $\mu\text{l}$  droplet impacting on the squared micropillars array. The snapshots are obtained using a high-speed camera. The sequence shows a) approach of the droplet, b) hitting the surface, c,d) recoil and e,f) penetration into the cavities of the microstructures, ending in a Wenzel state.

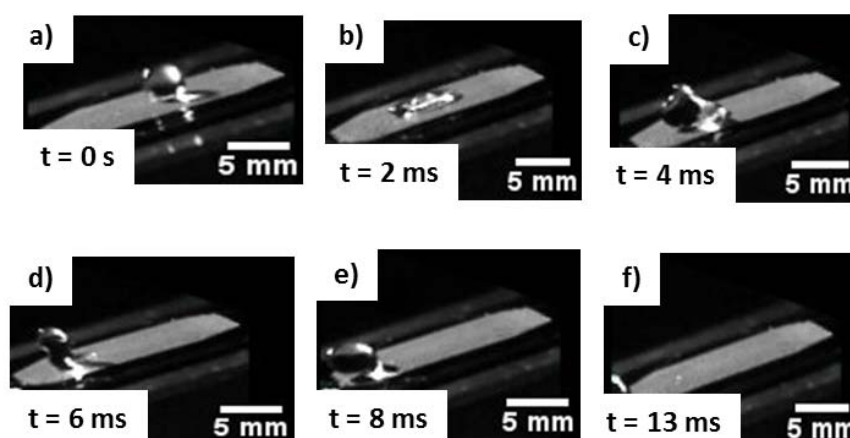


**Figure 7.14:** Sequence of a 10  $\mu\text{l}$  droplet impacting on the nanospikes-on-micropillars array. The snapshots are obtained using a high-speed camera. The sequence shows a) approach of the droplet, b) hitting the surface, c,d) recoil of the droplet and e,f) roll-off of the droplet along the surface.

Figure 7.13 shows the process of a droplet impinging on the 2D micropillars array, impacting with a velocity of 0.94 m/s on a slightly tilted ( $10^\circ$ ) surface. The droplet hits the surface and it is deformed after 2 ms (Figure 7.13b). The droplet recoils in approximately 5 ms (Figure 7.13c,d). After recoiling, the droplet remains on the surface (Figure 7.13e,f), in a clear Wenzel state, indicating the penetration of the droplet on the cavities of the microstructures.

Figure 7.14 shows the process of a droplet impinging on the

nanospikes-on-micropillars array, impacting with a velocity of 0.94 m/s. The droplet hits the surface and it is deformed after 2 ms (Figure 7.14b). The droplet recoils in 3 ms (Figure 7.14c,d). After recoiling, the droplet bounce-off from the surface, leaving no residual water (Figure 7.14e,f).

This difference on the impacting behavior between the 2D and the 3D fabricated surfaces evidences the robustness of the hierarchical surfaces in comparison with one single level of structures.

#### 7.2.4 Summary

We present a simple and robust manufacturing method to produce well-defined hierarchical micro/nano structures over  $cm^2$  areas. The usefulness of this approach allows the design and production of superhydrophobic surfaces in a reproducible manner. We compared different combination of hierarchical micro nanostructures and examined their self-cleaning properties. An increment of a 70% of the static WCA compared to the unpatented surface was achieved, while a hysteresis of  $4^\circ$  and a sliding angle of  $7^\circ$  were realized.

To the best of our knowledge, this is the largest static contact angle obtained on a patterned surface without the need of low surface energy coatings. Furthermore, since the hierarchical patterns were demonstrated over  $5 \times 5 cm^2$  areas on flexible PET, these results open the path to a high volume superhydrophobic surfaces.

The robustness of the superhydrophobicity as well as the self-cleaning performance were analysed by dynamic measurements. The surfaces exhibited and excellent self-cleaning behavior, removing all the contaminants when the droplets rolled off from the surface. The improvement of the 3D hierarchical surfaces in comparison with the 2D micropillars was evidenced by experiments of impacting droplets. The impacting of droplet on the 2D surfaces leads to a penetration of the water droplet in the cavities, while for the case of the 3D structures the droplets bounce off from the surface, thus avoiding the wetting of the surfaces.



### 7.3 Design of hierarchical surfaces for tuning wetting characteristics

In this section, we describe the fabrication of hybrid hierarchical patterned surfaces with tuneable wetting properties. We demonstrate that a hierarchical surface fabricated with a combination of two different materials exhibit both 'lotus' and 'petal' effect by varying the deposition conditions of the water droplets, without the need of any modification on the surface. The great difference between the capillary pressures exerted by the microstructures and by the nanostructures was the key factor that allowed us to effectively tailor the adhesion of the water droplets. By having a low capillary pressure for the microstructures and a high capillary pressure for the nanostructures, we engineer the surface properties in a controlled way, having the possibility of being in a 'lotus' state or in a 'petal' state.

Superhydrophobic 'lotus' surfaces that exhibit high water contact angle ( $CA, > 150^\circ$ ) and low water adhesion ( $CAH, < 10^\circ$ ), can be used as self-cleaning [12, 158] or anti-bacterial interfaces [159]. In this case, through the combination of a larger microstructure in the range from 10 to 50  $\mu\text{m}$  and a smaller structure in the range from 200 nm to 2  $\mu\text{m}$ , the leaves of the lotus plant exhibit high water contact angle (WCA) and low water sliding angle (WSA) that produces the self-cleaning effect of this plant. These water droplets do not penetrate in the interstitial structures (Cassie-Cassie's state), thus producing an easily roll off. These are the most common and fabricated structures by the researchers.

In contrast, adhesive superhydrophobic 'petal' surfaces that exhibit high water contact angle ( $CA > 150^\circ$ ) and can pin water droplets can be useful for transporting small volumes of aqueous solution without loss of liquid [8, 20], for localized chemical reactions or microfluidic lab-on-a-chip devices [59]. These plants exhibit a larger micropapillae in the range from 15-20  $\mu\text{m}$  and smaller nanofolds in the range from 700 to 900 nm. This configuration allows the water droplets to impregnate the microstructure formed by the large micropapillae, but not the nanofolds, leading to a surface with high WSA and high adhesive force to water (Wenzel-Cassie's state). The droplets do not roll off even if the petal is turned upside down.

Superhydrophobic surfaces with controlled adhesion force have been demonstrated on polystyrene [21], polypropylene (PP) [160], poly(dimethyl siloxane) (PDMS) [161], carbon nanotubes [162], epoxy resin [163] and so on [164–168]. However, the controlled adhesion force on these structures is based on tuneable surface morphology or surface chemistry in the respective surfaces. The ability to address the adhesive properties (i.e. high or low adhesion) on the same surface with any additional chemical or topographical modification has not been reported yet [164].

The same experimental procedure that was followed in Section 6.2.2 was implemented to achieve our hierarchical hybrid surfaces. By changing the imprint conditions, two different imprinting modes could be achieved, as formerly discussed, the ‘inking’ mode and the ‘intact’ mode. In the ‘inking’ mode the nanostructures were transferred only to the elevated parts of the microstructures, whereas in the ‘intact’ mode the nanostructures are transferred to the complete area of the pre-patterned surface.

This section makes a comparative study of the dynamic behavior when a water droplet is dropped on one of these surface configurations. The samples fabricated with the ‘intact’ mode exhibit a unique dynamic behavior, with intermediate wetting states which depend on the water droplet deposition conditions.

In this work, only the nano pillars and the nano spikes were selected to perform the imprints. The microstructures consisted on a square array of cylindrical pillars; the geometrical parameters, as well as the roughness and the solid-liquid contact fraction of these structures were already presented in Table 7.1.

This section will present the obtained results, both from the morphology, wettability and dynamic behavior point of view. The typical wetting analysis realized for superhydrophobic surfaces will be presented. A careful dynamic analysis will be carried out for the samples fabricated with the ‘intact’ mode. Furthermore, a model will be proposed to explain the obtained results.

### 7.3.1 Morphology control and Wettability

To make a comparative study, the two different fabrication modes were used to fabricate the two different types of structures. Figure 7.15 shows SEM images of the fabricated samples. The ‘intact’ mode (Figure 7.15a,b) corresponds to a high pressure imprint, obtaining transfer of the nanostructures both on the top and on the bottom of the micro array. The ‘inking’ mode (Figure 7.15c,d) corresponds to a low pressure imprint, obtaining transfer of the structures only on the elevated parts of the micro array. Table 7.6 shows the static and dynamic contact angle measurements and their standard deviation on the different fabricated surfaces.

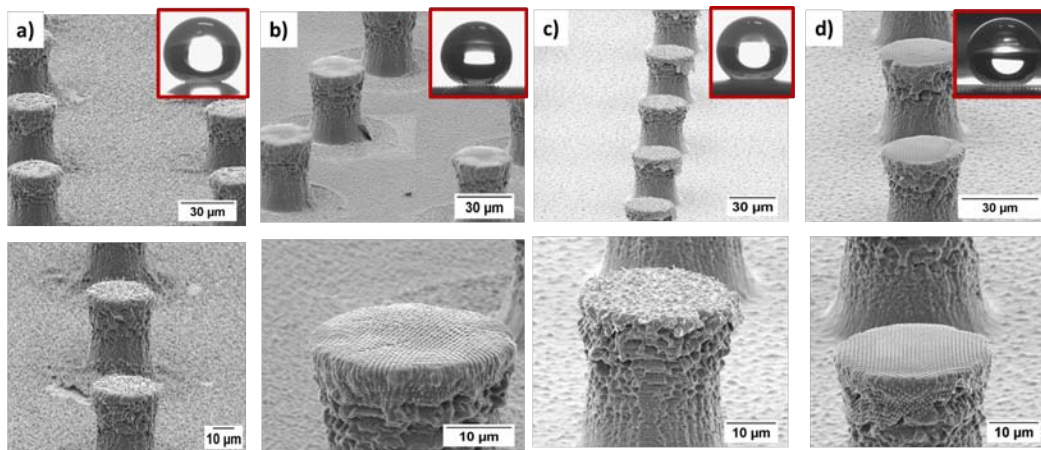


**Figure 7.15:** Tilted view SEM images of cylindrical micropillars decorated with nanostructures in two different modes: a) intact mode of the nanospikes on micropillars, b) intact mode of the nanopillars on micropillars, c) inking mode of the nanospikes on micropillars and d) inking mode of the nanopillars on micropillars. The insets correspond to their WCA images.

<i>Surface structure</i>	<b>Water contact angles [°]</b>		
	<i>Static</i>	<i>Sliding</i>	<i>Hysteresis</i>
Intact mode (Nanospikes - Micropillars)	167 ± 3	7 ± 3	6 ± 3
Inking mode (Nanospikes - Micropillars)	162 ± 4	10 ± 3	9 ± 4
Intact mode (Nanopillars - Micropillars)	168 ± 2	6 ± 2	4 ± 2
Inking mode (Nanopillars - Micropillars)	168 ± 2	9 ± 3	10 ± 5

**Table 7.6:** Experimental contact angles measurements for the hierarchical structures fabricated with PMMA/Ormocomp.

The measured WCA values on all the samples are larger than  $150^{\circ}$ , clearly indicating superhydrophobic properties. The surfaces exhibit a clear 'lotus' state, as it can be observed on the sliding angle and contact angle hysteresis measurements, indicating low adhesion between the droplet and the surfaces. All the fabricated samples exhibit contact angle values above  $160^{\circ}$ , overcoming the threshold values for superhydrophobicity. Sliding angles as low as  $6^{\circ}$  and contact angle hysteresis values as low as  $4^{\circ}$  were found on the surfaces fabricated with the 'intact' mode. Interestingly, the wettability analysis of the surfaces exhibit similar in the two different surface configurations. This is because when a droplet is in the 'lotus' state, is resting only on the elevated parts of the surface, and the pattern below the elevated parts does not influence the measurements. However, when dynamic effects are analysed, the behavior changes dramatically, and the effect of having nanostructures on the bottom of the array becomes very important to have an effective control of the adhesiveness over the superhydrophobic surface.

### 7.3.2 Dynamic behavior

Dynamic effects on a superhydrophobic surface, such as impingement [52, 157] or vibration [51, 169] have a great interest in probing energy barriers responsible of wetting transitions. Usually, these transitions are directly from a composite to homogeneous state (i.e. Cassie to Wenzel transition) [39, 170]. In this regard, hierarchical surfaces open the pathway from intermediate transitions, which can be useful if one can get a precise control over them. In this section, an intermediate state from pure Cassie to pure Wenzel transition is demonstrated. This intermediate transition corresponds to the so-called 'petal' effect, where the water is penetrating the microstructures, but not the nanostructures, leading to a high contact angle and a high adhesion force.

Droplet impact and rebound characteristics on superhydrophobic surfaces are governed primarily by the impact velocity and inherent liquid properties, such as density, viscosity and surface tension [171]. When a droplet impinges on a superhydrophobic surface, it deforms and stores kinetic energy, which makes it recoil. The shape and extent of the deformation are balanced by the surface tension and its velocity and can be quantified with the Weber number, which is the ratio of kinetic energy to surface energy. After impingement, the inertial energy of the water droplet is dissipated through viscous forces. This viscous resistance affects the droplet rebound characteristics and can be quantified by the Reynolds number, defined as the ratio of the inertial force to viscous force [172]. These numbers are dimensionless and can be used to characterize the impact dynamics of the water droplet toward the structured surface. The Weber number ( $We$ ) is defined as:

$$We = \frac{\rho d V^2}{\sigma} \quad (7.12)$$

where  $\rho$  is the density of the drop ( $1000 \text{ Kg/m}^3$ ),  $d$  is the diameter of the drop ( $d = 0.004 \text{ m}$ ),  $\sigma$  is the surface tension of the drop ( $0.072 \text{ J/m}^3$ ). The Reynolds number ( $Re$ ) is defined as:

$$Re = \frac{\rho d V}{\eta} \quad (7.13)$$

where  $\eta$  is the dynamic viscosity of the liquid ( $0.001Ns/m^2$ ).

The behavior of a water droplet on a superhydrophobic surfaces is governed by its impact velocity  $V$ . In our hierarchical surfaces, depending on the impact velocity, different wetting regimes were observed, characterized by the degree of penetration of the droplet on the micro and nano structures. For relatively low impact velocities, regular rebound of the droplets and air trapping were observed on all the hierarchical surfaces. For intermediate impact velocities the dynamic of the droplets was different for the two different modes of fabrication. For the surfaces which contained nanostructures only on the elevated parts of the microstructures (i.e. 'inking' mode), a pinning of the droplet with low WCA is observed, indicating penetration both on the microstructures and on the nanostructures (Wenzel state). For the surfaces which contained nanostructures on the complete are of the pre-patterned surface (i.e. 'intact' mode), pinning was also observed, but with a high contact angle, indicating 'petal' state, where the droplet is penetrating the microstructures but not the nanostructures. For high impact velocities, Wenzel droplets were observed on all the samples.

As the two dimensionless numbers are velocity dependant, one can create an impact diagram, depending on the impact velocity and the viscosity of the liquid. Figure 7.16 shows the impact diagrams for the intact mode surfaces. For the hierarchical surface fabricated with nanopillars - micropillars, the 'petal' region is present when the droplets impact with velocities from 0.81 to 1.71 m/s. At lower velocities the 'lotus' state appears while at higher velocities Wenzel state appears. For the surfaces fabricated with nanospikes - micropillars, the 'petal' region is present when the droplets impact with velocities from 0.71 to 0.98 m/s. At lower velocities 'lotus' state appears and at higher velocities Wenzel state appears.

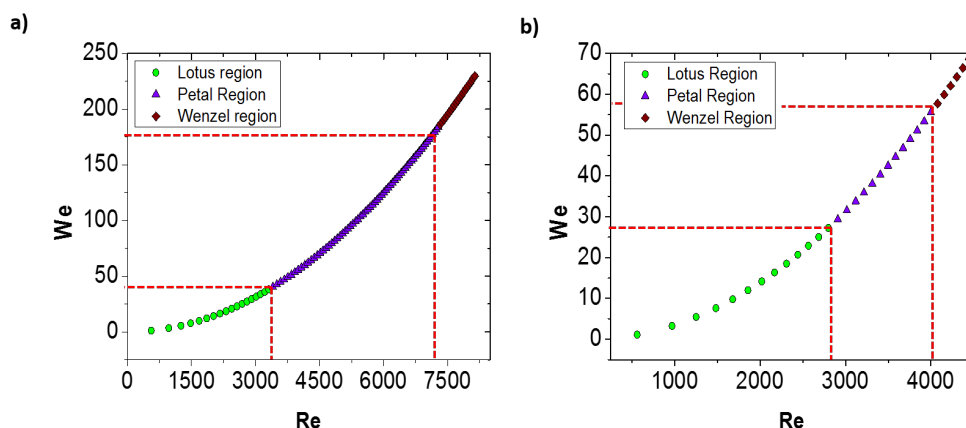


**Figure 7.16:** Graphs showing the dynamic behavior of droplet on the a) nanopillars-micropillars surface and b) nanopikes-micropillars surface.

For the samples fabricated with the inking mode a velocity of 0,80 m/s was necessary to provoke a direct Cassie to Wenzel transition. Figure 7.17 shows a schematic of all the wetting states observed on the samples fabricated with the intact mode.

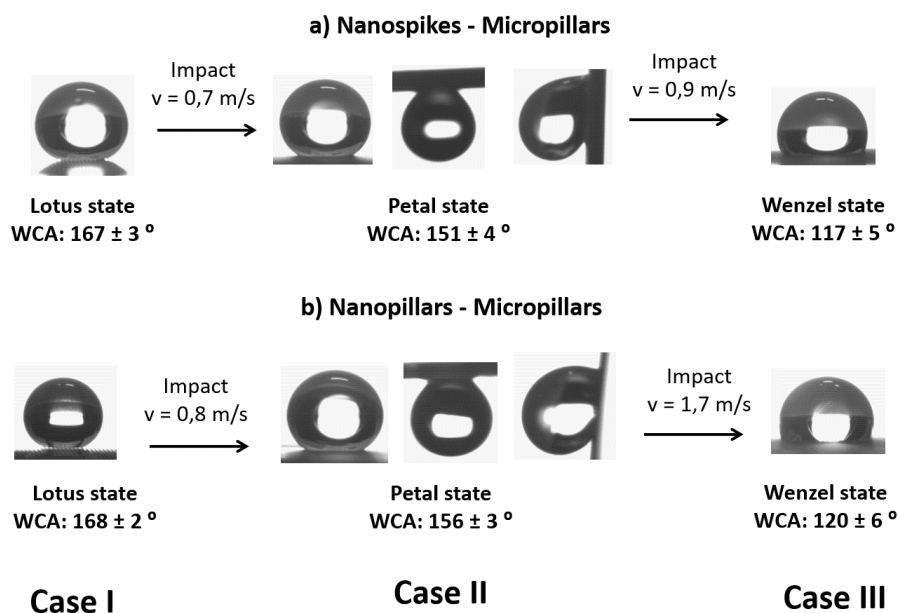


**Figure 7.17:** Schematic of the different wetting states observed on the hierarchical surfaces made with the intact mode. a) Transitions for the nanospikes - micropillars configuration and b) transitions for the nanopillars - micropillars configuration.

Three different states are clearly differentiated. For the case of the nanospikes -

micropillars surface, first the droplet rests on a ‘lotus’ state, with a CA of  $167^\circ$ , if the droplet impacts the surface at a velocity in the range between 0,7 and 0,9 m/s ( $28 < We < 47$ ,  $2169 < Re < 367$ ), the ‘petal’ state appears, with a CA of  $151^\circ$  and a high adhesion force. If the drop impacts the surface at a velocity higher than 0.9 m/s, the Wenzel state appear, with a CA of  $117^\circ$ . The same situation is observed with the nanopillars - micropillars sample, but the threshold velocities to produces the transitions to “petal” state is higher, being in the range between 0,8 and 1,7 m/s ( $36 < We < 162$ ,  $3218 < Re < 6837$ ). When the droplet impacts at a velocity higher than 1,7 m/s, Wenzel transition is observed.

The process followed to obtain the three different observed states was recorded with a high speed camera (1200 frames per second). In Figure 7.18 it can be observed different snapshots of the obtained videos. These images show how the droplet impinges on the surface and the behavior it attains. For the Case I, the droplet is impacting at 0.6 m/s. The droplet hits the surface and it is deformed after 3 ms (Case Ib). After 8 ms the droplet recoils and after 10 ms bounce off from the surface. After 34 ms the droplet impinges again the surfaces. Several rebounds later on, at 87 ms the droplet stabilizes on a ‘lotus’ state. For the Case II, the droplet is impacting with a velocity of 0.8 m/s. The droplet hits the surface and it is deformed after 2 ms (Case IIb). After 10 ms the droplet recoils while still attached to the surface. Then, the droplet starts to stabilize and after 65ms a droplet in a ‘petal’ state is observed. For the Case III, the droplet is impacting with a velocity of 1.8 m/s. The droplet hits the surface and it is deformed after 2 ms (Case IIIb). After 10 ms the drop recoils while still attached to the surface. Then, the droplets tarts to stabilize and after 56ms a droplet in a Wenzel state.



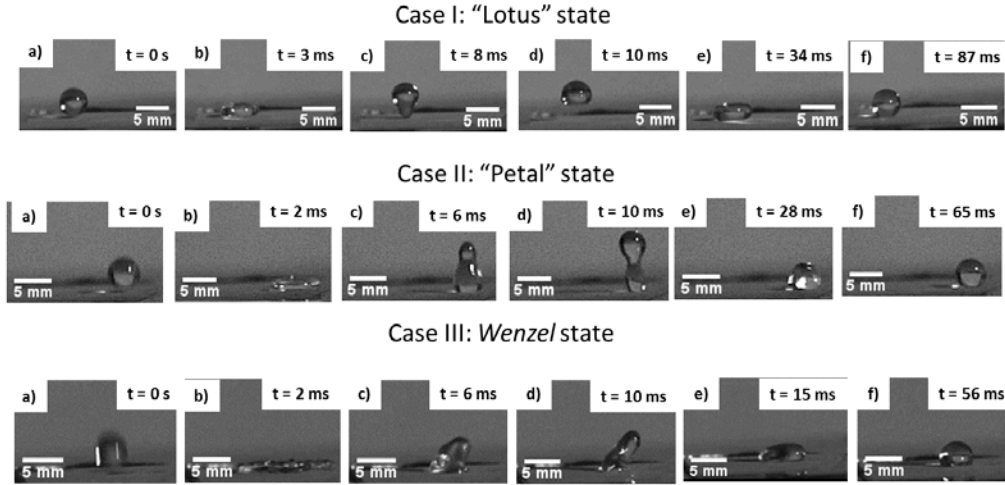


**Figure 7.18:** Snapshots of a 10  $\mu\text{l}$  droplet hitting the surface at 0.6 m/s for the Case I, at 0.8 m/s for the Case II and at 1.8 m/s for the Case III.

The phenomenon of partial pinning existing in the ‘petal’ range of the surfaces, can be explained by the balance between wetting and anti-wetting pressures that govern the impact dynamics of the droplets [171, 173–175]. As discussed in Section 2.4.2, a larger  $P_{wetting}$  than  $P_{antiwetting}$  causes the droplet to wet the surface.

Two pressures contribute to  $P_{wetting}$ , which involves the droplet kinetic energy and the shock-wave formed as a result of droplet surface impact. This  $P_{wetting}$  will be a sum of the Bernoulli pressure, also denoted as dynamic pressure ( $P_D$ ) [52] and water hammer pressure ( $P_{WH}$ ) [173]. Dynamic pressure, which is due to the velocity of the droplet during impingement, is given by:

$$P_D = \frac{1}{2}\rho V^2 \quad (7.14)$$

where  $\rho$  is the density of the impinging liquid and  $V$  the impact velocity. The water hammer pressure corresponds to the shock-waver produced at the moment of impact, and can be strong enough to cause a wetting transition [173], is given by:

$$P_{WH} = k\rho CV \quad (7.15)$$

where  $C$  is the speed of the sound in water (1495 m/s). The coefficient  $k$  refers to a collision factor which describes the elasticity of the collision. A wide range of

experimentally determined values of the coefficient are available in the literature, ranging from 0,2 to 0,001 [34, 175, 176], in function of the impact velocity or the droplet volume. Experiments on droplet impingement typically use a droplet speed of the order of m/s, for which the water hammer coefficient is typically approximated as 0.2 [173, 174]. In our experiments we assume that the coefficient  $k$  has a value of 0.2, taking into consideration that this values could be an overestimation of the water hammer pressure acting on the surface.

The antiwetting pressure ( $P_{antiwetting}$ ) is associated with the capillary pressure ( $P_C$ ). It denotes the force per unit area offered to a water droplet as it transitions from a Cassie state to a Wenzel state. It is defined as follows [171, 175]:

$$P_C = \sigma |\cos\theta_A| \frac{L_C}{A_C} \quad (7.16)$$

where  $\sigma$  is the surface tension,  $\theta_A$  is the advancing contact angle of the flat surface,  $L_C$  is the capillary perimeter and  $A_C$  is the capillary area. Since the superhydrophobic surface have a hierarchical structure, there will be two different capillary pressures [177], i.e. the capillary pressure due to the microstructures ( $P_{CM}$ ) and the one caused by the nanostructures ( $P_{CN}$ ). For the case of the microstructures, we have a square lattice of circular pillars, and its corresponding capillary pressure will be:

$$P_{CM} = \sigma |\cos\theta_A| \frac{\pi D}{P^2 - \frac{\pi}{4} D^2} \quad (7.17)$$

where  $D$  is the diameter of the pillar and  $P$  the pitch. For the case of the microstructures, we have a hexagonal lattice of circular pillars, and its corresponding capillary pressure will be:

$$P_{CN} = \sigma |\cos\theta_A| \frac{\frac{\pi}{2} D}{\frac{\sqrt{3}}{4} P^2 - \frac{\pi}{8} D^2} \quad (7.18)$$

The corresponding capillary pressure exerted by the micropillars will be  $P_{CM} = 0.21kPa$  for  $\theta_A = 105^\circ$ ,  $D = 40\mu m$  and  $P = 115\mu m$ . The corresponding capillary pressure exerted by the nanopillars will be  $P_{CN} = 0.28MPa$  for  $\theta_A = 58^\circ$ ,  $D = 500nm$  and  $P = 750nm$ . This high difference between the two exerted capillary pressures will be the factor that allows the ‘petal’ state, where the water is wetting

the microstructures, but not the nanostructures. For an impact velocity of  $0,8 \text{ m/s}$  (the necessary velocity of obtain the ‘petal’ state), the water hammer pressure is  $P_{WH} = 0.24 \text{ MPa}$ , while the corresponding dynamic pressure is  $P_D = 0.34 \text{ kPa}$ . In this case, the wetting pressure is higher than the capillary pressure exerted by the microstructures, but lower than the capillary pressure exerted by the nanostructures. Thus, the droplets will penetrate into the microstructures but not into the nanostructures, since  $P_{CM} < P_{wetting} < P_{CN}$ . It is important to highlight that this value for the water hammer pressure is an overestimation of the real value, since we are in the range below  $1 \text{ m/s}$ , there is a controversy on the possible value of the  $k$  coefficient for low impact velocities, ranging from  $0,001$  to  $0,2$ .

For higher impact velocities  $V > 1.7 \text{ m/s}$ , the water hammer pressure is  $0.51 \text{ MPa}$  and the dynamic pressure is  $1.49 \text{ kPa}$ , which exceeds both exerted capillary pressures, thus the droplet was able to penetrate both into microstructures and the nanostructures.

Figure 7.19 illustrates schematics of the three possible wetting states existing on our surfaces and their corresponding pressure balances. For impact velocities lower than  $0,8 \text{ m/s}$ , the wetting pressure is lower than the antiwetting pressures, thus the droplet remains in the ‘lotus’ state. For impact velocities in the range of  $0.8 \text{ m/s} < V < 1.7 \text{ m/s}$ , the  $P_{wetting}$  is between the two possible antiwetting pressures, thus the droplet remains in the ‘petal’ state. For impact velocities higher than  $1.71 \text{ m/s}$  the wetting pressure is higher than the anti-wetting pressures, thus the droplet penetrates on the structures, allowing the Wenzel state.

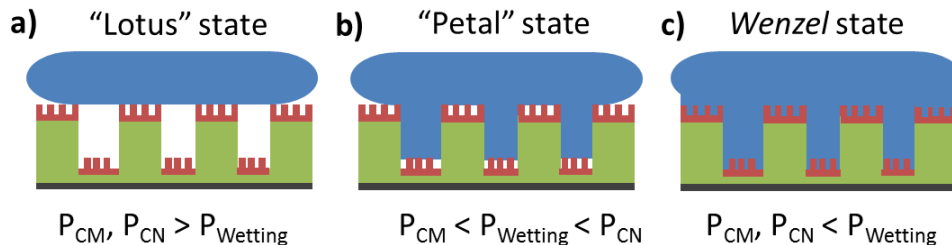


**Figure 7.19:** Schematics of three different wetting states in function of the wetting and antiwetting pressures.

The same behavior was observed on the surface with the nanospikes-micropillars, obtaining a similar needed wetting pressure to wet the microstructures ( $PWH = 0.21MPa$  and  $P_D = 0.26kPa$ ). However, when the wetting pressure exceeded  $0,29MPa$  the droplet was able to wet the nanostructures, which means that the capillary pressure due to the nanospikes is lower. However, due to the random distribution of the structures it was not possible to calculate this pressure theoretically.

Due to the mismatch observed between the water hammer pressure calculated in this study and the experimentally observed transition, we also propose a model, based on the energy barriers needed to provoke the different transitions. The transition between the different observed wetting states was explained in terms of the energy barrier between the different states by Patankar [31].

The energy barrier is understood as the energy required to wet the sides of the structured elements on a superhydrophobic surface. We can interpret the energy barrier in terms of work done by capillary force, which is the product of capillary pressure and liquid-air interfacial area, to displace the air gaps through a height  $h$  within the roughness elements. Thus, the energy barrier between to different wetting states corresponding to one unit cell is:

$$E_{State1} - E_{State2}|_{unit-cell} = P_C (A_C h) \quad (7.19)$$

The total energy barrier between the two states of a droplet of radius  $R$  may be determined by multiplying the energy of the unit cell by the total number of pillars ( $n$ ) beneath de droplet:

$$n = \frac{\pi R^2}{A} \quad (7.20)$$

where  $A$  is the area of the unit cell. As we have two different wetting transitions, as well as two different capillary pressures, we will have two different energy barriers to provoke the two different transitions. Thus, the total energy required to produce the transition to “petal” state will be:

$$E_{Lotus} - E_{Petal} = \pi P_{CM} h R^2 = \pi h R^2 \sigma |\cos\theta_A| \frac{\pi D}{P^2 - \frac{\pi}{4} D^2} \quad (7.21)$$

On the other hand, the total energy required to produce the transition to Wenzel state will be:

$$E_{Lotus} - E_{Wenzel} = \pi P_{CN} h R^2 = \pi h R^2 \sigma |\cos\theta_A| \frac{\frac{\pi}{2} D}{\frac{\sqrt{3}}{4} P^2 - \frac{\pi}{8} D^2} \quad (7.22)$$

Thus, the energy required to produce the transition to the ‘petal’ state corresponds to  $E_{petal} = 2.3mJ$ , and the energy required to produce the transition to Wenzel state corresponds to  $E_{Wenzel} = 2,7J$ . Again, this big difference between the two energy barriers evidences the possibility of having intermediate wetting states.

With these considerations, it is important to highlight the importance of the distribution of the nanostructures on hierarchical structures for effective control of the water adhesion. When the nanostructures are embedded only on the elevated parts of the micropillars, the effect of the hierarchy will be neglectable for dynamic effects, due to the fact that when we have impacting droplets, partial penetration will take place on the cavities of the pillar structures.

Herein, we demonstrate an application of these surfaces on micro droplet transport. The experiments are performed with a water droplet in the ‘petal’ state, as evidenced in Figure 7.20.

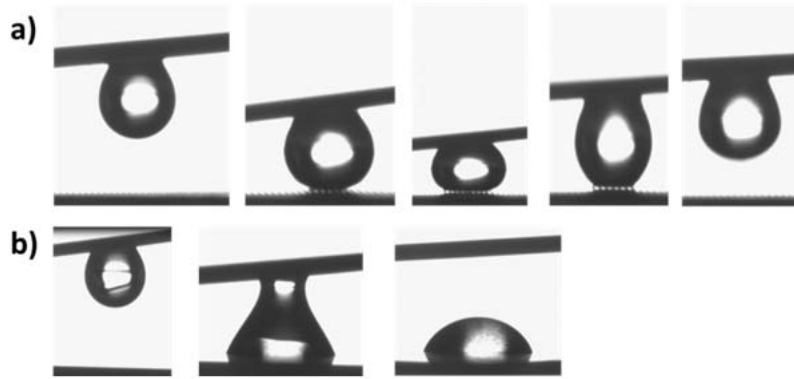


**Figure 7.20:** Snapshots showing a) droplet in contact with a hydrophobic surface and b) droplet in contact with a hydrophilic surface.

The water droplet is placed upside down and is approached both to a hydrophobic and to a hydrophilic surface. In Figure 7.20a, the droplet is brought in contact with a hydrophobic surface; it is observed that the lower the distance between the surfaces, the higher the deformation of the droplet. Then, when the droplet is separated from the hydrophobic surface, it can be observed how the droplet remains on the surface with the ‘petal’ state. In Figure 7.20b, the opposite situation is showed, the droplet is brought in contact with a hydrophilic surface, showing how the droplet is perfectly transferred to the hydrophilic surface without loss of mass.

### 7.3.3 Effect of the inclination

Experiments of droplet impact at oblique conditions were performed in order to evaluate the possible wetting transitions that can take place in such configuration. Since the droplet impacts are oblique, it is necessary to re-define the Weber and the Reynolds numbers in terms of normal impact velocity ( $V_N$ ) and tangential impact velocity ( $V_T$ ) as [178]:

$$We_N = \frac{\rho d V_N^2}{\sigma}; We_T = \frac{\rho d V_T^2}{\sigma}; \quad (7.23)$$

$$Re_N = \frac{\rho d V_N}{\eta}; Re_T = \frac{\rho d V_T}{\eta}; \quad (7.24)$$

It is reasonable to expect that the normal velocity component may cause the water penetration rather than the absolute speed. We thus use the We number that is dependent on this component ( $We_N$ ). For these tests, droplets with a range of normal Weber numbers from 2 to 244 and Reynolds number from 525 to 8398 were used. Room-temperature (25 °C) droplets were used at inclinations of 20, 30 and 45 °.

Although the rebound is predicted with high Weber numbers, droplets often rebound only partially when their Weber number exceeds a certain threshold value. This partial rebound regime occurs when the meniscus of impacting water droplets can penetrate between the surface textures and disrupt the air pockets [173]. For this reason, different velocities were tested. Initially, a low impact velocity (below the threshold to produce the 'petal' effect on 0 ° tilt surfaces) to observe the impact and rebound of the droplet. Secondly, an intermediate impact velocity, to analyse if we can have 'petal' droplets in oblique conditions, and thirdly, high impact velocities, to observe if Wenzel transition occurs.

Figures 7.21, 7.22 and 7.23 show a set of snapshot of complete and partial rebounds, the 'intact' mode fabricated surfaces have an inclination of 20, 30 and 45 °, respectively. Complete rebounds were observed at low and moderate impact velocities as the air layers below the droplet remains intact, while the pinning is observed at high velocities, when the air pockets are disrupted by the wetting pressure of the impinging droplet. The transition observed in these experiments is a direct Cassie-to-Wenzel transition, thus, petal state it is not observed on oblique impacts. Interestingly, these transitions take place at the same conditions that the Wenzel transition takes place on the 0 ° tilted surface.

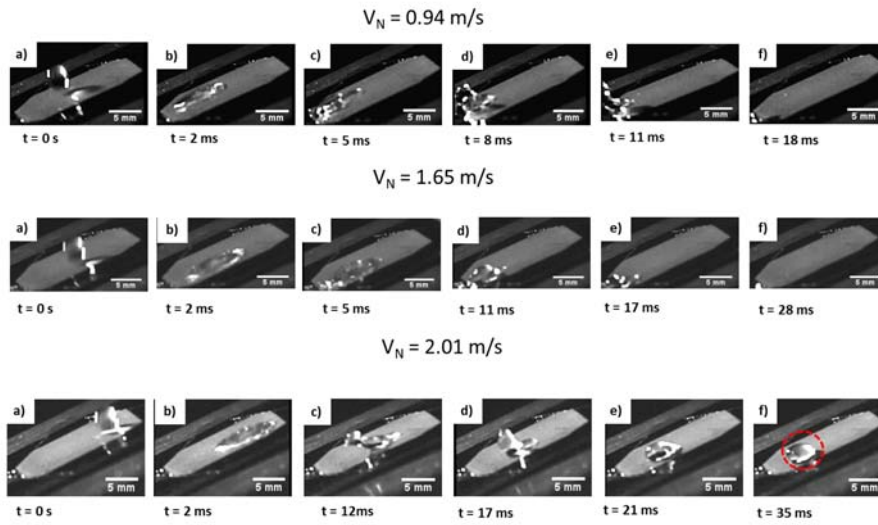


**Figure 7.21:** Snapshots of a 10  $\mu\text{l}$  droplet hitting the surface ( $20^\circ$  tilt) at normal velocities of 0.94 m/s, 1.65 m/s and at 2.01 m/s. Pinning of the droplet occurs at velocities higher than 2 m/s.

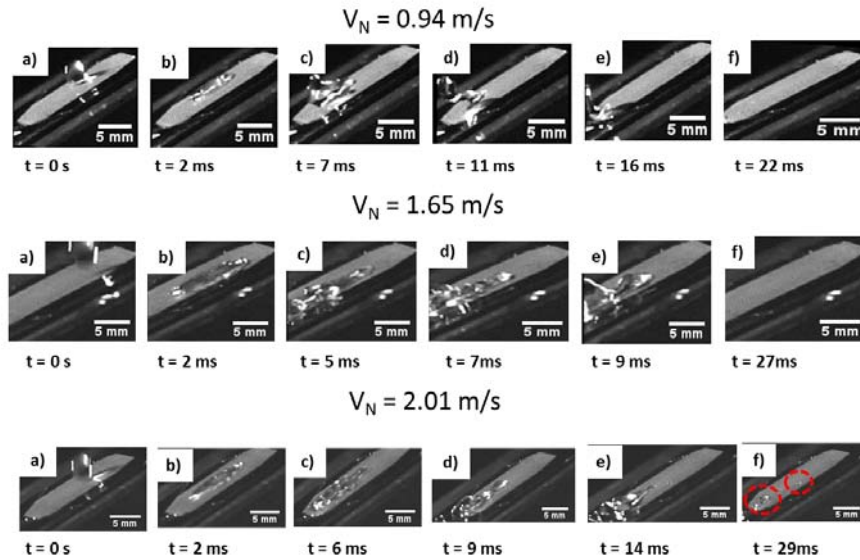


**Figure 7.22:** Snapshots of a 10  $\mu\text{l}$  droplet hitting the surface ( $30^\circ$  tilt) at normal velocities of 0.94 m/s, 1.65 m/s and at 2.01 m/s. Pinning of the droplet occurs at velocities higher than 2 m/s.



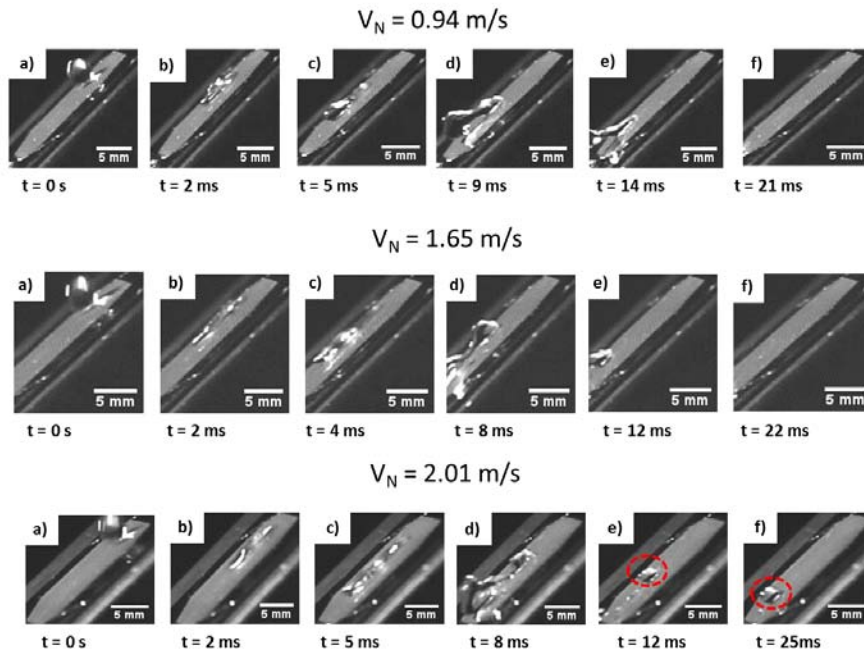


**Figure 7.23:** Snapshots of a 10  $\mu\text{l}$  droplet hitting the surface ( $45^\circ$  tilt) at normal velocities of 0.94 m/s, 1.65 m/s and at 2.01 m/s. Pinning of the droplet occurs at velocities higher than 2 m/s.

Table 7.7 shows a summary of the transitions to Wenzel state for each inclination. It can be observed that the transitions occur at different droplet height release, but the normal components of the velocity and the Weber number remain rather constant. These results indicate that the wetting pressure exerted by the normal velocity is responsible for the disruption of the air pockets.

Inclination	0 <sup>0</sup>	20 <sup>0</sup>	30 <sup>0</sup>	45 <sup>0</sup>
<i>Transition height (m)</i>	0.15	0.17	0.21	0.30
Impact velocity (m/s)	1.71	1.83	2.03	2.42
We number	164	186	229	329
Normal impact velocity ( $V_N$ )(m/s)	<b>1.71</b>	<b>1.70</b>	<b>1.76</b>	<b>1.71</b>
Normal We number ( $We_N$ )	164	163	172	162

**Table 7.7:** Summary of results for each of the tilt angles tested in this study. The droplet diameters are 4 mm.

### 7.3.4 Summary

We describe the fabrication of hybrid hierarchical patterned surfaces with tunable wetting properties. A hierarchical surface fabricated with a combination of two different materials exhibit both ‘lotus’ and ‘petal’ effect by varying the deposition conditions of the water droplets, without the needing of any chemical modification on the surface. The great difference between the capillary pressures exerted by the microstructures and by the nanostructures was the key factor that allowed us to tailor effectively the adhesiveness of the water droplets. By imposing a low capillary pressure to the microstructures and a high capillary pressure to the nanostructures, we created a energetic gap, where the ‘petal’ state can be produced.

The performed experiments allows us to have an effective control over the surfaces. It is possible to control the desired wetting state in function of the impact velocity of the droplet and the inclination of the superhydrophobic surface. We strongly believe that these results can elucidate a better understating on the design of multifunctional

surfaces.

## 7.4 Oleophobic surfaces

Intensive research efforts have been performed during the last years to study and realize surfaces with self-cleaning properties. However, it still remains a big challenge that, although one surface could perform superhydrophobic properties, it does not mean that the surface will repel other liquids like oils. For instance, in the case of the lotus leaf, Tuteja et al. [179] showed that although the surface of the lotus leaf exhibits very high water contact angle and small roll off angle, a hexadecane droplet actually wets and spreads on it. Furthermore, most of the common contaminants and pollutants are organic materials, which sticks to superhydrophobic surfaces and cannot be removed easily.

As previously discussed in Chapter 2, engineering surfaces that show low affinity toward most of the low surface tension liquids like oils is not achievable unless re-entrant or overhanging structure in addition to low surface energy are provided. A liquid cannot penetrate in a pattern with an overhanging structure because of the capillary force at the solid/liquid interface near the structure. As a result, the liquid cannot touch the bottom of the pattern and a layer with trapped air is formed between the surface and the liquid.

Accordingly, recent approaches have employed chemically treated materials such as glass and silicon oxides or polymers to make re-entrant structures with oil-repellency properties. However, the efficient fabrication of micro and nanostructures with re-entrant or overhanging structures has not been reported, since all the reported fabrication methods involve complicated and high-cost processes.

Nanoimprint lithography (NIL) is a good alternative towards the conventional fabrication methods due to its low cost and high throughput. However, despite great efforts have been made to improve the applications of NIL; it has not been demonstrated as a suitable approach to fabricate overhanging structures [180–183]. Here we show the potential of NIL to fabricate complex overhanging structures.

By a novel one-step controlled electroplating process we produced mushroom-like structures with controlled shape. These structures were fabricated using the template-assisted electroplating concept. We create a polymer mask with an array of cylindrical holes by means of a photolithography process over a conductive substrate

for subsequently realize the electroplating process only on the opened channels of the surface.

A precise control on the electroplating parameters is needed to produce the desired shape of our surface, since a careful control over the overgrowth of the pillars is needed. The total area of the surface was  $0.34 \text{ dm}^2$ . By having a square array of cylinders with diameter and pitch  $4 \text{ }\mu\text{m}$  and  $11 \text{ }\mu\text{m}$ , respectively, we can calculate the area to be plated corresponding to a unit cell, being  $1.32 \cdot 10^{-8} \text{ dm}^2$ . Thus, the number of unit cells to be plated will be 25708884.

Inside each unit cell, the area to be plated will be the area corresponding to one cylinder, being its area  $1.25 \cdot 10^{-9} \text{ dm}^2$ . Therefore, the total area to be plated will correspond to the area of 25708884 cylinders, being  $0.032 \text{ dm}^2$ . By applying a power current of  $0.03\text{A}$ , the achieved current density will correspond to  $1 \text{ A/dm}^2$ . The surfaces were electroplated using the same current density at different times, thus achieving mushroom-like structures with different overhanging degrees.

These structures were successfully replicated in a soft PDMS stamp followed by a direct UV-NIL step to replicate them in a photocurable resist. The surface morphology, in combination with a low surface energy coating demonstrated an amphiphobic effect. Enhanced repellency was obtained over a wide range of low surface tension liquids while the small sliding angles indicating the Cassie-Baxter state.

Nickel mushroom-like structures were prepared on a silicon wafer by means of photolithography and electroplating techniques. The wafers were coated with a  $50 \text{ nm}$  Au layer on top of a  $5 \text{ nm}$  Cr adhesive layer (Figure 7.24a). Then, the wafer was spin-coated with AZ 2035 nLoF photoresist. The photoresist layer was exposed to UV light during  $60 \text{ sec}$  using a quartz mask with a square array of cylindrical pillars, having a diameter and pitch of  $4$  and  $11 \text{ }\mu\text{m}$ , respectively. Development was done using AZ 726MIF during  $1 \text{ minute}$  (Figure 7.24b).

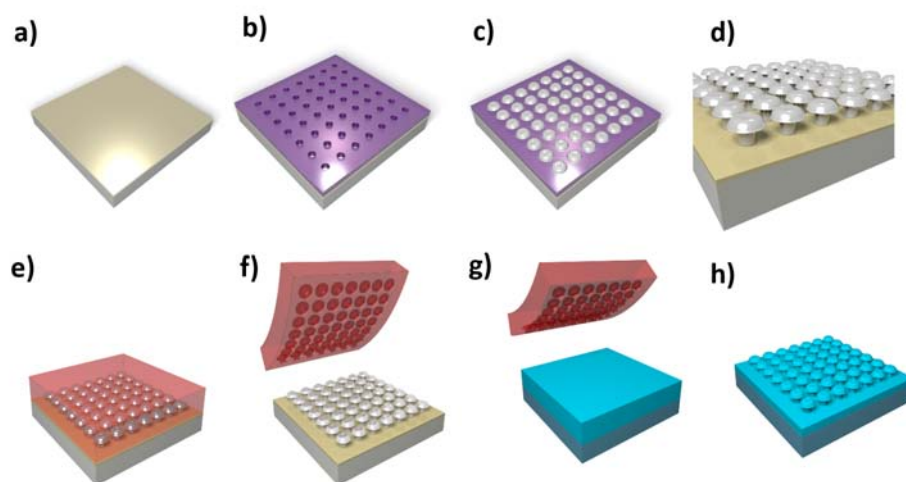


**Figure 7.24:** Schematic of the fabrication process followed to develop the polymeric mushroom-like structures. The template was fabricated in nickel by electroplating. A soft stamp was produced with the negative pattern. This soft stamp was used to produce mushroom-like structures by direct UV-NIL in Ormocomp.

The surface was then placed in an electroplating bath solution of a combination of nickel sulphamate ( $Ni(SO_3N_2)_2$ ) (90 g/l), nickel chloride ( $NiCl_2 \cdot 6H_2O$ ) (11.2 g/l) and boric acid ( $H_3BO_3$ ) (45 g/l). The bath solution was kept at 55 °C and pH was 4.0.

When the nickel reached the top of holes area left by the resist, the nickel started to overgrow uniformly on the surrounding areas of the pillar, thus obtaining the desired mushroom-like shape (Figure 7.24c). The photoresist layer was then stripped using acetone and oxygen plasma (Figure 7.24d). With this method, an easy control over the morphology and overhanging degree of the mushroom-like structures can be achieved.

The wafer with the nickel mushroom-like structures was treated with a fluorinated antiadhesion layer (Optool DSX) to alter the surface energy for easy mold releasing. Subsequently, a soft PDMS replica was fabricated by the experimental procedure reported in Section 5.1.1 (Figure 7.24e,f). The polymer used to fabricate the amphiphobic surfaces was Ormocomp. Ormocomp was spin-coated onto a silicon wafer, and the PDMS mold was placed on the resist surface (Figure 7.24g). Finally, pressure and UV light were applied in order to crosslink the resist and create the mushroom-like structures (Figure 7.24h).

To improve the amphiphobic behavior, theOrmocomp surfaces were treated with a fluorinated antiadhesion layer (Optool DSX). The combination of the treatment with the overhanging structures enables the formation of a favourable liquid–air interface for lower surface tension liquids, such as oils, that exhibit contact angles less than  $90^\circ$  on the corresponding flat surface.

All the steps followed here are very simple and inexpensive, as well as widely used methods by industry, allowing the mass production of mushroom-like structures with amphiphobic characteristics.

#### 7.4.1 Morphology control

By varying the electroplating parameters we successfully managed to realize tailored size (degree of overhanging) and spacing mushroom-like structures. Figure 7.25 illustrates tilted view SEM images of nickel mushroom like structures with different overhanging degrees. Figure 7.25a corresponds to a low degree of overhanging, with a distance between the mushroom caps between in the 3-3.5  $\mu\text{m}$  range. Figure 7.25b corresponds to a medium degree of overhanging, with a distance between the mushroom caps between 2 and 2.5  $\mu\text{m}$ , while Figure 7.25c corresponds to a high degree of overhanging, being the distance between the mushroom caps between 0.8 and 1  $\mu\text{m}$ . This last separation was found to be the minimum interspace distance which one could achieve a successful pattern transfer by means of direct UV-NIL. This limitation is due to the interspace distance and does not imply that the UV-NIL replication technique has a threshold in terms of dimensions. Smaller distances could be achieved by modifying the electroplating conditions however, it was not possible to produce soft PDMS replicas for samples with a higher overhanging degree.

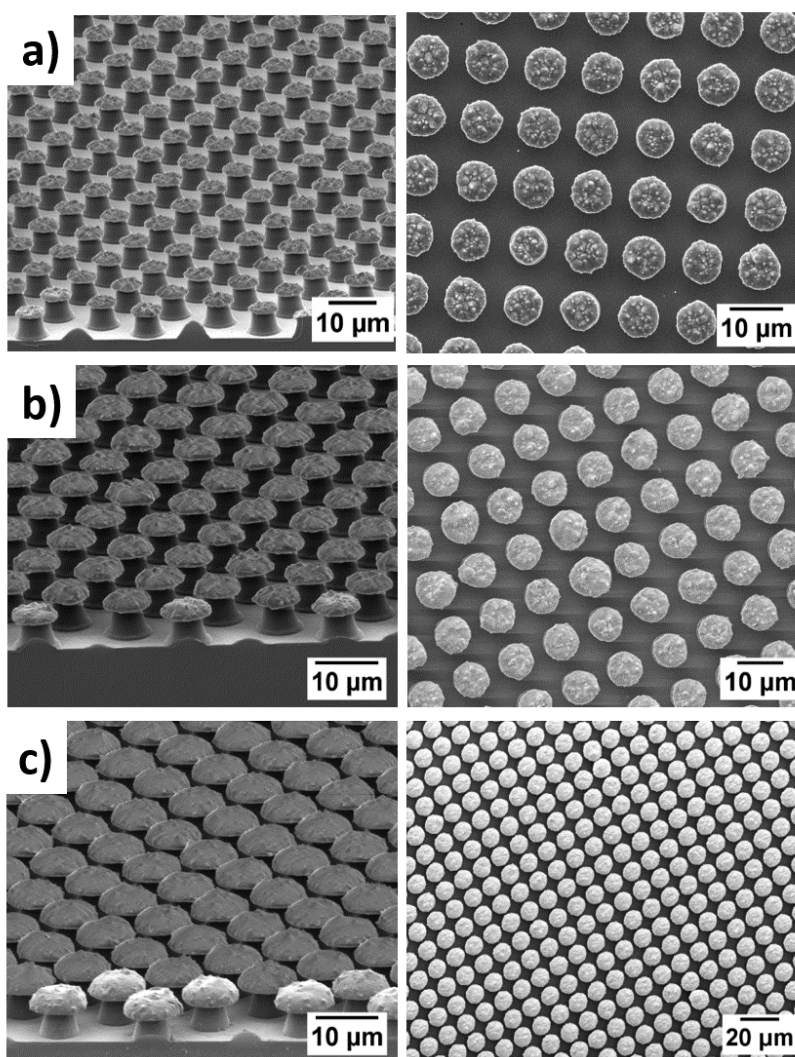


**Figure 7.25:** SEM images showing Ormocomp mushroom-like structures with different overhanging degrees. Distance between caps of a) 3-3.5  $\mu\text{m}$ , b) 2-2.5  $\mu\text{m}$  and c) 0.8-1  $\mu\text{m}$ .

Controlling the surface morphology is a key issue when designing amphiphobic structures, since a high degree of overhanging surface area is needed to avoid water penetration, while at the same time, a low solid-liquid contact fraction is needed. In this work, different degree of overhanging mushroom-like structures were fabricated in order to find the optimum conditions to obtain a respectable water/oil repellency and a high degree of imprinting fidelity.



### 7.4.2 Wetting analysis

The low surface energy, combined with the rough surface texture, led to a superhydrophobic and oleophobic surface rendered by the mushroom-like structures. Table 7.8 shows static and dynamic water contact angle measurements and their standard deviation corresponding to the different fabricated mushroom-like structures. Treated flat Ormocomp surfaces were found to be hydrophobic with water contact angles of  $112^{\circ}$ . Structured Ormocomp resulted superhydrophobic with water contact angles as high as  $155^{\circ}$  and sliding angles as low as  $8^{\circ}$ . All the fabricated samples exhibit superhydrophobic behavior, with the best values obtained for the mushroom-like structures with a medium overhanging degree. This behavior is explained through the solid-liquid contact fraction contact: a low solid-liquid contact fraction is needed to produce air trapping below the droplet; however, if this fraction is too small, the liquid will partially penetrate into the structures. For this reason, optimum structures require a perfect control over the pattern definition to produce a remarkable superhydrophobic and oleophobic effect. For the case of a low overhanging degree, although the solid-liquid contact fraction is low, the great distance between adjacent mushrooms produce a partial penetration of the droplet meniscus, leading to a decrease on the contact angle value. For the case of a high overhanging degree, the solid-liquid contact fraction becomes higher due to the small distance between adjacent mushrooms. To optimum surfaces were found to be those with a medium degree of overhanging, yielding the best values in terms of static and dynamic contact angles.

<i>Surface structure</i>	Contact angles [ $^{\circ}$ ]		
	<i>Static</i>	<i>Sliding</i>	<i>Hysteresis</i>
Flat Surface	$112 \pm 3$	$35 \pm 3$	$40 \pm 6$
Low overhanging degree	$148 \pm 3$	$11 \pm 4$	$10 \pm 4$
Medium overhanging degree	$155 \pm 1$	$8 \pm 2$	$6 \pm 3$
High overhanging degree	$147 \pm 3$	$15 \pm 3$	$12 \pm 5$

**Table 7.8:** Experimental water contact angles measurements for the Ormocomp mushroom-like structures with different overhanging degrees.

To accurately evaluate the oil-repellent properties of the mushroom-like structures, several liquids have been selected having a wide range of surface tensions. The selected liquids for this study were water, diiodomethane, ethylene glycol and olive oil, possessing surface tensions of 71.99, 50.80, 47.70 and 32.03 mN/m, respectively [68].

Data related to apparent contact angles, contact angle hysteresis, and sliding angles droplets of various liquids are summarized in Table 7.9. The same behavior is observed for the case of the oils, since the best obtained values arise from the surfaces with a medium overhanging degree. It is important to highlight that, while with the water a pure Cassie-Baxter state is observed, for the case of the oils, a slight decrease in the contact angle values is observed. This is due to the lower surface tensions and higher density of these liquids, which produces partial penetration on the structures. It is plausible to suggest that the diiodomethane, ethylene glycol and olive oil demonstrate the so-called mixed wetting regime, combining the features of the Cassie and Wenzel wetting models.

	Contact angles [ $^{\circ}$ ]								
	<i>Diiodomethane</i>			<i>Ethylene glycol</i>			<i>Olive oil</i>		
<i>Surface Structure</i>	Static	Sliding	Hysteresis	Static	Sliding	Hysteresis	Static	Sliding	Hysteresis
Flat Surface	$83 \pm 4$	$20 \pm 3$	$18 \pm 4$	$88 \pm 3$	$25 \pm 2$	$22 \pm 3$	$73 \pm 3$	$38 \pm 3$	$26 \pm 3$
Low overhanging degree	$138 \pm 3$	$10 \pm 3$	$11 \pm 3$	$140 \pm 2$	$17 \pm 3$	$14 \pm 4$	$136 \pm 2$	$22 \pm 3$	$20 \pm 4$
Medium overhanging degree	$140 \pm 2$	$8 \pm 2$	$10 \pm 3$	$142 \pm 3$	$16 \pm 2$	$13 \pm 4$	$138 \pm 3$	$20 \pm 3$	$18 \pm 5$
High overhanging degree	$128 \pm 3$	$15 \pm 3$	$12 \pm 4$	$132 \pm 2$	$18 \pm 3$	$17 \pm 4$	$130 \pm 3$	$26 \pm 2$	$20 \pm 4$

**Table 7.9:** Experimental contact angles measurements for theOrmocomp mushroom-like structures with different overhanging degrees measured with liquids with different surface tension.

It should be stressed that the high apparent contact angle, such as the obtained in Figure 7.26, does not guarantee the oil repellency of a surface. Low contact angle hysteresis and sliding angle are also necessary to provide easy sliding of the droplets and perform self-cleaning properties of the surface. From the Table 7.9 it can be observed that high contact angle values are accompanied by low hysteresis and sliding angles. For the case of the samples fabricated with a medium overhanging degree, contact angles as high as  $140^{\circ}$  and sliding angles as small as  $8^{\circ}$  were found with the diiodomethane.

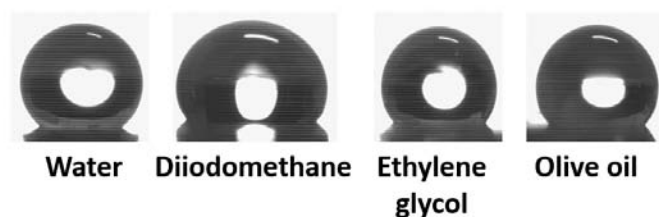


**Figure 7.26:** Photographs of 5  $\mu\text{l}$  droplets of different liquids obtained on the surface with medium overhanging degree.

Figure 7.27 shows the contact angles as a function of the surface tension of the different tested liquids. It is seen that the contact angle diminishes as the surface tensions decreases. However, one exception is observed for the case of diiodomethane, since their contact angle values are lower even being its surface tension higher than for olive oil and ethylene glycol.

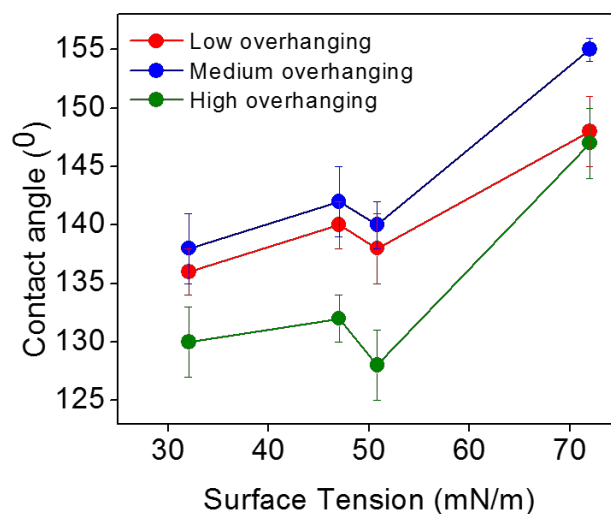


**Figure 7.27:** Graph showing the obtained contact angle values for liquids with different surface tensions.

This can be explained taking into account that the effect of the gravity can induce sagging effect in certain liquids, amplifying variations in contact angle measurements. This effect can be quantified in term of the dimensionless Bond number ( $Bo$ ), defined using the maximum droplet width and the capillary length of the liquid. The Bond number is commonly used as a dimensionless measure of the extent of gravitational

forces relative to capillary forces acting on the drop. As discussed in Chapter 2, the capillary length of a liquid is defined by:

$$\kappa_C = \sqrt{\frac{\gamma_{LV}}{\rho g}} \quad (7.25)$$

where  $\gamma_{LV}$  is the liquid-air surface tension,  $\rho$  is the density of the liquid and  $g$  is the gravity. Thus, the Bond number is defined as [184]:

$$Bo = \frac{\rho g l^2}{\gamma_{LV}} \quad (7.26)$$

where  $l$  is the maximum half-width of the drop. The capillary length of the diiodomethane is  $a = 1.25$  mm (note that the capillary length of the water is  $a = 2.7$  mm [25]). For a typical 5  $\mu$ l droplet, this value produce a Bond number of  $Bo = 0.075$ . At  $Bo = 0$ , i.e., in the absence of gravity, the profile of the liquid droplet is described by a spherical cap. However, as the  $Bo$  number increases the effect of the gravity becomes more relevant. A comparison of a droplet with  $Bo$  numbers of 0 and 0.075 is depicted in Figure 7.28.

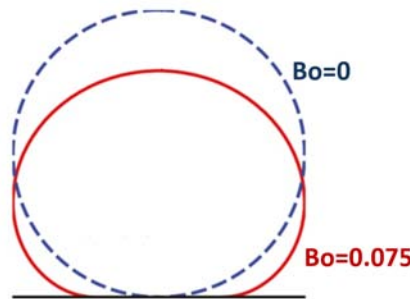


**Figure 7.28:** Profiles of liquid droplets of volume  $v = 5$   $\mu$ l and capillary length  $a = 1.25$  mm ( $Bo = 0.075$ , solid line). In comparison with a spherical profile ( $Bo$ , dashed line), it can be observed the effect of the gravity on the sagging effect [184].

This small capillary length arising from the diiodomethane is due to the high density of this liquid, as can be observed in the summary of surface tensions and liquid densities depicted in Table 7.10. It can be observed that diiodomethane, although possessing lower surface tension than water, it has a greater density, thus diminishing

its capillary length. It is plausible to propose, that the effect of the gravity produce a sagging effect for diiodomethane, producing partial penetration of the meniscus inside the cavities, thus diminishing the contact angle value considerably.

<i>Liquid</i>	<i>Surface tension (mN/m)</i>	<i>Density (g/m<sup>3</sup>)</i>
Water	71.99	1
Diiodomethane	50.80	3.32
Ethylene glycol	47.70	1.11
Olive oil	32.03	0.8

**Table 7.10:** : Surface tension and density values for the liquids used in this study.

### 7.4.3 Robustness of the oleophobicity

It has been suggested that there exists a certain critical value of the surface tension,  $\gamma_{LV}$ , of a liquid at which the oleophobicity is no longer observed; and a droplet demonstrates a high sticky state [185, 186]. For the experimental determination of the critical surface tension ( $\gamma_{LV}$ ), several groups used water/alcohol solutions, possessing controllable surface tension. Droplets with different water/ethanol concentrations were used in this study to define the critical surface tension of a liquid to produce sticky droplets, thus losing the oleophobic behavior.

The concentration of ethanol in the droplet was gradually increased, and the contact angle was measured as a function of the surface tension of the water/ethanol liquid. The surface tensions of the water/ethanol solutions displayed in Figure 7.29 were taken from existing literature [187].

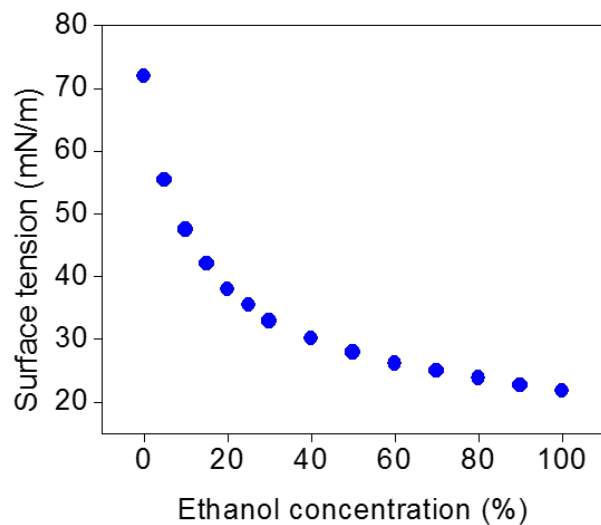


**Figure 7.29:** Surface tension obtained for different ethanol concentrations in water.

The dependence between the contact angle value and the liquid surface tension is depicted in Figure 7.30. At a certain concentration of ethanol, an abrupt change in the contact angle was observed, indicating the onset of the wetting transition responsible for the loss of the oleophobicity. This big change on the contact angle was observed at a surface tension of  $\approx 27.9$  mN/m.

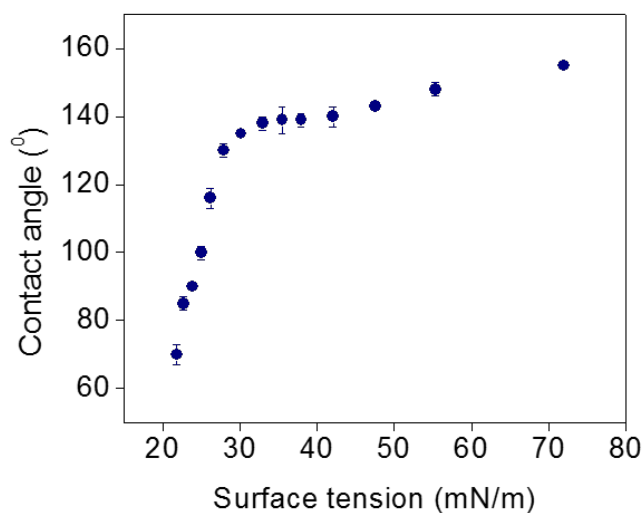


**Figure 7.30:** Measured contact angle of different water/ethanol solutions possessing different surface tensions.

Comparing these values with the values obtained for common test liquids (Table

7.8 and Table 7.9), it can be observed that the surface tensions of these liquids is larger than the critical surface tension found in water/ethanol mixtures. For the case of a surface tension around 50 mN/m, the contact angle obtained by mixing water/ethanol was  $148^\circ$ . Diiodomethane has approximately the same surface tension, but its contact angle was found to be  $140^\circ$ . This provides a clear evidence of the influence of the gravity to produce a sagging effect in this liquid.

#### 7.4.4 Summary

We have developed a novel fabrication method to produce overhanging structures by one-step process. Mushroom-like structures were fabricated by electroplating of nickel over a conductive surface with a resist used as a mask to produce the overhanging structures. We also have demonstrated NIL as a powerful technique to direct imprint overhanging structures by using a soft PDMS stamp. These mushroom-like structures exhibited amphiphobic properties over a wide range of liquids with different surface tensions. Furthermore, the critical surface tension that allow oleophobicity was found experimentally by measuring the contact angle values using different concentrations of water and ethanol.



## Chapter 8

# Conclusions and Prospects

The research conducted in this thesis is concentrated on the development of different micro and nanopatterning techniques, based on nanoimprint lithography-based methods, and the exploration of its applications in functional surfaces with special wetting properties.

Different fabrication techniques were developed that allowed us the realization of 3D hierarchical micro and nanostructures. We explored some industrial manufacturing techniques, such as injection molding or electroplating, and we paved the way to use them for nanotechnology applications.

A free-residual layer nanoimprint technique was developed and implemented to address two different applications.

- Firstly, the combination of this technique with an up-plating process allowed us to fabricate fully metallic nickel templates for injection molding purposes.
- Secondly, the combination of this technique with UV-NIL enabled the fabrication of tailored 3D micro/nano structures for superhydrophobic applications. Subsequently electroplating process on these structures permitted the fabrication of nickel templates for injection molding purposes.

All the fabricated 2D and 3D structures were carefully analyzed, both from the fabrication and the wetting point of view. The effect of the structural hierarchy was demonstrated to improve the superhydrophobic behavior, as observed in both

droplet roll off and hysteresis. A static contact angle value of  $170^\circ$  with a hysteresis of  $4^\circ$  was achieved without additional chemical treatment.

To the best of our knowledge, this is the largest static contact angle obtained on a patterned surface without the need of applying a low surface energy coating. Dynamic measurements were performed on these surfaces, showing an excellent self-cleaning ability, as well as a strong robustness over impacting drops.

Having a precise control of the fabrication parameters, surfaces with tuneable wetting properties were fabricated. A hierarchical surface fabricated with a combination of two different materials exhibit both ‘lotus’ and ‘petal’ effect by varying the deposition conditions of the water drops, without the need of any chemical modification of the surface. The huge difference between the capillary pressures exerted by the microstructures and by the nanostructures was the key factor that allowed us to tailor effectively the adhesiveness of the water drops. This study has contributed to a better understating of the wettability and design of multifunctional surfaces.

A new fabrication method was developed to produce overhanging structures in one-step process. Mushroom-like structures were fabricated by electroplating of nickel over a conductive surface with a resist used as a mask resulting in overhanging structures. Additionally, these structure were directly imprinted by using a soft PDMS stamp. These mushroom-like structures exhibited amphiphobic properties over a wide range of liquids of different surface tensions. The critical surface tension that allowed oleophobicity was found experimentally by measuring the contact angle values using different concentrations of water and ethanol.

Concerning future research, there are different routes to continue the research presented in this thesis. Efficient superoleophobic surfaces that can remain in the Cassie-Baxter state for low surface tension liquid over different stimuli still remain a challenging task.

Although injection molding was demonstrated as a suitable technique to produce industrial functional surfaces, the parameters need to be optimized to produce good quality structures.

On the other hand, superhydrophobic surfaces that could keep their behavior

over nano and microdroplet condensation is an issue that can have a great deal of interest for different real-life applications. Pure microstructures are useless dealing with dropwise condensation and pure nanostructures present usually a not stable superhydrophobic state. Therefore, a proper combination of structures should be found in order to obtain stable superhydrophobic surfaces over water condensation.

The effect on the surface topography extended to super cooled water droplets could offers a better understanding on the development of anti-ice surfaces, which remains as a challenging task with an enormous amount of possible applications, such as in roads, air and sea transportation, marine and offshore structures, wind turbines and heat exchangers.

Furthermore, the fabrication procedure developed here to produce hierarchical structures with different materials could be used for producing bio scaffolds. Having the possibility of producing micro and nanostructures with different materials, this could be used to produce selectively cell growing. By having one of the materials with anti-fouling properties and other material that could promote cell growing, a selective cell growing could be attained [188].

On the other hand, it has also been demonstrated that the Gecko legs also exhibit a hierarchical combination of micro and nanofibril structures. Furthermore, several studies have demonstrated the advantage of having hierarchical structures for adhesive applications [189,190]. A careful study of the implications of having a micropillar/nanopillar structure for adhesive application it is of a special interest.

This thesis extends the knowledge of the potential manufacturing processes that can be used for functional surfaces applications. It has shown the possibility of produce controlled 3D hierarchical surfaces in a controlled manner for achieving a precise control over the surface wetting characteristics.

# Bibliography

- [1] B. Bhushan. Biomimetics: lessons from nature—an overview. *Philosophical Transactions of the Royal Society of London A*, 367(1893):1445–1486, 2009.
- [2] M. Nosonovsky and P.K. Rohatgi. *Biomimetics in Materials Science: Self-Healing, Self-Lubricating, and Self-Cleaning Materials*. Springer, 2011.
- [3] B. Bhushan. *Biomimetics: Bioinspired Hierarchical-Structured Surfaces for Green Science and Technology*. Springer, 2016.
- [4] M. Nosonovsky and B. Bhushan. *Multiscale Dissipative Mechanisms and Hierarchical Surfaces: Friction, Superhydrophobicity, and Biomimetics*. Springer, 2008.
- [5] W. Barthlott and C. Neinhuis. Purity of the sacred lotus, or escape from contamination in biological surfaces. *Planta*, 202(1):1–8, 1997.
- [6] C. Neinhuis and W. Barthlott. Characterization and distribution of water-repellent, self-cleaning plant surfaces. *Annals of Botany*, 79(6):667–677, 1997.
- [7] H. J. Ensikat, P. Ditsche-Kuru, C. Neinhuis, and W. Barthlott. Superhydrophobicity in perfection: the outstanding properties of the lotus leaf. *Beilstein Journal of Nanotechnology*, 2:152–161, 2011.
- [8] L. Feng, Y. Zhang, J. Xi, Y. Zhu, N. Wang, F. Xia, and L. Jiang. Petal effect. a superhydrophobic state with high adhesive force. *Langmuir*, 24(8):4114–4119, 2008.

- 
- [9] K. Liu, J. Du, J. Wu, and L. Jiang. Superhydrophobic gecko feet with high adhesive forces towards water and their bio-inspired materials. *Nanoscale*, 4(3):768–772, 2012.
- [10] B. Dean and B. Bhushan. Shark-skin surfaces for fluid-drag reduction in turbulent flow: a review. *Philosophical Transactions of the Royal Society of London A*, 368(1929):4775–4806, 2010.
- [11] Y. Zheng, X. Gao, and L. Jiang. Directional adhesion of superhydrophobic butterfly wings. *Soft Matter*, 3(2):178–182, 2007.
- [12] R. Blossey. Self-cleaning surfaces - virtual realities. *Nature Materials*, 2(5):301–306, 2003.
- [13] T. Darmanin and F. Guittard. Recent advances in the potential applications of bioinspired superhydrophobic materials. *Journal of Materials Chemistry A*, 2(39):16319–16359, 2014.
- [14] E. Ueda and P. A. Levkin. Emerging applications of superhydrophilic-superhydrophobic micropatterns. *Advanced Materials*, 25(9):1234–47, 2013.
- [15] A. Malshe, K. Rajurkar, A. Samant, H. N. Hansen, S. Bapat, and W. Jiang. Bio-inspired functional surfaces for advanced applications. *CIRP Annals-Manufacturing Technology*, 62(2):607–628, 2013.
- [16] H. Schiff. Nanoimprint lithography: An old story in modern times. a review. *Journal of Vacuum Science & Technology B*, 26(2):458, 2008.
- [17] Nanopatterning - a global market report. 09/2015.
- [18] R. N. Wenzel. Resistance of solid surfaces to wetting by water. *Industrial & Engineering Chemistry*, 28(8):988–994, 1936.
- [19] A. B. D. Cassie and S. Baxter. Wettability of porous surfaces. *Transactions of the Faraday Society*, 40(0):546–551, 1944.

- 
- [20] B. Bhushan and M. Nosonovsky. The rose petal effect and the modes of superhydrophobicity. *Philosophical Transactions of the Royal Society of London A*, 368(1929):4713–28, 2010.
- [21] M. Jin, X. Feng, L. Feng, T. Sun, J. Zhai, T. Li, and L. Jiang. Superhydrophobic aligned polystyrene nanotube films with high adhesive force. *Advanced Materials*, 17(16):1977–1981, 2005.
- [22] L. Gao and T. J. McCarthy. Teflon is hydrophilic. comments on definitions of hydrophobic, shear versus tensile hydrophobicity, and wettability characterization. *Langmuir*, 24(17):9183–9188, 2008.
- [23] T. Young. An essay on the cohesion of fluids. *Philosophical Transactions of the Royal Society of London*, 95:65–87, 1805.
- [24] B. Bhushan. *Nanotribology and Nanomechanics II: Nanotribology, Biomimetics, and Industrial Applications*. Springer, 2011.
- [25] S. H. Kim. Fabrication of superhydrophobic surfaces. *Journal of Adhesion Science and Technology*, 22(3-4):235–250, 2008.
- [26] M. Strobel and C. S. Lyons. An essay on contact angle measurements. *Plasma Processes and Polymers*, 8(1):8–13, 2011.
- [27] A.-M. Kietzig. Comments on “an essay on contact angle measurements” – an illustration of the respective influence of droplet deposition and measurement parameters. *Plasma Processes and Polymers*, 8(11):1003–1009, 2011.
- [28] G. Kwak, M. Lee, K. Senthil, and K. Yong. Impact dynamics of water droplets on chemically modified wox nanowire arrays. *Applied Physics Letters*, 95(15):153101, 2009.
- [29] F. M. Fowkes. *Contact Angle, Wettability, and Adhesion*, volume 43 of *Advances in Chemistry*. American Chemical Society, 1964.
- [30] Yong C. J. and B. Bharat. Contact angle, adhesion and friction properties of micro-and nanopatterned polymers for superhydrophobicity. *Nanotechnology*, 17(19):4970, 2006.

- 
- [31] N. A. Patankar. Transition between superhydrophobic states on rough surfaces. *Langmuir*, 20(17):7097–7102, 2004.
- [32] M. Reyssat, J. M. Yeomans, and D. Quéré. Impalement of fakir drops. *EPL (Europhysics Letters)*, 81(2):26006, 2008.
- [33] B. Liu and F. F. Lange. Pressure induced transition between superhydrophobic states: Configuration diagrams and effect of surface feature size. *Journal of Colloid and Interface Science*, 298(2):899–909, 2006.
- [34] A. Sarkar and A.-M. Kietzig. Design of a robust superhydrophobic surface: thermodynamic and kinetic analysis. *Soft Matter*, 11(10):1998–2007, 2015.
- [35] M. Nosonovsky and B. Bhushan. Hierarchical roughness optimization for biomimetic superhydrophobic surfaces. *Ultramicroscopy*, 107(10-11):969–79, 2007.
- [36] A. J. Milne and A. Amirfazli. The cassie equation: how it is meant to be used. *Advances in Colloid and Interface Science*, 170(1-2):48–55, 2012.
- [37] C. Antonini, J. B. Lee, T. Maitra, S. Irvine, D. Derome, Manish K. Tiwari, J. Carmeliet, and D. Poulikakos. Unraveling wetting transition through surface textures with x-rays: Liquid meniscus penetration phenomena. *Scientific Reports*, 4:4055, 2014.
- [38] A. Marmur. Soft contact: measurement and interpretation of contact angles. *Soft Matter*, 2(1):12–17, 2006.
- [39] E. Bormashenko. Progress in understanding wetting transitions on rough surfaces. *Advances in Colloid and Interface Science*, 2014.
- [40] G. Whyman and E. Bormashenko. How to make the cassie wetting state stable. *Langmuir*, 27(13):8171–6, 2011.
- [41] A. Marmur. Wetting on hydrophobic rough surfaces. to be heterogeneous or not to be. *Langmuir*, 19(20):8343–8348, 2003.

- 
- [42] C. W. Extrand. Model for contact angles and hysteresis on rough and ultraphobic surfaces. *Langmuir*, 18(21):7991–7999, 2002.
- [43] B. He, N. A. Patankar, and J. Lee. Multiple equilibrium droplet shapes and design criterion for rough hydrophobic surfaces. *Langmuir*, 19(12):4999–5003, 2003.
- [44] A. Lafuma and D. Quere. Superhydrophobic states. *Nature Materials*, 2(7):457–60, 2003.
- [45] V. Bahadur and S. V. Garimella. Electrowetting-based control of static droplet states on rough surfaces. *Langmuir*, 23(9):4918–4924, 2007.
- [46] J. Bico, U. Thiele, and D. Quéré. Wetting of textured surfaces. *Colloids and Surfaces A*, 206(1–3):41–46, 2002.
- [47] G. Kwak, M. Lee, K. Senthil, and K. Yong. Impact dynamics of water droplets on chemically modified wox nanowire arrays. *Applied Physics Letters*, 95(15):153101, 2009.
- [48] Y. Kwon, N. Patankar, J. Choi, and J. Lee. Design of surface hierarchy for extreme hydrophobicity. *Langmuir*, 25(11):6129–6136, 2009.
- [49] Q. S. Zheng, Y. Yu, and Z. H. Zhao. Effects of hydraulic pressure on the stability and transition of wetting modes of superhydrophobic surfaces. *Langmuir*, 21(26):12207–12212, 2005.
- [50] M. Reyssat, A. Pépin, F. Marty, Y. Chen, and D. Quéré. Bouncing transitions on microtextured materials. *EPL (Europhysics Letters)*, 74(2):306, 2006.
- [51] E. Bormashenko, R. Pogreb, G. Whyman, Y. Bormashenko, and M. Erlich. Vibration-induced cassie-wenzel wetting transition on rough surfaces. *Applied Physics Letters*, 90(20):201917, 2007.
- [52] Y. C. Jung and B. Bhushan. Dynamic effects of bouncing water droplets on superhydrophobic surfaces. *Langmuir*, 24(12):6262–6269, 2008.



- [53] P.G. de Gennes, F. Brochard-Wyart, and D. Quere. *Capillarity and Wetting Phenomena: Drops, Bubbles, Pearls, Waves*. Springer, 2004.
- [54] S. Brandon, N. Haimovich, E. Yeger, and A. Marmur. Partial wetting of chemically patterned surfaces: The effect of drop size. *Journal of Colloid and Interface Science*, 263(1):237–243, 2003.
- [55] A. Marmur. The lotus effect: Superhydrophobicity and metastability. *Langmuir*, 20(9):3517–3519, 2004.
- [56] H. Y. Erbil and C. E. Cansoy. Range of applicability of the wenzel and cassie baxter equations for superhydrophobic surfaces. *Langmuir*, 25(24):14135–14145, 2009.
- [57] S. Wang and L. Jiang. Definition of superhydrophobic states. *Advanced Materials*, 19(21):3423–3424, 2007.
- [58] G. McHale. All solids, including teflon, are hydrophilic (to some extent), but some have roughness induced hydrophobic tendencies. *Langmuir*, 25(13):7185–7187, 2009.
- [59] N. Verplanck, Y. Coffinier, V. Thomy, and R. Boukherroub. Wettability switching techniques on superhydrophobic surfaces. *Nanoscale Research Letters*, 2(12):577–596, 2007.
- [60] Y.-L. Zhang, H. Xia, E. Kim, and H.-B. Sun. Recent developments in superhydrophobic surfaces with unique structural and functional properties. *Soft Matter*, 8(44):11217–11231, 2012.
- [61] M. Nosonovsky and B. Bhushan. Stochastic model for metastable wetting of roughness-induced superhydrophobic surfaces. *Microsystem Technologies*, 12(3):231–237, 2006.
- [62] Y.-T. Cheng, D. E. Rodak, A. Angelopoulos, and T. Gacek. Microscopic observations of condensation of water on lotus leaves. *Applied Physics Letters*, 87(19):194112, 2005.

- [63] A. Checco, P. Guenoun, and J. Daillant. Nonlinear dependence of the contact angle of nanodroplets on contact line curvature. *Physical Review Letters*, 91(18):186101, 2003.
- [64] N. Michael and B. Bhushan. Hierarchical roughness makes superhydrophobic states stable. *Microelectronic Engineering*, 84(3):382–386, 2007.
- [65] M. Nosonovsky and B. Bhushan. Biomimetic superhydrophobic surfaces: Multiscale approach. *Nano Letters*, 7(9):2633–2637, 2007.
- [66] M. Nosonovsky and B. Bhushan. Roughness-induced superhydrophobicity: a way to design non-adhesive surfaces. *Journal of Physics: Condensed Matter*, 20(22):225009, 2008.
- [67] J. Huovinen, E. and Hirvi, M. Suvanto, and T. A. Pakkanen. Micro-micro hierarchy replacing micro-nano hierarchy: a precisely controlled way to produce wear-resistant superhydrophobic polymer surfaces. *Langmuir*, 28(41):14747–55, 2012.
- [68] Philip S. Brown and B. Bhushan. Designing bioinspired superoleophobic surfaces. *APL Materials*, 4(1):015703, 2016.
- [69] R. Hensel, C. Neinhuis, and C. Werner. The springtail cuticle as a blueprint for omniphobic surfaces. *Chemical Society Reviews*, 45(2):323–341, 2016.
- [70] M. Nosonovsky and B. Bhushan. Why re-entrant surface topography is needed for robust oleophobicity. *Philosophical Transactions of the Royal Society A: Mathematical, Physical and Engineering Sciences*, 374(2073), 2016.
- [71] A. Tuteja, W. Choi, M. Ma, J. M. Mabry, S. A. Mazzella, G. C. Rutledge, G. H. McKinley, and R. E. Cohen. Designing superoleophobic surfaces. *Science*, 318(5856):1618–1622, 2007.
- [72] A. Marmur. From hydrophilic to superhydrophobic: Theoretical conditions for making high-contact-angle surfaces from low-contact-angle materials. *Langmuir*, 24(14):7573–7579, 2008.

- [73] T. Nishino, M. Meguro, K. Nakamae, M. Matsushita, , and Y. Ueda. The lowest surface free energy based on cf3 alignment. *Langmuir*, 15(13):4321–4323, 1999.
- [74] T. Onda, S. Shibuichi, N. Satoh, and K. Tsujii. Super-water-repellent fractal surfaces. *Langmuir*, 12(9):2125–2127, 1996.
- [75] J. Feng, M. T. Tuominen, and J. P. Rothstein. Hierarchical superhydrophobic surfaces fabricated by dual-scale electron-beam-lithography with well-ordered secondary nanostructures. *Advanced Functional Materials*, 21(19):3715–3722, 2011.
- [76] L. Zhu, Y. Feng, X. Ye, and Z. Zhou. Tuning wettability and getting superhydrophobic surface by controlling surface roughness with well-designed microstructures. *Sensors and Actuators A: Physical*, 130-131:595–600, 2006.
- [77] Y. Li, J. Zhang, S. Zhu, H. Dong, F. Jia, Z. Wang, Y. Tang, L. Zhang, S. Zhang, and B. Yang. Bioinspired silica surfaces with near-infrared improved transmittance and superhydrophobicity by colloidal lithography. *Langmuir*, 26(12):9842–7, 2010.
- [78] H. K. Park, S. W. Yoon, and Y. R. Do. Superhydrophobicity of 2d  $SiO_2$  hierarchical micro-nanorod structures fabricated using a two-step micro-nanosphere lithography. *Journal of Materials Chemistry*, 22(28):14035–14041, 2012.
- [79] D. Wang, A. Zhao, L. Li, Q. He, H. Guo, H. Sun, and Q. Gao. Bioinspired ribbed hair arrays with robust superhydrophobicity fabricated by micro/nanosphere lithography and plasma etching. *RSC Advances*, 5(117):96404–96411, 2015.
- [80] K.-C. Park, H. J. Choi, C.-H. Chang, R. E. Cohen, G. H. McKinley, and G. Barbastathis. Nanotextured silica surfaces with robust superhydrophobicity and omnidirectional broadband supertransmissivity. *ACS Nano*, 6(5):3789–3799, 2012.

- [81] A. Checco, A. Rahman, and C. T. Black. Robust superhydrophobicity in large-area nanostructured surfaces defined by block-copolymer self assembly. *Advanced Materials*, 26(6):886–91, 2014.
- [82] N. Gupta, M. V. Kavya, Y. R. G. Singh, J. Jyothi, and H. C. Barshilia. Superhydrophobicity on transparent fluorinated ethylene propylene films. study of the degradation in hydrophobicity after exposure to the environment. *Journal of Applied Physics*, 114(16):164307, 2013.
- [83] V. Kondrashov and J. R uhe. Microcones and nanograss: Toward mechanically robust superhydrophobic surfaces. *Langmuir*, 30(15):4342–4350, 2014.
- [84] V. Jokinen, P. Suvanto, A. R. Garapaty, J. Lyytinen, J. Koskinen, and S. Franssila. Durable superhydrophobicity in embossed cytop fluoropolymer micro and nanostructures. *Colloids and Surfaces A*, 434:207–212, 2013.
- [85] S. E. Lee, D. Lee, P. Lee, S. H. Ko, S. S. Lee, and S. U. Hong. Flexible superhydrophobic polymeric surfaces with micro-/nanohybrid structures using black silicon. *Macromolecular Materials and Engineering*, 298(3), 2013.
- [86] J. Yong, Q. Yang, F. Chen, D. Zhang, U. Farooq, G. Du, and X. Hou. A simple way to achieve superhydrophobicity, controllable water adhesion, anisotropic sliding, and anisotropic wetting based on femtosecond-laser-induced line-patterned surfaces. *Journal of Materials Chemistry A*, 2(15):5499, 2014.
- [87] D. V. Ta, A. Dunn, T. J. Wasley, R. W. Kay, J. Stringer, P. J. Smith, C. Connaughton, and J. D. Shephard. Nanosecond laser textured superhydrophobic metallic surfaces and their chemical sensing applications. *Applied Surface Science*, 357, Part A:248–254, 2015.
- [88] K. Ellinas, S. P. Pujari, D. A. Dragatogiannis, C. A. Charitidis, A. Tserepi, H. Zuilhof, and E. Gogolides. Plasma micro-nanotextured, scratch, water and hexadecane resistant, superhydrophobic, and superamphiphobic polymeric surfaces with perfluorinated monolayers. *ACS Applied Materials & Interfaces*, 6(9):6510–6524, 2014.

- [89] B. G. Park, W. Lee, J. S. Kim, and K. B. Lee. Superhydrophobic fabrication of anodic aluminum oxide with durable and pitch-controlled nanostructure. *Colloids and Surfaces A*, 370(1–3):15–19, 2010.
- [90] R. Wu, G. Chao, H. Jiang, Y. Hu, and A. Pan. The superhydrophobic aluminum surface prepared by different methods. *Materials Letters*, 142:176–179, 2015.
- [91] A. Ganne, V. O. Lebed, and A. I. Gavrilov. Combined wet chemical etching and anodic oxidation for obtaining the superhydrophobic meshes with anti-icing performance. *Colloids and Surfaces A*, 499:150–155, 2016.
- [92] M. Gong, Z. Yang, X. Xu, D. Jasion, S. Mou, H. Zhang, Y. Long, and S. Ren. Superhydrophobicity of hierarchical zno nanowire coatings. *Journal of Materials Chemistry A*, 2(17):6180, 2014.
- [93] Z. Wang, Y. Tian, H. Fan, J. Gong, S. Yang, J. Ma, and J. Xu. Facile seed-assisted hydrothermal fabrication of  $\gamma$ -AlOOH nanoflake films with superhydrophobicity. *New Journal of Chemistry*, 38(3):1321–1327, 2014.
- [94] I. Sas, R. E. Gorga, J. A. Joines, and K. A. Thoney. Literature review on superhydrophobic self-cleaning surfaces produced by electrospinning. *Journal of Polymer Science B*, 50(12):824–845, 2012.
- [95] M. W. Lee, S. An, S. S. Latthe, C. Lee, S. Hong, and S. S. Yoon. Electrospun polystyrene nanofiber membrane with superhydrophobicity and superoleophilicity for selective separation of water and low viscous oil. *ACS Applied Materials & Interfaces*, 5(21):10597–10604, 2013.
- [96] Z.-Q. Dong, B.-J. Wang, X. Ma, Y.-M. Wei, and Z.-L. Xu. Fas grafted electrospun poly(vinyl alcohol) nanofiber membranes with robust superhydrophobicity for membrane distillation. *ACS Applied Materials & Interfaces*, 7(40):22652–22659, 2015.
- [97] Z. Liu, H. Wang, E. Wang, X. Zhang, R. Yuan, and Y. Zhu. Superhydrophobic poly(vinylidene fluoride) membranes with controllable structure and tunable wettability prepared by one-step electrospinning. *Polymer*, 82:105–113, 2016.

- 
- [98] X.-M. Bao, J.-F. Cui, H.-X. Sun, W.-D. Liang, Z.-Q. Zhu, J. An, B.-P. Yang, P.-Q. La, and A. Li. Facile preparation of superhydrophobic surfaces based on metal oxide nanoparticles. *Applied Surface Science*, 303:473–480, 2014.
- [99] X. Liu, Y. Wang, Z. Chen, K. Ben, and Z. Guan. A self-modification approach toward transparent superhydrophobic glass for rainproofing and superhydrophobic fiberglass mesh for oil–water separation. *Applied Surface Science*, 360, Part B:789–797, 2016.
- [100] H.-J. Choi, S. Choo, J.-H. Shin, K.-I. Kim, and H. Lee. Fabrication of superhydrophobic and oleophobic surfaces with overhang structure by reverse nanoimprint lithography. *The Journal of Physical Chemistry C*, 117(46):24354–24359, 2013.
- [101] S.-W. Ryu, S. Choo, H.-J. Choi, C.-H. Kim, and H. Lee. Replication of rose petal surfaces using a nickel electroforming process and uv nanoimprint lithography. *Applied Surface Science*, 322:57–63, 2014.
- [102] H.-J. Choi, J.-H. Shin, S. Choo, J. Kim, and H. Lee. A tunable method for nonwetting surfaces based on nanoimprint lithography and hydrothermal growth. *Journal of Materials Chemistry A*, 1(29):8417–8424, 2013.
- [103] Y. H. Sung, Y. D. Kim, H.-J. Choi, R. Shin, S. Kang, and H. Lee. Fabrication of superhydrophobic surfaces with nano-in-micro structures using uv-nanoimprint lithography and thermal shrinkage films. *Applied Surface Science*, 349:169–173, 2015.
- [104] C.-C. Liang, C.-H. Lin, T.-C. Cheng, J. Shieh, and H.-H. Lin. Nanoimprinting of flexible polycarbonate sheets with a flexible polymer mold and application to superhydrophobic surfaces. *Advanced Materials Interfaces*, 2(7), 2015.
- [105] T. Wu and Y. Suzuki. Design, microfabrication and evaluation of robust high-performance superlyophobic surfaces. *Sensors and Actuators B: Chemical*, 156(1):401–409, 2011.

- 
- [106] S. E. Lee, H.-J. Kim, S.-H. Lee, and D.-G. Choi. Superamphiphobic surface by nanotransfer molding and isotropic etching. *Langmuir*, 29(25):8070–8075, 2013.
- [107] S. M. Kang, S. M. Kim, H. N. Kim, M. K. Kwak, D. H. Tahk, and K. Y. Suh. Robust superomniphobic surfaces with mushroom-like micropillar arrays. *Soft Matter*, 8(33):8563–8568, 2012.
- [108] H. Zhao, K.-Y. Law, and V. Sambhy. Fabrication, surface properties, and origin of superoleophobicity for a model textured surface. *Langmuir*, 27(10):5927–5935, 2011.
- [109] S. Ji, P. A. Ramadhianti, T.-B. Nguyen, W. Kim, and H. Lim. Simple fabrication approach for superhydrophobic and superoleophobic al surface. *Microelectronic Engineering*, 111:404–408, 2013.
- [110] J. Ou, W. Hu, S. Liu, M. Xue, F. Wang, and W. Li. Superoleophobic textured copper surfaces fabricated by chemical etching/oxidation and surface fluorination. *ACS Applied Materials & Interfaces*, 5(20):10035–10041, 2013.
- [111] H.-B. Jo, J. Choi, K.-J. Byeon, H.-J. Choi, and H. Lee. Superhydrophobic and superoleophobic surfaces using zno nano-in-micro hierarchical structures. *Microelectronic Engineering*, 116:51–57, 2014.
- [112] H. Wang and Z. Guo. Design of underwater superoleophobic tio<sub>2</sub> coatings with additional photo-induced self-cleaning properties by one-step route bio-inspired from fish scales. *Applied Physics Letters*, 104(18):183703, 2014.
- [113] A. K. Kota, Y. Li, J. M. Mabry, and A. Tuteja. Hierarchically structured superoleophobic surfaces with ultralow contact angle hysteresis. *Advanced Materials*, 24(43):5838–5843, 2012.
- [114] V. A. Ganesh, S. S. Dinachali, A. S. Nair, and S. Ramakrishna. Robust superamphiphobic film from electrospun tio<sub>2</sub> nanostructures. *ACS Applied Materials & Interfaces*, 5(5):1527–1532, 2013.

- 
- [115] S. Y. Chou, P. R. Krauss, and P. J. Renstrom. Imprint of sub-25 nm vias and trenches in polymers. *Applied Physics Letters*, 67(21):3114, 1995.
- [116] F. Hua, Y. Sun, A. Gaur, M. A. Meitl, L. Bilhaut, L. Rotkina, J. Wang, P. Geil, M. Shim, J. A. Rogers, and A. Shim. Polymer imprint lithography with molecular-scale resolution. *Nano Letters*, 4(12):2467–2471, 2004.
- [117] C.M.S. Torres. *Alternative Lithography: Unleashing the Potentials of Nanotechnology*. Springer US, 2012.
- [118] J. Haisma, M. Verheijen, K. van den Heuvel, and J. van den Berg. Mold-assisted nanolithography: A process for reliable pattern replication. *Journal of Vacuum Science & Technology B*, 14(6):4124–4128, 1996.
- [119] X. D. Huang, L. R. Bao, X. Cheng, L. J. Guo, S. W. Pang, and A. F. Yee. Reversal imprinting by transferring polymer from mold to substrate. *Journal of Vacuum Science & Technology B*, 20(6):2872, 2002.
- [120] N. Kehagias, V. Reboud, G. Chansin, M. Zelsmann, C. Jeppesen, F. Reuther, C. Schuster, M. Kubenz, G. Gruetzner, and C. M. Sotomayor Torres. Submicron three-dimensional structures fabricated by reverse contact uv nanoimprint lithography. *Journal of Vacuum Science & Technology B*, 24(6):3002, 2006.
- [121] N. Kehagias, V. Reboud, G. Chansin, M. Zelsmann, C. Jeppesen, C. Schuster, M. Kubenz, F. Reuther, G. Gruetzner, and C. M. Sotomayor Torres. Reverse-contact uv nanoimprint lithography for multilayered structure fabrication. *Nanotechnology*, 18(17):175303, 2007.
- [122] N. Kehagias, Vincent Reboud, G. Chansin, M. Zelsmann, C. Jeppesen, F. Reuther, C. Schuster, M. Kubenz, G. Gruetzner, and C. M. Sotomayor Torres. Submicron three-dimensional structures fabricated by reverse contact uv nanoimprint lithography. *Journal of Vacuum Science & Technology B*, 24(6):3002, 2006.
- [123] N. Kehagias, M. Zelsmann, C. M. Sotomayor Torres, K. Pfeiffer, G. Ahrens, and G. Gruetzner. Three-dimensional polymer structures fabricated by



- reversal ultraviolet-curing imprint lithography. *Journal of Vacuum Science & Technology B*, 23(6):2954–2957, 2005.
- [124] L.-R. Bao, X. Cheng, X. D. Huang, L. J. Guo, S. W. Pang, and A. F. Yee. Nanoimprinting over topography and multilayer three-dimensional printing. *Journal of Vacuum Science & Technology B*, 20(6):2881–2886, 2002.
- [125] F. Zhang and H. Y. Low. Ordered three-dimensional hierarchical nanostructures by nanoimprint lithography. *Nanotechnology*, 17(8):1884, 2006.
- [126] M. Schlesinger and M. Paunovic. *Modern Electroplating*. Wiley, 2011.
- [127] H. Shinohara, M. Fukuhara, T. Hirasawa, J. Mizuno, and S. Shoji. Fabrication of magnetic nanodots array using uv nanoimprint lithography and electrodeposition for high density patterned media. *Journal of Photopolymer Science and Technology*, 21, 2008.
- [128] J. Pokki, O. Ergeneman, K. M. Sivaraman, B. Ozkale, M. A. Zeeshan, T. Luhmann, B. J. Nelson, and S. Pane. Electroplated porous polypyrrole nanostructures patterned by colloidal lithography for drug-delivery applications. *Nanoscale*, 4(10):3083–3088, 2012.
- [129] Y. Liu, S. Li, J. Zhang, Y. Wang, Z. Han, and L. Ren. Fabrication of biomimetic superhydrophobic surface with controlled adhesion by electrodeposition. *Chemical Engineering Journal*, 248:440–447, 2014.
- [130] J. Liu, S. Zhang, Y. Ma, J. Shao, B. Lu, and Y. Chen. Gold nanopillar arrays as biosensors fabricated by electron beam lithography combined with electroplating. *Applied Optics*, 54(9):2537–2542, 2015.
- [131] S.-Y. Hwang, H.-H. Park, S.-M. Kang, H.-B. Shin, and H. K. Kang. Fabrication of nanopatterned metal sheet using photolithography and electroplating. *Thin Solid Films*, 546:132–135, 2013.
- [132] D. Bera, S. C. Kuiry, and S. Seal. Synthesis of nanostructured materials using template-assisted electrodeposition. *JOM*, 56(1):49–53, 2004.

- [133] M. A. Zeeshan, K. Shou, S. Pané, E. Pellicer, J. Sort, K. M. Sivaraman, M. D. Baró, and B. J. Nelson. Structural and magnetic characterization of batch-fabricated nickel encapsulated multi-walled carbon nanotubes. *Nanotechnology*, 22(27):275713, 2011.
- [134] M. J. Burek and J. R. Greer. Fabrication and microstructure control of nanoscale mechanical testing specimens via electron beam lithography and electroplating. *Nano Letters*, 10(1):69–76, 2010.
- [135] Z. Liu, A. Prowald, S. Zein El Abedin, and F. Endres. Template-assisted electrodeposition of highly ordered macroporous zinc structures from an ionic liquid. *Journal of Solid State Electrochemistry*, 17(4):1185–1188, 2013.
- [136] K. Hnida, J. Mech, and G. D. Sulka. Template-assisted electrodeposition of indium–antimony nanowires – comparison of electrochemical methods. *Applied Surface Science*, 287:252–256, 2013.
- [137] T.A. Osswald, L.S. Turng, and P.J. Gramann. *Injection Molding Handbook*. Carl Hanser Publishers, 2008.
- [138] M. Matschuk, H. Bruus, and N. B. Larsen. Nanostructures for all-polymer microfluidic systems. *Microelectronic Engineering*, 87(5–8):1379–1382, 2010.
- [139] Y. Qin. *Micromanufacturing Engineering and Technology*. Elsevier Science, 2010.
- [140] C. Hopmann, C. Behmenburg, U. Recht, and K. Zeuner. Injection molding of superhydrophobic liquid silicone rubber surfaces. *Silicon*, 6(1):35–43, 2014.
- [141] W. Michaeli, M. Schongart, F. Klaiber, and S. Beckemper. Production of superhydrophobic surfaces using a one-step variothermal injection moulding process. *Micro and Nanosystems*, 3(3):222–225, 2011.
- [142] M. Liu and Q. Chen. Characterization study of bonded and unbonded polydimethylsiloxane aimed for bio-micro-electromechanical systems-related applications. *Journal of Micro/Nanolithography, MEMS, and MOEMS*, 6(2):023008–023008–6, 2007.

- 
- [143] L. Miao, S. Jianren, S. Ying, B. Christopher, and C. Quanfang. Thickness-dependent mechanical properties of polydimethylsiloxane membranes. *Journal of Micromechanics and Microengineering*, 19(3):035028, 2009.
- [144] A. Francone. *Materials and anti-adhesive issues in UV-NIL*. PhD thesis, Institut National Polytechnique de Grenoble, 2010.
- [145] W. Zhou. *Nanoimprint Lithography: An Enabling Process for Nanofabrication: An Enabling Process for Nanofabrication*. Springer, 2013.
- [146] S.A. Campbell. *The Science and Engineering of Microelectronic Fabrication*. Oxford University Press, 1996.
- [147] G.S. May and C.J. Spanos. *Fundamentals of Semiconductor Manufacturing and Process Control*. Wiley, 2006.
- [148] D. Stokes. *Principles and Practice of Variable Pressure: Environmental Scanning Electron Microscopy (VP-ESEM)*. Wiley, 2008.
- [149] C. Auner, U. Palfinger, H. Gold, J. Kraxner, A. Haase, T. Haber, M. Sezen, W. Grogger, G. Jakopic, J. R. Krenn, G. Leising, and B. Stadlober. Residue-free room temperature uv-nanoimprinting of submicron organic thin film transistors. *Organic Electronics*, 10(8):1466–1472, 2009.
- [150] C. Auner, U. Palfinger, H. Gold, J. Kraxner, A. Haase, Thomas Haber, M. Sezen, W. Grogger, G. Jakopic, J. R. Krenn, G. Leising, and B. Stadlober. High-performing submicron organic thin-film transistors fabricated by residue-free embossing. *Organic Electronics*, 11(4):552–557, 2010.
- [151] K.-Y. Yang, K.-M. Yoon, J.-W. Kim, J.-H. Lee, and H. Lee. Low temperature fabrication of residue-free polymer patterns on flexible polymer substrate. *Japanese Journal of Applied Physics*, 48(9):095003, 2009.
- [152] H. Yoon, K. M. Lee, D.-Y. Khang, H. H. Lee, and S.-J. Choi. Rapid flash patterning of nanostructures. *Applied Physics Letters*, 85(10):1793, 2004.

- [153] K. Yu-Chih and H. Franklin Chau-Nan. Residual-layer-free direct printing by selective filling of a mould. *Journal of Micromechanics and Microengineering*, 21(2):025026, 2011.
- [154] P. Hyunsoo and C. Xing. Thermoplastic polymer patterning without residual layer by advanced nanoimprinting schemes. *Nanotechnology*, 20(24):245308, 2009.
- [155] S. Hemmilä, J. V. Cauich-Rodríguez, J. Kreutzer, and P. Kallio. Rapid, simple, and cost-effective treatments to achieve long-term hydrophilic pdms surfaces. *Applied Surface Science*, 258(24):9864–9875, 2012.
- [156] W. Li and A. Amirfazli. Hierarchical structures for natural superhydrophobic surfaces. *Soft Matter*, 4(3):462, 2008.
- [157] Y. Chae Jung and B. Bhushan. Dynamic effects induced transition of droplets on biomimetic superhydrophobic surfaces. *Langmuir*, 25(16):9208–9218, 2009.
- [158] B. Bhushan, Y. C. Jung, and K. Koch. Micro-, nano- and hierarchical structures for superhydrophobicity, self-cleaning and low adhesion. *Philosophical transactions A*, 367(1894):1631–72, 2009.
- [159] X. Zhang, L. Wang, and E. Levanen. Superhydrophobic surfaces for the reduction of bacterial adhesion. *RSC Advances*, 3(30):12003–12020, 2013.
- [160] H. Y. Erbil, A. L. Demirel, Y. Avci, and O. Mert. Transformation of a simple plastic into a superhydrophobic surface. *Science*, 299(5611):1377–1380, 2003.
- [161] X.-J. Huang, D.-H. Kim, M. Im, J.-H. Lee, J. B. Yoon, and Y.-K. Choi. “lock-and-key” geometry effect of patterned surfaces: Wettability and switching of adhesive force. *Small*, 5(1):90–94, 2009.
- [162] Z. Wang, N. Koratkar, L. Ci, and P. M. Ajayan. Combined micro-/nanoscale surface roughness for enhanced hydrophobic stability in carbon nanotube arrays. *Applied Physics Letters*, 90(14):143117, 2007.

- 
- [163] B. Bhushan and E. K. Her. Fabrication of superhydrophobic surfaces with high and low adhesion inspired from rose petal. *Langmuir*, 26(11):8207–8217, 2010.
- [164] M. Liu and L. Jiang. Switchable adhesion on liquid/solid interfaces. *Advanced Functional Materials*, 20(21):3753–3764, 2010.
- [165] G. Gong, J. Wu, X. Jin, and L. Jiang. Adhesion tuning at superhydrophobic states: From petal effect to lotus effect. *Macromolecular Materials and Engineering*, 300(11):1057–1062, 2015.
- [166] G. Guangming, W. Juntao, Z. Yong, L. Jingang, J. Xu, and J. Lei. A novel fluorinated polyimide surface with petal effect produced by electrospinning. *Soft Matter*, 10(4):549–552, 2014.
- [167] Z. Cheng, M. Du, H. Lai, N. Zhang, and K. Sun. From petal effect to lotus effect: a facile solution immersion process for the fabrication of super-hydrophobic surfaces with controlled adhesion. *Nanoscale*, 5(7):2776–2783, 2013.
- [168] N. D. Boscher, D. Duday, S. Verdier, and P. Choquet. Single-step process for the deposition of high water contact angle and high water sliding angle surfaces by atmospheric pressure dielectric barrier discharge. *ACS Applied Materials & Interfaces*, 5(3):1053–1060, 2013.
- [169] E. Bormashenko, R. Pogreb, G. Whyman, and M. Erlich. Cassie - wenzel wetting transition in vibrating drops deposited on rough surfaces: Is the dynamic cassie - wenzel wetting transition a 2d or 1d affair? *Langmuir*, 23(12):6501–6503, 2007.
- [170] M. Reyssat, D. Richard, C. Clanet, and D. Quere. Dynamical superhydrophobicity. *Faraday Discussions*, 146(0):19–33, 2010.
- [171] D. Bartolo, F. Bouamrine, Verneuil É, A. Buguin, P. Silberzan, and S. Moulinet. Bouncing or sticky droplets: Impalement transitions on superhydrophobic micropatterned surfaces. *EPL (Europhysics Letters)*, 74(2):299, 2006.

- 
- [172] I. S. Bayer and C. M. Megaridis. Contact angle dynamics in droplets impacting on flat surfaces with different wetting characteristics. *Journal of Fluid Mechanics*, 558:415–449, 2006.
- [173] T. Deng, K. K. Varanasi, M. Hsu, N. Bhate, C. Keimel, J. Stein, and M. Blohm. Nonwetting of impinging droplets on textured surfaces. *Applied Physics Letters*, 94(13):133109, 2009.
- [174] M. Reyssat, A. Pépin, F. Marty, Y. Chen, and D. Quéré. Bouncing transitions on microtextured materials. *EPL (Europhysics Letters)*, 74(2):306, 2006.
- [175] S. Dash, M. T. Alt, and S. V. Garimella. Hybrid surface design for robust superhydrophobicity. *Langmuir*, 28(25):9606–9615, 2012.
- [176] H.-M. Kwon, A. T. Paxson, K. K. Varanasi, and N. A. Patankar. Rapid deceleration-driven wetting transition during pendant drop deposition on superhydrophobic surfaces. *Physical Review Letters*, 106(3):036102, 2011.
- [177] L. Chen, Z. Xiao, P. C. H. Chan, Y.-K. Lee, and Z. Li. A comparative study of droplet impact dynamics on a dual-scaled superhydrophobic surface and lotus leaf. *Applied Surface Science*, 257(21):8857–8863, 2011.
- [178] Y. H. Yeong, J. Burton, E. Loth, and I. S. Bayer. Drop impact and rebound dynamics on an inclined superhydrophobic surface. *Langmuir*, 30(40):12027–12038, 2014.
- [179] A. Tuteja, W. Choi, G. H. McKinley, R. E. Cohen, and M. F. Rubner. Design parameters for superhydrophobicity and superoleophobicity. *MRS Bulletin*, 33(08):752–758, 2008.
- [180] H. Schiff. Nanoimprint lithography: 2d or not 2d? a review. *Applied Physics A*, 121(2):415–435, 2015.
- [181] Y. Chen. Applications of nanoimprint lithography/hot embossing: a review. *Applied Physics A*, 121(2):451–465, 2015.

- 
- [182] S. Möllenbeck, N. Bogdanski, M. Wissen, H. C. Scheer, J. Zajadacz, and K. Zimmer. Investigation of the separation of 3d-structures with undercuts. *Microelectronic Engineering*, 84(5–8):1007–1010, 2007.
- [183] S. Möllenbeck, N. Bogdanski, H. C. Scheer, J. Zajadacz, and K. Zimmer. Moulding of arrowhead structures. *Microelectronic Engineering*, 86(4–6):608–610, 2009.
- [184] S. Srinivasan, G. H. McKinley, and R. E. Cohen. Assessing the accuracy of contact angle measurements for sessile drops on liquid-repellent surfaces. *Langmuir*, 27(22):13582–13589, 2011.
- [185] J. B. Boreyko, C. H. Baker, C. R. Poley, and C. H. Chen. Wetting and dewetting transitions on hierarchical superhydrophobic surfaces. *Langmuir*, 27(12):7502–9, 2011.
- [186] E. Bormashenko, R. Balter, and D. Aurbach. Formation of liquid marbles and wetting transitions. *Journal of Colloid and Interface Science*, 384(1):157–161, 2012.
- [187] G. Vázquez, E. Alvarez, and J. M. Navaza. Surface tension of alcohol + water from 20 to 50 c. *Journal of Chemical & Engineering Data*, 40:611–614, 1995.
- [188] S. Merino, A. Retolaza, V. Trabadelo, A. Cruz, P. Heredia, J. A. Alduncín, D. Mecerreyes, I. Fernández-Cuesta, X. Borrísé, and F. Pérez-Murano. Protein patterning on the micro- and nanoscale by thermal nanoimprint lithography on a new functionalized copolymer. *Journal of Vacuum Science & Technology B*, 27(6):2439–2443, 2009.
- [189] R. D. O’Rorke, T. W. J. Steele, and H. K. Taylor. Bioinspired fibrillar adhesives: a review of analytical models and experimental evidence for adhesion enhancement by surface patterns. *Journal of Adhesion Science and Technology*, 30(4):362–391, 2016.
- [190] R. Sahay, H. Y. Low, A. Baji, S. Foong, and K. L. Wood. A state-of-the-art review and analysis on the design of dry adhesion materials for applications such as climbing micro-robots. *RSC Advances*, 5(63), 2015.